Myristoylated Neuronal Calcium Sensor-1 captures the ciliary vesicle at distal appendages

Tomoharu Kanie[1,2,4], Roy Ng[1], Keene L. Abbott[1], Olaf Pongs[3], and Peter K. Jackson[1,4]

[1]Baxter Laboratory, Department of Microbiology & Immunology and Department of Pathology, Stanford University, Stanford, CA, 94305

[2]Department of Cell Biology, University of Oklahoma Health Sciences Center, Oklahoma, OK, 73112

[3]Institute for Physiology, Center for Integrative Physiology and Molecular Medicine (CIPPM), Saarland University, Homburg, Germany

[4]Corresponding authors

Summary (230 Words)

The primary cilium is a microtubule-based organelle that cycles through assembly and disassembly. In many cell types, formation of the cilium is initiated by recruitment of ciliary vesicles to the distal appendage of the mother centriole. However, the distal appendage mechanism that directly captures ciliary vesicles is yet to be identified. In an accompanying paper, we show that the distal appendage protein, CEP89, is important for thef ciliary vesicle recruitment, but not for other steps of cilium formation (Tomoharu Kanie, Love, Fisher, Gustavsson, & Jackson, 2023). The lack of a membrane binding motif in CEP89 suggests that it may indirectly recruit ciliary vesicles via another binding partner. Here, we identify Neuronal Calcium Sensor-1 (NCS1) as a stoichiometric interactor of CEP89. NCS1 localizes to the position between CEP89 and a ciliary vesicle marker, RAB34, at the distal appendage. This localization was completely abolished in CEP89 knockouts, suggesting that CEP89 recruits NCS1 to the distal appendage. Similarly to CEP89 knockouts, ciliary vesicle recruitment as well as subsequent cilium formation was perturbed in NCS1 knockout cells. The ability of NCS1 to recruit the ciliary vesicle is dependent on its myristoylation motif and NCS1 knockout cells expressing myristoylation defective mutant failed to rescue the vesicle recruitment defect despite localizing proper localization to the centriole. In sum, our analysis reveals the first known mechanism for how the distal appendage recruits the ciliary vesicles.

Introduction

The primary cilium is an organelle that consists of the microtubule-based axoneme surrounded by the ciliary membrane, which accumulates specific membrane proteins (e.g., G-protein coupled receptors) to serve as a sensor for extracellular environmental cues (Reiter & Leroux, 2017). The cilium extends from the mother centriole, and cycles assembly and disassembly, as the cell needs to disassemble the cilium prior to mitosis (Vorobjev & Chentsov Yu, 1982) to allow the centrosome to function within the spindle pole during mitosis. The processes of the cilium formation were described in great detail through electron microscopy by Sergei Sorokin in 1960s (S. Sorokin, 1962) (S. P. Sorokin, 1968) and is known to be subdivided to two types called the extracellular and intracellular pathways (Molla-Herman et al., 2010). In the extracellular pathway used, for example, by mouse inner medullary collecting duct cells (mIMCD3 cells), the mother centriole is believed to first dock to the plasma membrane before the extension of the axonemal microtubule as well as ciliary membrane (Molla-Herman et al., 2010). In the intracellular pathway used, for example, by Retinal Pigment Epithelia (RPE) cells (Molla-Herman et al., 2010) and fibroblasts (S. Sorokin, 1962) (Molla-Herman et al., 2010), the first step of cilium formation is attachment of the small vesicles, or so-called ciliary vesicles, to the distal end of the mother centriole (S. Sorokin, 1962), or more specifically to the distal appendage (Schmidt et al., 2012; Sillibourne et al., 2013). The distal appendage is a nine-fold blade-like structure attached to the distal end of the mother centriole (Anderson, 1972; Bowler et al., 2019; Paintrand, Moudjou, Delacroix, & Bornens, 1992). The ciliary vesicle recruitment is followed by the fusion of the small vesicles (Lu et al., 2015), removal of CP110 (Lu et al., 2015), which is believed to cap the distal end of the mother centriole (Spektor, Tsang, Khoo, & Dynlacht, 2007), and subsequently axonemal extension, which is mediated at least partially by

54 intraflagellar transport (IFT) (Craft, Harris, Hyman, Kner, & Lechtreck, 2015). While the distal
55 appendage is indispensable for all those steps, how exactly the distal appendage controls these
56 multiple processes is largely unknown.

57 To understand the molecular roles of the distal appendage, we first need to uncover its
58 molecular composition and identify critical functions of distal appendage proteins. In an
59 accompanying paper, we comprehensively analyzed all known distal appendage proteins to date
60 and revealed that the Centrosomal Protein 89 (CEP89) is important for ciliary vesicle
61 recruitment, but not for other processes organizing cilium formation (Tomoharu Kanie et al.,
62 2023). Since CEP89 lacks apparent lipid binding motifs, we hypothesized that an interacting
63 partner of CEP89 may bind to ciliary vesicle directly. We sought to identify and understand the
64 protein directly recruiting the ciliary vesicle.

65 **Results**

66 **Discovery of Neuronal Calcium Sensor-1 as a stoichiometric interactor of CEP89**

67 To identify interacting partners of CEP89, we performed tandem affinity purification and mass
68 spectrometry (TAP-MS) (Rigaut et al., 1999). Localization and affinity purification (LAP)
69 (Cheeseman & Desai, 2005) tagged CEP89 was expressed in retinal pigment epithelia
70 immortalized with human telomerase (RPE-hTERT), and CEP89 was immunoprecipitated first
71 by Green Fluorescent Protein (GFP) antibody beads followed by a second affinity precipitation
72 by S protein beads. Final eluates were resolved by SDS-PAGE gel and analyzed by silver-
73 staining (Figure 1A) and mass spectrometry (Figure 1B). This analysis identified two
74 stoichiometric interactors, Neuronal Calcium Sensor-1 (NCS1) and C3ORF14, consistent with
75 the previous high-throughput proteome analyses, which identified both proteins as either CEP89
76 interactors (Huttlin et al., 2021) or neighbors (Gupta et al., 2015). Consistent with the TAP-MS

77 data, endogenous NCS1 strongly coimmunoprecipitated with endogenous CEP89 (Figure 1-
78 figure supplement 1A).

79 NCS1 is a member of NCS family proteins, which are characterized as containing
80 calcium binding EF-hand motifs as well as a myristoylation signal for N-terminal addition of
81 myristate (Burgoyne & Weiss, 2001). NCS1 was first identified as Frequenin in Drosophila, a
82 protein that can facilitate neurotransmitter release in neuromuscular junction (Pongs et al., 1993).
83 Since then, numerous papers propose models wherein NCS1 is involved in both presynaptic and
84 postsynaptic functions (reviewed in (Dason, Romero-Pozuelo, Atwood, & Ferrus, 2012)).
85 However, how exactly NCS-1 regulates neuronal function is still not well understood. As
86 described later in this paper, NCS-1 is expressed ubiquitously in various tissues, consistent with
87 the previous report (Gierke et al., 2004). While the previous literatures reported the role of NCS1
88 in other cell types including cardiomyocytes (Nakamura, Jeromin, Mikoshiba, & Wakabayashi,
89 2011) and adipocytes (Ratai, Hermainski, Ravichandran, & Pongs, 2019), molecular mechanisms
90 regulating non-neuronal functions of NCS1 remains enigmatic. A centrosomal role of NCS1 has
91 never been described.

92 CEP89 binding to NCS1 required the N-terminal region (1-343a.a.) (Figure 1C and D).
93 The C-terminal portion of CEP89 (344-783a.a.) is required for its centrosomal localization
94 (Figure 1- figure supplement 1B), consistent with a previous report (Sillibourne et al., 2013). An
95 *in vitro* binding assay using *in vitro* translated proteins revealed that HA tagged CEP89 directly
96 binds to MYC tagged C3ORF14 and NCS1 (Figure 1E), whereas HA-C3ORF14 did not bind to
97 NCS1 (Figure 1F). A negative control, CEP350 fragment (2470-2836 a.a.), which binds to its
98 binding partner FGFR1OP (or FOP) efficiently (Figure 1-figure supplement 2A) as previously
99 described (T. Kanie et al., 2017), did not bind to either HA-CEP89, nor HA-C3ORF14 (Figure

100 1E and F). Thus, CEP89 serves to bridge NCS1 and C3ORF14 (Figure 1G).

101

102 **NCS1 is recruited to the distal appendage by CEP89 and is positioned between CEP89 and**

103 **the ciliary vesicle marker, RAB34**

104 We next sought to determine the precise localization of NCS1 and C3ORF14. When observed

105 via a wide-field microscopy, NCS1 localized to the mother centriole, marked by CEP170 (Figure

106 2A). Some cytoplasmic staining was also observed. Both centriolar and cytoplasmic staining was

107 highly specific as the signal was strongly reduced in NCS1 knockout cells (Figure 2A). The

108 cytoplasmic localization of NCS1 is inconsistent with a previous study, where C-terminally

109 Enhanced Yellow Fluorescent Protein (EYFP) tagged NCS1 constitutively localized to

110 membranous compartments (O'Callaghan et al., 2002). We tested if the difference in localization

111 is due to the tagging. We also tested whether membrane binding, myristoylation motif, of NCS1

112 affects its localization by making the myristoylation defective mutant by converting the position

113 2 glycine to alanine (NCS1-G2A). N-terminally LAP (EGFP and S) tagged wild-type or G2A

114 mutant of NCS1 localized to mother centriole as well as cytoplasm, similar to endogenous NCS1

115 (Figure 2- figure supplement 1A and B). Consistent with the previous paper (O'Callaghan et al.,

116 2002), C-terminally LAP tagged wild-type NCS1 localized to membrane compartments, such as

117 plasma membrane and endoplasmic reticulum, whereas the myristoylation defective mutant

118 (G2A) diffusely localized to cytoplasm (Figure 2-figure supplement 1C and D). This result

119 suggests that C-terminal tagging of NCS1 changes its localization potentially via exposing the

120 myristoylation motif of NCS1, and endogenous NCS1 may sequester its myristoylation motif to

121 allow localization to cytoplasm. A small amount of nuclear localization observed in LAP tagged

122 NCS1 likely derives from LAP tagging (Figure 2- figure supplement 1), as the endogenous

123 NCS1 did not localize to nucleus (Figure 2A). Similar to NCS1, C-terminally LAP tagged
124 C3ORF14 localized to the location between acetylated tubulin, a cilium marker, and Pericentrin,
125 a centrosome marker, suggesting that it also localizes specifically to the mother centriole (Figure
126 2B). NCS1 localization to the mother centriole was enhanced upon serum deprivation (Figure
127 2C), a condition that induces cilium formation in RPE cells, much like several other distal
128 appendage proteins (see Figure 1D of (Tomoharu Kanie et al., 2023)). When observed via 3D
129 structured illumination microscopy, of which resolution is twice as high as a diffraction limited
130 microscopy (Y. Wu & Shroff, 2018), C-terminally LAP (EGFP-S) tagged C3ORF14 localized to
131 a position slightly distal to the distal appendage protein, CEP164, in side-view (Figure 2D).
132 When top (or axial) view of the mother centriole was visualized, LAP-C3ORF14 formed a ring-
133 like structure that is slightly smaller than the CEP164 ring (Figure 2E), which is reminiscent of
134 the 9-fold symmetrical structure of the distal appendage (Paintrand et al., 1992). Similarly, NCS1
135 localized slightly distal to CEP164 (Figure 2F) as well as the binding partner, CEP89 (Figure
136 2G), and slightly proximal to the ciliary vesicle marker, RAB34 (Stuck, Chong, Liao, & Pazour,
137 2021) (Tomoharu Kanie et al., 2023) (Figure 2H). Like C3ORF14, NCS1 formed a slightly
138 smaller ring than CEP164 (Figure 2I). Consistent with this, the ring diameter of NCS1 and
139 C3ORF14 was 319.5±7.7 nm (n=13, average±SEM) and 348.8±8.0 nm (n=16, average±SEM),
140 respectively (see Figure 1C of (Tomoharu Kanie et al., 2023)). It is notable that both C3ORF14
141 and NCS1 also localized to the region close to subdistal appendage in some but not all centrioles
142 (Figure 2D and F), consistent with what was observed for CEP89 localization (Chong et al.,
143 2020). This near subdistal appendage localization explains why C3ORF14 was previously
144 classified as a subdistal appendage protein (Gupta et al., 2015). These results suggest that NCS1
145 localizes to the distal appendage and more precisely to the position sandwiched between CEP89

146 and the ciliary vesicle (Figure 2J).

147 We next determined the hierarchy of the three proteins. Centriolar localization of CEP89 was not
148 affected by depletion of either NCS1 nor C3ORF14 (Figure 2K and Figure 2-figure supplement
149 2A). NCS1 failed to localize to the mother centriole without altering its cytoplasmic localization
150 in CEP89 knockout cells but not in C3ORF14 knockout cells (Figure 2L and Figure 2-figure
151 supplement 2B), indicating that CEP89 recruits NCS1 to the distal appendage. The lack of NCS1
152 localization at the centriole in CEP89 knockouts cells was rescued by expressing untagged
153 CEP89 (Figure 2L and Figure 2- figure supplement 2B). C3ORF14 localization required CEP89,
154 but not NCS1 (Figure 2M and Figure 2- figure supplement 2C). The expression level of neither
155 NCS1, nor C3ORF14 was affected by CEP89 depletion (Figure 2- figure supplement 2D and E).
156 These results suggest that both NCS1 and C3ORF14 are recruited to the distal appendage by
157 CEP89 (Figure 2N). We also tested whether the three proteins affect localization of other distal
158 appendage proteins and found that the localization of other distal appendage proteins were
159 unchanged in cells deficient in CEP89, NCS1, or C3ORF14 (Figure 2-figure supplement 3A-C)
160 (see also Figure 2A-L of (Tomoharu Kanie et al., 2023)). Similar to the centriolar localization of
161 CEP89, which was significantly reduced in CEP83 or SCLT1 knockouts, NCS1 localization was
162 also greatly diminished in these knockouts (Figure 2-figure supplement 3D). This is consistent
163 with the observation that CEP83-SCLT1 module serves as a structural component of the distal
164 appendage (see (Tomoharu Kanie et al., 2023) for the detail). In contrast, the feedback complex
165 CEP164-TTBK2 (see (Tomoharu Kanie et al., 2023) for the detail) was required for proper
166 centriolar localization of NCS1 (Figure 2- figure supplement 3D) but not for CEP89 (Figure 2F
167 of (Tomoharu Kanie et al., 2023)). Given that CEP89 is a substrate of TTBK2 (Bernatik et al.,
168 2020; Lo et al., 2019), this might suggest that phosphorylation of TTBK2 could affect the

169 interaction between CEP89 and NCS1. It is also possible that NCS1 may be a phosphorylation
170 target of TTBK2. These questions warrant future investigation.
171
172 **NCS1 is important for efficient ciliary vesicle recruitment at the distal appendage**
173 We next sought to understand the role of NCS1 at the distal appendage and performed kinetic
174 analysis of ciliation in control (sgGFP) and knockouts of CEP89, NCS1, or C3ORF14 in RPE
175 cells, in which serum starvation induces cilium formation (Figure 3A). Control RPE cells form
176 cilia over 24 hours after serum starvation, and almost of all cells completed cilium formation
177 between 24 and 48 hours. CEP89 and NCS1 knockouts displayed a notable delay in initiating
178 ciliation (see 12-hour in Figure 3A), but gradually catch up on ciliogenesis and exhibited only
179 mild ciliary formation defects at later time points (see 48 hours in Figure 3A). The cilium
180 formation defect was rescued by expressing untagged CEP89 in CEP89 knockouts or untagged
181 NCS1 in NCS1 knockouts (Figure 3B). This kinetic defect is strongly consistent with the
182 knockouts of several other distal appendage proteins, namely ANKRD26 and FBF1 (Figure 5A
183 and B of (Tomoharu Kanie et al., 2023)). Consistent with the cells deficient in ANKRD26 or
184 FBF1 (see Figure 5- figure supplement 1 of (Tomoharu Kanie et al., 2023)), ciliary ARL13B
185 signal intensity was reduced in CEP89 or NCS1 knockouts even after the cells complete cilium
186 formation (Figure 3-figure supplement 1A-C). This suggests that even though the NCS1 or
187 CEP89 knockouts can eventually form primary cilia, those cilia may be functionally different
188 from wild-type cilia. C3ORF14 knockouts showed similar but much milder kinetic defect of
189 cilium formation than CEP89 or NCS1 knockouts, therefore, we focused on NCS1 in the
190 subsequent investigation.
191 We then sought to understand how NCS1 is involved in cilium formation. In an

192 accompanying paper (Tomoharu Kanie et al., 2023), we showed that CEP89 participates in
193 cilium formation by regulating ciliary vesicle recruitment without affecting IFT88::CEP19
194 recruitment, important steps that require distal appendage proteins (Schmidt et al., 2012)
195 (Dateyama et al., 2019)(see Figure 5 of (Tomoharu Kanie et al., 2023)). We tested if NCS1 has
196 similar roles to its binding partner, CEP89. Indeed, NCS1 knockouts exhibited moderate ciliary
197 vesicle recruitment defect, similar to CEP89 knockouts, when assessed using RAB34 as a ciliary
198 vesicle marker (Figure 3C). Transmission electron microscopy analysis confirmed the ciliary
199 vesicle recruitment defect in NCS1 knockouts (Figure 3D and E). The presence of fused vesicles,
200 albeit much lower percentage than control cells, in NCS1 knockouts (Figure 3D and E) suggests
201 that NCS1 is important for recruitment but not fusion of the ciliary vesicle. Removal of CP110,
202 which is believed to act as a cap of axonemal microtubule, was partially, but measurably affected
203 in NCS1 knockout cells (Figure 3F), consistent with the fact that CP110 removal is in part
204 downstream of ciliary vesicle recruitment (Figure 4D of (Tomoharu Kanie et al., 2023)). Neither
205 IFT88 nor CEP19 recruitment to the centriole was affected in NCS1 knockout cells (Figure 3G
206 and H). These results suggest that NCS1 plays an important role in cilium formation by
207 regulating ciliary vesicle recruitment, but not other known processes of cilium formation,
208 consistent with the role of CEP89 in ciliary vesicle recruitment.

209 **Yet unknown distal appendage proteins may compensate the lack of NCS1 in ciliary vesicle**
210 **recruitment**

211 As we showed in an accompanying paper, the distal appendage is indispensable for the
212 recruitment of the ciliary vesicle to the mother centriole. Virtually no RAB34 positive ciliary
213 vesicle was observed at mother centriole in cells deficient in CEP164, CEP83, or TTBK2, which
214 are critical for structural integrity of the distal appendage (Figure 5C of (Tomoharu Kanie et al.,

215 2023)). This phenotype is much stronger than what we observed in CEP89 or NCS1 knockouts
216 (Figure 3C), suggesting that some other distal appendage proteins may compensate the lack of
217 NCS1 for the ciliary vesicle recruitment. To address this question, we created cells lacking both
218 NCS1 and each of the other distal appendage proteins (FBF1, CEP89, ANKRD26, KIZ,
219 LRRC45) as well as the distal appendage associated protein, INPP5E (Figure 4A). We omitted
220 the integral components of the distal appendage proteins (CEP164, TTBK2, CEP83, SCLT1)
221 from the analysis, as the knockouts of these proteins showed very strong ciliary vesicle
222 recruitment defects on their own, therefore making it difficult to test if the NCS1 depletion
223 shows additive effects. Cilium formation assay revealed that depletion of NCS1 decreased the
224 percentage of ciliated cells in each single knockout cells, except CEP89 (Figure 4B and C). This
225 suggests that CEP89, but no other distal appendage protein regulates the same ciliary formation
226 pathway as NCS1. Similarly, depletion of NCS1 decreased the RAB34 positive centriole in each
227 of the single distal appendage knockout cells, except CEP89 knockouts (Figure 4D). These
228 results suggest that yet unknown distal appendage proteins would be required to compensate for
229 the ciliary vesicle recruitment defect of NCS1 knockout cells. Another possibility is that one or
230 more integral components (CEP164, TTBK2, SCLT1, and CEP83) may be directly involved in
231 ciliary vesicle recruitment. These hypotheses warrant future investigation.

232 **NCS1 captures ciliary vesicle via its myristoylation motif**

233 Since NCS1 is myristoylated, we wondered whether the membrane association motif is
234 necessary for NCS1 to recruit the ciliary vesicle. We tested this hypothesis by creating a
235 myristoylation defective mutant (NCS1-G2A). We tested whether the mutant indeed lost the
236 ability to bind membrane using differential centrifugation following nitrogen cavitation. We first
237 determined which fraction is the most optimal to assess membrane association in our

238 experimental setting. While the microsomal fraction prepared from the pellet following
239 ultracentrifugation at 100,000 g is often used to analyze membrane fraction of the cells (Graham,
240 2015), the plasma membrane marker, Epidermal Growth Factor Receptor (EGFR), was enriched
241 mostly in the pellet following centrifugation at 15,000 *g* in our experiment (Figure 5A; see
242 Methods for further explanation of the technical design). In addition, NCS1-G2A was
243 fractionated in the 100,000 *g* pellet to similar extent as wild-type NCS1 (Figure 5A), indicating
244 that centrifugation at 100,000 *g* may also pellet some soluble proteins, even though cytoplasmic
245 protein RabGDI remained in the 100,000 *g* supernatant. Thus, we decided to use 15,000 *g* pellet
246 to assess membrane fraction in our experiment. In control cells (sgSafe), both NCS1 and CEP89
247 was found in both soluble fraction (15,000 *g* supernatant) and membrane fraction (15,000 *g*
248 pellet) (Figure 5A). In contrast, NCS1-G2A was only found in the soluble fraction (15,000 *g*
249 supernatant) (Figure 5A), suggesting that myristoylation is required for membrane localization of
250 NCS1. Interestingly, CEP89 was only found in the soluble fraction (15,000 *g* supernatant) in
251 NCS1 knockout cells expressing either empty vector or NCS1-G2A, but not NCS1-WT. This
252 suggests that membrane localization of CEP89 requires NCS1 with an intact myristoylation
253 motif. When expressed at similar level to endogenous NCS1 (Figure 5B), both wild-type and the
254 myristoylation defective (G2A) NCS1 localizes to the mother centriole to a similar extent
255 (Figure 5C and D). However, the myristoylation defective mutant almost completely failed to
256 rescue ciliation and ciliary vesicle recruitment defect of NCS1 knockout cells (Figure 5E and F).
257 These data suggest that NCS1 recruits ciliary vesicle to the distal appendage via its
258 myristoylation motif (Figure 5G).

259 **Calcium binding is needed for stability of NCS1**

260 In addition to myristoylation motif, human NCS1 also has three functional and one apparently

261 non-functional (due to the mutation in critical amino acids needed for co-ordination bond with
262 calcium) EF-hand motifs (Bourne, Dannenberg, Pollmann, Marchot, & Pongs, 2001). Several
263 other NCS family proteins, including Recoverin and Hippocalcin, show a calcium-myristoyl
264 switch (Ames et al., 1997; O'Callaghan, Tepikin, & Burgoyne, 2003). In this mechanism, the
265 sequestered myristoylation motif is exposed to allow the protein to bind membrane upon calcium
266 binding. It has been proposed that NCS1 may employ a similar molecular switch. While the
267 structure of fission yeast Ncs1, solved by nuclear magnetic resonance spectroscopy showed the
268 calcium-myristoyl switch (Lim, Strahl, Thorner, & Ames, 2011), several lines of evidence
269 suggest the absence of that type of switch in budding yeast and mammalian NCS1(Ames et al.,
270 2000; O'Callaghan et al., 2002) (Lemire, Jeromin, & Boisselier, 2016). Since a myristoylation
271 defective mutant of NCS1 failed to form cilia efficiently without affecting its centrosomal
272 localization (Figure 5C and E), we tested if there is a calcium-myristoylation switch by making
273 various EF-hand mutations, where each or combination of the three active EF-hand motif was
274 disabled by mutating invariant glutamate at -Z position to glutamine (E84Q for the 1st, E120Q
275 for the 2nd, and E168Q for the 3rd active EF-hand mutation). We expressed *wild type* or EF-hand
276 mutants of untagged NCS1 in NCS1 knockout cells and detected the expression and the
277 localization of each mutant using α-NCS1 antibody. The wild-type and the mutants of NCS1
278 were functionally tested via ciliation assay rather than the ciliary vesicle recruitment assay,
279 because the ciliation assay is much less variable than the vesicle recruitment assay. Although the
280 E84Q mutant as well as any double and triple EF-hand mutants were highly destabilized (See
281 input in Figure 5- figure supplement 1A), centriolar NCS1 signal intensity of the mutant was
282 reduced in parallel to its diminished expression level. This suggests that the first EF hand is
283 indispensable for stability of NCS1. E120Q mutant had similar expression level, but its

284 centrosomal signal was significantly reduced (Figure 5- figure supplement 1B), consistent with
285 its diminished interaction with CEP89 (see IP: GFP in Figure 5- figure supplement 1A), a protein
286 that recruits NCS1 to the mother centriole (Figure 2L). This suggests that the second EF-hand is
287 involved in keeping its structure to interact with CEP89. E168Q had a negligible effect in
288 stability and localization of NCS1. The ciliation assay revealed that none of single EF-hand
289 mutants showed significant cilium formation defect (Figure 5- figure supplement 1C) despite the
290 partial reduction of centriolar signal intensity for E84Q and E120Q. The double or triple mutants
291 almost completely failed to rescue ciliation defect of NCS1 knockout cells (Figure 5-figure
292 supplement 5C), reflecting their very low expression level (Figure 5-figure supplement 1A).
293 These results suggest that calcium binding is primarily required for the structure and stability of
294 NCS1 and NCS1 does not clearly exhibit a calcium-myristoylation switch. The structural role of
295 calcium on NCS1 is largely consistent with NCS1's high binding affinity to calcium (-90 nM)
296 (Aravind et al., 2008).

297 **NCS1 is recruited to the centriole in a microtubule-independent manner where it captures**
298 **ciliary vesicles**

299 We next sought to understand where NCS1 captures ciliary vesicle. One possibility is that NCS1
300 captures the ciliary vesicle in the cytoplasm and then traffics it to the centriole by dynein-
301 dependent transport via microtubule. Another possibility is that NCS1 traffics to the centriole
302 first and then captures ciliary vesicles. To distinguish these two possibilities, we treated RPE
303 cells with nocodazole to destabilize microtubules, as microtubules were previously shown to be
304 indispensable for ciliary vesicle recruitment (C. T. Wu, Chen, & Tang, 2018). Consistent with
305 the previous report (C. T. Wu et al., 2018), destabilization of microtubule by nocodazole (Figure
306 6A and B) immediately inhibited ciliary vesicle recruitment and subsequent cilium formation

307 (Figure 6C and D), suggesting that ciliary vesicles are trafficked to the mother centriole via
308 microtubules. In contrast, centriolar NCS1 signal was gradually increased upon serum starvation
309 even in the presence of nocodazole (Figure 6E), suggesting that NCS1 accumulates at the distal
310 appendage by microtubule-independent mechanisms, possibly by diffusion, similar to the
311 previously proposed diffusion-to-capture model of IFT trafficking to the ciliary base (Hibbard,
312 Vazquez, Satija, & Wallingford, 2021). Because NCS1 is an N-terminally myristoylated protein,
313 we also considered whether NCS1 might be trafficked to the distal appendage through UNC119,
314 a chaperone that binds to N-myristoylated ciliary proteins like NPHP3 and cystin and traffics
315 them to the primary cilium (K. J. Wright et al., 2011). We conclude that NCS1 unlikely uses
316 UNC119 pathway, as we did not observe UNC119A/UNC119B in our AP/MS analysis of
317 CEP89 (Figure 1B-Source Data), nor in purifications of UNC119A/UNC119B proteins
318 themselves (K. J. Wright et al., 2011). In a complementary approach to the microtubule
319 destabilization, we tested if NCS1 localizes to the distal appendage even if the ciliary vesicle
320 recruitment is inhibited by RAB34 depletion (see Figure 4B and C of (Tomoharu Kanie et al.,
321 2023)). We confirmed that centriolar NCS1 was comparable between control (sgSafe) and
322 RAB34 knockout cells (Figure 6F), suggesting that NCS1 is recruited to the centriole
323 independently from the ciliary vesicle. These results suggest that NCS1 moves to the distal
324 appendage possibly by diffusion or an alternative trafficking mechanism and there it captures the
325 ciliary vesicle that is trafficked to the centriole by microtubule-dependent trafficking.

326 **NCS1 localizes to the ciliary base in neuronal and non-neuronal cells**

327 While the majority of papers to date focused on the role of NCS1 in neurons given its original
328 discovery as a protein that facilitates neurotransmitter release (Pongs et al., 1993), expression
329 analysis revealed that the protein is expressed ubiquitously in non-neuronal tissues (Gierke et al.,

330 2004). Since we discovered that NCS1 localizes to the centriole, a major microtubule organizing
331 center in animal cells (Bornens, 2012), we tested the expression and the localization of NCS1 in
332 neuronal and non-neuronal cell types. We first tested the expression of NCS1 in various murine
333 tissues and confirmed that NCS1 is expressed in a wide-range of tissues (Figure 7-figure
334 supplement 1A). The low expression level of NCS1 in liver, skeletal muscle, and fat might
335 reflect that most of the cells (hepatocyte, myocyte, and adipocytes, respectively) in those tissues
336 do not retain cilia, or because of the difference in ratio between intracellular and extracellular
337 proteins. When we performed immunofluorescence assay, NCS1 localized to both cytoplasm and
338 the ciliary base (a dot next to ciliary markers, ARL13B or AC3) in isolated hippocampal neuron
339 (top panel in Figure 7A) as well as cells in hypothalamus (Figure 7B) and the dentate gyrus of
340 the hippocampus (Figure 7-figure supplement 2C). Both cytoplasmic and the centriole signal was
341 specific for NCS1 as we detected no signal in NCS1 knockout cells (bottom panel in Figure 7A
342 and B, and Figure 7-figure supplement 2C). NCS1 also localized to the ciliary base in virtually
343 all the non-neuronal ciliated cells that we tested, including kidney epithelia, pancreatic islet cells,
344 airway epithelia, ependymal cells, and mouse embryonic fibroblasts (MEFs) (Figure 7C and D,
345 Figure 7-figure supplement 2A-D). Only ciliated cells where we failed to detect NCS1 at the
346 ciliary base was photoreceptor cells (Figure 7-figure supplement 2E). We next sought to
347 determine whether NCS1 is involved in cilium formation in those cells, as we saw in RPE cells
348 (Figure 3A and B). In MEFs, cilium formation is modestly perturbed in Ncs1 depleted cells
349 (Figure 7E and F), consistent with the kinetic cilium formation defect in RPE cells (Figure 3A).
350 Decrease in ciliary ARL13B signal was also detected in *Ncs1*$^{-/-}$ MEFs (Figure 7F), similar to
351 NCS1 knockout RPE cells (Figure 3-figure supplement 1). In contrast, we did not detect a
352 measurable cilium formation defect in hippocampal neurons that lack Ncs1 (Figure 7G), whereas

353 the signal of ciliary membrane protein, type III adenylyl cyclase (ADCY3) (Bishop, Berbari,
354 Lewis, & Mykytyn, 2007) (Berbari, Bishop, Askwith, Lewis, & Mykytyn, 2007), was
355 significantly decreased (Figure 7H). Other ciliary GPCRs, such as SSTR3 and GPR161, were
356 also decreased in *Ncs1*$^{-/-}$ neurons, but did not show statistical significance with the small number
357 of samples analyzed (Figure 7-fiure supplement 3A and B). The difference in the cilium
358 formation defect in different cell types (modest ciliation defects in RPE and MEFs, but no defect
359 in neurons) as well as potential signaling function of NCS1 will be discussed in the Discussion.

360 ***Ncs1* knockout mice exhibit obesity, but not other phenotypes related to ciliopathies**

361 To date, NCS1 has been characterized mainly in neuronal aspects, as NCS1 was classically
362 believed to be a neuron-specific calcium sensor (Olafsson et al., 1997). Ncs1 was shown to be
363 essential for memory formation in C. elegans. Mice lacking Ncs1 exhibited impairment of
364 memory formation (de Rezende et al., 2014; Saab et al., 2009) (Nakamura et al., 2017). Since
365 NCS1 is now shown to localize to the distal appendage in both neuronal and non-neuronal cells
366 and regulate efficient cilium formation at least in some cell types, we sought to test if *Ncs1*
367 knockout mice show phenotypes related to ciliopathies, pleiotropic disorders caused by
368 functional and structural dysfunction of cilia (Reiter & Leroux, 2017). A series of previous
369 mouse genetic studies showed that the loss of ciliary function in mice result in partially penetrant
370 pre-weaning lethality, obesity, retinal degeneration, and male infertility (Nishimura et al., 2004)
371 (Ding et al., 2020; Fath et al., 2005; Mykytyn et al., 2004). We assessed whether the previously
372 generated *Ncs1*$^{-/-}$ mice (Hermainski, 2012; Ng et al., 2016) exhibit ciliopathy phenotypes.
373 Inconsistent with the previous two reports (Nakamura et al., 2011) (Dickinson et al., 2016),
374 which generated *Ncs1* knockout mice independently, our *Ncs1*$^{-/-}$ mice did not exhibit pre-
375 weaning lethality (Figure 7A, p=0.369 in Chi-square test in data with male and female

376 combined). The difference between our data and the previous studies might derive from the
377 background of mice (C57BL6/J in our study and C57BL6/N in the previous studies). When body
378 weight was analyzed, both male and female *Ncs1*$^{-/-}$ mice became more obese than their
379 littermates starting at 9-10 weeks of age, and gained 10% more weight than the controls at 20
380 weeks (Figure 7B-C). The obesity phenotype is consistent with the previous reports (Nakamura
381 et al., 2011; Ratai et al., 2019) and is similar to what was observed in cilia-defective mice, which
382 became obese starting between 8-12 weeks (Ding et al., 2020; Fath et al., 2005; Mykytyn et al.,
383 2004; Nishimura et al., 2004). *Ncs1*$^{-/-}$ accumulated more fat than their littermate *Ncs1*$^{+/-}$ mice,
384 suggesting that the obesity phenotype at least partially comes from the increased fat amount in
385 *Ncs1*$^{-/-}$ mice. We also assessed other ciliopathy phenotypes, but *Ncs1*$^{-/-}$ did not show other cilia-
386 related symptoms, such as retinal degeneration (judged by thickness of outer nuclear layer),
387 polycystic kidney, and male infertility (Figure 8E-H). The absence of retinal degeneration, one of
388 the most penetrant phenotypes besides obesity in Bardet-Biedl syndrome (Forsythe & Beales,
389 2013) (Forsyth & Gunay-Aygun, 2020), might reflect the lack of Ncs1 at the ciliary base in
390 photoreceptors (Figure 7-figure supplement 2E). The milder phenotype of *Ncs1*$^{-/-}$ mice than the
391 previously reported cilia-defective mice may reflect mild-modest cilium formation defect of
392 *Ncs1*$^{-/-}$ mice (Figure 7E and G). Further investigations are needed to determine whether the
393 obesity phenotype singularly come from cilia defect, and how exactly dysfunction of cilia leads
394 to obesity in *Ncs1*$^{-/-}$ mice.

395 **Discussion**

396 In 1962, Sorokin described through electron micrographs that cilium biogenesis in fibroblasts is
397 initiated by attachment of a small vesicle to the distal end of the centriole (S. Sorokin, 1962), or
398 more precisely to the distal appendage of the mother centriole (Schmidt et al., 2012). Since the

399 distal appendage proteins that have been discovered so far (CEP83 (Tanos et al., 2013), CEP164
400 (Graser et al., 2007), TTBK2 (Cajanek & Nigg, 2014), SCLT1 (Tanos et al., 2013), FBF1 (Tanos
401 et al., 2013), CEP89 (Sillibourne et al., 2011), ANKRD26 (Bowler et al., 2019), LRRC45
402 (Kurtulmus et al., 2018)) lack apparent lipid binding motifs, how exactly the ciliary vesicle is
403 captured by the distal appendage is poorly understood. In an accompanying paper, we screened
404 all the previously and newly discovered distal appendage proteins and found that CEP89 is
405 important for ciliary vesicle recruitment but not for other processes of cilium formation, such as
406 IFT and CEP19 recruitment (see Figure 6 of (Tomoharu Kanie et al., 2023)). Since CEP89 also
407 lacks any identifiable lipid binding domain, we hypothesized that an interactor of CEP89 would
408 be directly involved in the ciliary vesicle recruitment. In this paper, we discovered NCS1 as a
409 stoichiometric interactor of CEP89. We further show that NCS1 captures the ciliary vesicle via
410 its myristoylation motif.

411 **How NCS1 captures ciliary vesicles only at distal appendages?**

412 To make cilium formation efficient and error-free, we assume that the cells would have
413 mechanisms where NCS1 only captures the ciliary vesicle at the distal appendage but not at other
414 location of the cells (e.g. cytoplasm). In addition to its centriolar localization, NCS1 localizes
415 throughout cytoplasm, of which signal is completely lost in NCS1 knockout cells (Figure 2A).
416 This implies that NCS1 may sequester its myristoylation motif to remain in cytoplasm and may
417 expose the membrane association motif to capture the ciliary vesicle only at the distal
418 appendage. One very intriguing possibility is that NCS1 may protrude its myristoyl group in
419 response to increase in local calcium concentration (calcium-myristoyl switch), as shown in
420 other NCS family proteins, such as Recoverin and Hippocalcin (Ames et al., 1997; O'Callaghan
421 et al., 2003). The local calcium concentration may be higher at the centriole because of the high

422 calcium concentration in the cilium (Delling, DeCaen, Doerner, Febvay, & Clapham, 2013). We
423 addressed this question by making a series of EF-hand mutants of NCS1, where the amino acids
424 at the -z position required for calcium binding were mutated. Our data emphasizes the
425 importance of calcium in the stability of NCS1 (Figure 5-figure supplement 1A). As long as the
426 expression level of NCS1 is maintained, the mutation did not strongly affect either centriolar
427 localization or cilium formation (Figure 5-figure supplement 1B and C). These data suggest that
428 calcium may be required for the structural integrity of NCS1 but may not regulate protrusion of
429 myristoyl moiety, which is required for efficient ciliary vesicle recruitment and subsequent
430 cilium formation (Figure 5E and F). Our data aligns with the previous reports that suggest the
431 absence of calcium-myristoyl switch in NCS1 (Ames et al., 2000; O'Callaghan et al., 2002)
432 (Lemire et al., 2016). The second possibility is that NCS1 exposes its myristoyl group only when
433 the protein binds to another protein at the distal appendage. Given that CEP89 recruits NCS1 to
434 the distal appendage (Figure 2L), we wondered if NCS1 associates with membranes only when
435 the protein binds to CEP89. However, a fractionation experiment showed that NCS1 purifies
436 with the membrane fraction even in the absence of CEP89 (Figure 5A), indicating the absence of
437 CEP89-myristoyl switch. The third possibility is that NCS1 continuously expose its
438 myristoylation motif but remains in cytoplasm because of a weak membrane association. This
439 hypothesis is in agreement with the low affinity of myristoylated peptides for lipid with the
440 dissociation constant of 100 μM, which is barely sufficient to keep its membrane association
441 (Peitzsch & McLaughlin, 1993). Myristoylated proteins typically require additional mechanisms
442 to bind membranes (M. H. Wright, Heal, Mann, & Tate, 2010): 1) another acyl chain (e.g.,
443 palmitoylation), 2) a cluster of basic amino acids that help association with negatively charged
444 head group of the membrane, 3) an interacting partner that has affinity for membrane. Since

445 NCS1 does not appear to have another acyl chain, membrane binding of NCS1 is likely enhanced
446 by either basic amino acids or another distal appendage protein that is in close proximity to
447 NCS1 keeps the protein associated with membrane. Interestingly, a recent paper showed that
448 lysine residues at position 3, 7, and 9 may be also involved in membrane binding of NCS1
449 (Baksheeva et al., 2020). In terms of the binding partner induced membrane association, this
450 process is likely regulated by yet unknown distal appendage protein(s) and not by CEP89 as
451 membrane association of NCS1 does not require CEP89 (Figure 5A). The rise in the local
452 concentration of NCS1 as well as membrane vesicle at the centriole may also help NCS1's
453 membrane association at that location. The weak association between myristoylated NCS1 and
454 membrane could also explain why cells can capture ciliary vesicles, albeit less efficiently, even
455 in the absence of NCS1 (Figure 3C and 5F). We currently do not have an obvious candidate for a
456 distal appendage protein that may compensate the lack of NCS1, as the depletion of NCS1 in any
457 of the knockouts of the known distal appendage proteins did not further inhibit the ciliary vesicle
458 recruitment and cilium formation (Figure 4B-D). Future study will focus on identifying
459 additional protein(s) that recruit the ciliary vesicle to the centriole.

460 **How the ciliary vesicle is transported to the distal appendage.**

461 Our model suggests that the ciliary vesicle is recruited to the distal appendage in a microtubule-
462 dependent manner, whereas NCS1 can reach to the mother centriole without intact microtubules
463 (Figure 6). How is the ciliary vesicle recruited to the distal appendage? Classically, subdistal
464 appendages were considered as the site where the microtubule anchoring occurs, as the electron
465 micrograph showed that microtubule are in contact with the head of the subdistal appendage (see
466 Figure 12 of the (Vorobjev & Chentsov Yu, 1982)). The subdistal appendage localization of
467 Ninein, which was shown to be indispensable for microtubule anchoring at the centriole

468 (Delgehyr, Sillibourne, & Bornens, 2005), further supports that subdistal appendages are the
469 contact site of the microtubule. Therefore, one can hypothesize that the ciliary vesicle is
470 transported first to the subdistal appendage and then subsequently moves to the distal appendage
471 by an unknown mechanism. Interestingly, CEP89 and its interactors, NCS1 and C3ORF14, each
472 localize to positions near the subdistal appendage in addition to their distal appendage
473 localization (Figure 2D and F) (Chong et al., 2020). NCS1 may bind to ciliary vesicle at the
474 subdistal appendage and then move to the distal appendage to anchor the vesicle and promote
475 cilium formation. Possibly this process is rapid, so that any vesicle attached to the subdistal
476 appendage has never been observed in electron micrographs. However, this model conflicts with
477 the observation that subdistal appendages are dispensable for cilium formation (Mazo, Soplop,
478 Wang, Uryu, & Tsou, 2016). Alternatively, microtubules may populate a structural site around
479 the distal appendages as shown by recent dSTORM imaging (Chong et al., 2020). γ-tubulin
480 observed in vicinity of the distal appendage may nucleate those microtubules. If this is the case,
481 the ciliary vesicle may be transported directly to the distal appendage and then be captured by
482 NCS1. To address this question, it would be greatly informative if the entire ciliary vesicle
483 recruitment process could be visualized by super-resolution microscopy in live cells in a future
484 study. Another important question is whether NCS1 specifically recognizes a receptor on the
485 ciliary vesicle or NCS1 randomly captures the membrane of vesicles that arrive at the distal
486 appendage. NCS1 may recognize specific vesicles via the membrane curvature or specific lipid
487 components. Interestingly, a recent study showed that NCS1 preferentially binds to
488 phosphatidylinositol-3-phosphate (Baksheeva et al., 2020). This warrants future study.

489 **Requirement of NCS1 in cilium formation differs among cell types**

490 Cilium formation can be classified into two types (S. P. Sorokin, 1968) (Molla-Herman et al.,

491 2010): 1) the intracellular pathway, which is initiated by ciliary vesicle recruitment to the distal
492 appendage, and 2) the extracellular pathway, where the centriole first docks to plasma
493 membrane. While specific cell types have been observed to selectively use one of the two
494 pathways, the distinction between the pathways might not be so definite. For example, mouse
495 inner medullary collecting duct cells (mIMCD3), typically classified as using the extracellular
496 pathway, can use the intracellular pathway in less confluent cells (Stuck et al., 2021).
497 Nonetheless, the requirement for RAB34, a ciliary vesicle marker, in ciliogenesis is more
498 pronounced in the cells that use the intracellular pathway (Ganga et al., 2021; Oguchi, Okuyama,
499 Homma, & Fukuda, 2020; Stuck et al., 2021), indicating that ciliary vesicle recruitment is an
500 indispensable step for that pathway. Our data showed that cilium formation is modestly affected
501 by NCS1 depletion in the cell types that are known to use intracellular pathway (Molla-Herman
502 et al., 2010), such as RPE and MEFs (Figure 3A and Figure 7E). While the ciliogenesis pathway
503 is not well characterized in neurons, the presence of the ciliary pocket, a sign of the intracellular
504 pathway (Molla-Herman et al., 2010), is apparent in electron micrographs of neurons and neural
505 progenitors (Barnes, 1961; Brechbuhl, Klaey, & Broillet, 2008; Breunig et al., 2008; Dingemans,
506 1969; Han et al., 2008; Mirzadeh, Merkle, Soriano-Navarro, Garcia-Verdugo, & Alvarez-Buylla,
507 2008). Thus, we can predict that neurons would use the intracellular pathway. However,
508 inconsistently with RPE and MEFs, we did not observe a ciliary formation defect in cultured
509 hippocampal neurons isolated from E18.5 mice, suggesting that the requirement for NCS1 may
510 differ among cell types even though they use the same cilium formation pathway. Another
511 possible explanation for a failure to see cilium formation defects is that it is not easy to assess the
512 kinetics of ciliation in isolated hippocampal neurons because culture conditions are very different
513 from RPE cells. Notably, cilium formation is not induced by serum starvation in isolated

514 hippocampal neurons. In tissues *in vivo*, it was not easy to assess whether the *Ncs1*$^{-/-}$ mice have
515 fewer cilia than the control mice for several reasons. First, cilium structure is greatly affected by
516 sample preparation. For example, we cannot visualize cilia if we do not fix the tissues by cardiac
517 perfusion with 4% paraformaldehyde and it is difficult to achieve perfectly efficient perfusion.
518 Second, orientation of cilia is affected by the orientation of how the tissue is sectioned and it is
519 thus difficult to analyze cilia that elongate perpendicularly to the slice. Therefore, we could not
520 test whether NCS1 is required for cilium formation in cells that typically use extracellular
521 pathway. These questions warrant future studies. Importantly, we did observe a decrease in
522 ciliary localization of several membrane proteins, such as ARL13B (Figure 3-figure supplement
523 1A-C) and ADCY3 (Figure 7H) in *Ncs1*$^{-/-}$ cells, even when the percentage of ciliated cells was
524 comparable to the control cells. This may suggest that NCS1 might be involved in recruiting
525 membrane signaling proteins to the cilium besides its function in ciliary vesicle recruitment and
526 cilium formation. It would be interesting to test in the future study if other ciliary membrane
527 proteins are also brought to the cilium via ciliary vesicles.

528 ***NCS1* may be a ciliopathy gene**

529 Given that NCS1 is involved in ciliary vesicle recruitment and subsequent cilium formation, we
530 tested if *Ncs1*$^{-/-}$ mice exhibit ciliopathy phenotypes. Our data showed that *Ncs1*$^{-/-}$ mice display a
531 modest obesity phenotype, but no other apparent ciliopathy related phenotypes, including retinal
532 degeneration. The absence of retinal degeneration may be explained by the lack of Ncs1 at the
533 ciliary base in photoreceptors. A possible explanation for the lack of other ciliopathy phenotypes
534 is the partial penetrance of these other symptoms. In human, obesity and retinal degeneration is
535 observed in most Bardet-Biedl syndrome patients (-90%), whereas other phenotypes, such as
536 hypogonadism and kidney disease are often absent (Forsyth & Gunay-Aygun, 2020). Mice

537 lacking the distal appendage protein, FBF1(Zhang et al., 2021) or ANKRD26 (Acs et al., 2015)
538 (Bera et al., 2008), or the distal appendage associate protein, CEP19 (Shalata et al., 2013),
539 display morbid obesity with few other ciliopathy-related phenotypes (e.g., preweaning lethality
540 and hydrocephalus in *Fbf1*$^{-/-}$ and male infertility in *Cep19*$^{-/-}$ mice). Interestingly, our data
541 revealed that knockouts of each of these genes show a kinetic defect in ciliation, but the cells
542 also are observed to eventually catch up for cilium formation (Figure 5A and B in (Tomoharu
543 Kanie et al., 2023) paper for ANKRD26 and FBF1) (Figure 3C of (T. Kanie et al., 2017) for
544 CEP19). This phenotype is almost identical to what was observed in CEP89 or NCS1 knockout
545 cells (Figure 3A), suggesting that mild cilium formation defect may result in obesity with few
546 other ciliopathy-related defects. Another explanation for the lack of other ciliopathy phenotypes
547 besides obesity is the background of our *Ncs1*$^{-/-}$ mice (C57BL6/J). It is well known that depletion
548 of the same gene could cause different severity of the phenotypes in different background of
549 mice. For example, mice lacking Bbip10, a BBSome associated protein (Loktev et al., 2008), in
550 pure C57BL6/J background show complete perinatal lethality, while approximately half of the
551 *Bbip10*$^{-/-}$ mice in 129/SvJ background can survive into adulthood (Loktev & Jackson, 2013).
552 Interestingly, two independent reports showed that *Ncs1*$^{-/-}$ exhibit partial (-50%) preweaning
553 lethality (Dickinson et al., 2016; Nakamura et al., 2011) in C57BL6/N mice. The difference in
554 the severity of the phenotypes in *Ncs1*$^{-/-}$ mice between previous reports and our results may be
555 explained by the difference between C57BL6/J and C57BL6/N. Genetic and phenotypic
556 differences between these two strains were extensively described in the previous paper (Simon et
557 al., 2013). Thus, NCS1 may be a ciliopathy gene and obesity caused by NCS1 depletion may be
558 attributable to ciliary defect. This warrants future genetic study. If obesity accompanied with
559 NCS1 depletion is due to a cilia defect, what kind of cilia defect exist in the *Ncs1* defective

560 animals *in vivo*? A simple defect may be the reduced number of ciliated cells because of the
561 cilium formation defect. While we did not see an apparent decrease in the number of cilia in
562 *Ncs1*$^{-/-}$ mice in any tissues that we examined (e.g., brain, kidney, pancreatic islets, and airway
563 epithelia) (Figure 7B-D, Figure 7-figure supplement 2), more accurate characterization is needed
564 to make a conclusion. It is possible that cilium formation is abolished in developmentally and
565 spatially regulated manner, so that the defect may be only apparent in specific cell types and
566 developmental stage. Another possibility that may cause cilia-related obesity phenotype in *Ncs1*$^{-}$
567 $^{/-}$ mice is that localization of some of the ciliary membrane proteins may be abolished in *Ncs1*$^{-/-}$
568 cells as shown in the cultured hippocampal neurons (Figure 7H). Unfortunately, it is not easy to
569 assess the number and morphology of the cilia as well as signal intensity of the ciliary membrane
570 proteins *in vivo* because of the issues described above. Technical improvement in the future may
571 allow us to more accurately characterize the cilia *in vivo* and determine whether ciliary defects in
572 *Ncs1*$^{-/-}$ mice indeed cause obesity. Alternatively, it would be interesting to see if *Cep89* knockout
573 mice display the similar phenotypes as *Ncs1* knockout mice.

574 **The connection between NCS1-related neurological disorder and cilia defect.**

575 NCS1 has been shown to participate in memory formation in *C. elegans* (Gomez et al., 2001) and
576 mice (Saab et al., 2009) (Nguyen et al., 2021) (Nakamura et al., 2017; Ng et al., 2016) (de
577 Rezende et al., 2014). While the neurological phenotypes in *Ncs1*$^{-/-}$ mice are not consistent
578 across studies, possibly because of the differences in mouse background, it seems that many
579 studies agree that the overall phenotypes are mild, and the mice display defects in memory
580 formation, when tested for novel object recognition (de Rezende et al., 2014) or displaced object
581 recognition (Mun et al., 2015; Ng et al., 2020; Nguyen et al., 2021). It is intriguing to consider
582 whether the memory formation defect in *Ncs1*$^{-/-}$ mice is attributable to ciliary defects. Several

583 lines of evidence suggest that loss of cilia in brain results in memory formation defects. If IFT88,
584 an IFT component critical for formation of the cilium, is depleted in telencephalon by Emx-1
585 Cre, the mice display impaired recognition memory assessed through novel object recognition
586 test (Berbari et al., 2014). The depletion of IFT20 in dentate gyrus of the hippocampus using
587 AAV-CAMKII-Cre caused the defect in displaced object recognition test (Rhee, Kirschen, Gu,
588 & Ge, 2016). Both mice lacking ADCY3 or SSTR3, ciliary membrane proteins that are
589 prominent in neurons (Bishop et al., 2007), exhibit defect in novel object recognition (Einstein et
590 al., 2010; Wang, Phan, & Storm, 2011). The similarity between cilia-defective mice and *Ncs1*$^{-/-}$
591 mice may suggest that the memory formation defect in *Ncs1*$^{-/-}$ deficient mice may be due to
592 ciliary dysfunction. It would be interesting to test whether SSTR3 agonist, which induces long-
593 term potentiation (LTP) (Einstein et al., 2010) likely via binding to the ciliary G-protein coupled
594 receptor, SSTR3, can induce LTP in *Ncs1*$^{-/-}$ mice. It would be also interesting to see if Cep89
595 depletion in mice causes similar memory formation defect, since NCS1 knockouts and CEP89
596 knockouts showed almost identical cilium formation defects (Figure 3). The importance of cilia
597 in neurological deficiencies should be an area of extensive future study.
598

599 **Author Contributions**

600 Conceptualization, T. K. and P. K. J.; Methodology, T. K., R.N., K.A., and P. K. J.;
601 Investigation, T. K., R.N., K.A., and P. K. J.; Writing – Original Draft, T. K.; Writing – Review
602 & Editing, T. K., R.N., K.A., O.P., and P. K. J.; Funding Acquisition, T.K. and P. K. J.;
603 Resources, T.K. and P. K. J.; Supervision, T. K. and P. K. J.
604

605 **Acknowledgments**

606 We thank Drs. Albert Wong and John Georgiou for providing *Ncs1* knockout mice. We thank
607 Dr. Jonathan Mulholland for technical advice on the 3D-SIM experiments. We thank Mr. John
608 Perrino for technical support for sample preparation for the electron microscopy experiments.
609 We thank members of the Jackson lab for helpful discussion and advice. 3D-SIM experiments
610 were performed at the Stanford Cell Sciences Imaging Facility and were supported by Award
611 Number 1S10OD01227601 from the National Center for Research Resources (NCRR). Electron
612 microscopy observation was performed at the Stanford Cell Sciences Imaging Facility and were
613 supported by National Institutes of Health (NIH) S10 Award Number 1S10OD028536-01, titled
614 "OneView 4kX4k sCMOS camera for transmission electron microscopy applications". The cell
615 authentication service performed by MTCRO-COBRE Cell line authentication core of the
616 University of Oklahoma Health Science Center was supported partly P20GM103639 and
617 National Cancer Institute Grant P30CA225520 of NIH. This project was support by funds from
618 the Baxter Laboratory for Stem Cell Research, the Stanford Department of Research, the
619 Stanford Cancer Center, NIH grants R01GM114276 and R01GM121565 to PKJ, NIH grant
620 P20GM103447 and a seed grant from Presbyterian Health Foundation (GRF00006006) to TK.
621

622 **Materials and Methods**

623 **Plasmids**

624 pMCB306, a lenti-viral vector containing loxP-mU6-sgRNAs-puro resistance-EGFP-loxP
625 cassette, and P293 Cas9-Blue Fluorescent Protein (BFP) were gifts from Prof. Michael Bassik.
626 Lenti-virus envelope and packaging vector, pCMV-VSV-G and pCMV-dR8.2 dvpr respectively,
627 were gifts from Prof. Bob Weinberg (Addgene plasmid #8454 and #8455).
628 pOG44 (V600520) was obtained from Thermo Fisher Scientific.

629 Lentiviral vectors containing single guide RNAs (sgRNAs) were generated by ligating 50 fmol
630 oligonucleotides encoding sgRNAs into 25 ng of the pMCB306 vector digested with BstXI
631 (R0113S, NEB) and BlpI (R0585S, NEB) restriction enzymes along with 0.25 μl of T4 ligase
632 (M0202S, NEB) in 2.5 μl total reaction volume. Before ligation, 4 μM of forward and reverse
633 oligonucleotides listed in the supplementary table were annealed in 50 μl of annealing buffer
634 (100 mM potassium acetate, 30 mM HEPES (pH7.4), and 3mM magnesium acetate) at room
635 temperature following denaturation in the same buffer at 95°C for 5 minutes. The targeting
636 sequence for sgRNAs are listed in the supplementary table "Source Data 1-Primers used for
637 genomic PCR and for generating sgRNA vectors". The guide RNA targeting sequence for
638 pMCB306-sgNCS1 vector used to create cells lacking both NCS1 and each of the other distal
639 appendage proteins shown in Figure 4 is the same as the one used to make NCS1 knockout cells.
640 The knockout cells for other distal appendage proteins were described in an accompanying paper
641 (Tomoharu Kanie et al., 2023).
642 pG-LAP6/puro vector (pCDNA5/TO/FRT/EGFP-TEV cleavage site-S tag-PreScission cleavage
643 site/DEST) used for the tandem affinity purification experiment was previously described (T.
644 Kanie et al., 2017). Gateway cloning compatible lentiviral vectors, pWPXLd/LAP-N/puro/DEST
645 vector and pWPXLd/LAP-C/puro/DEST vector, were previously described (T. Kanie et al.,
646 2017). pWPXLd/LAP-N/blast/long EF/DEST was created by inserting N-terminally LAP tag
647 (EGFP-TEV cleavage site-S tag-PreScission cleavage site)/DEST/blasticidin resistance cassette
648 into a second generation lenti-viral vector, pWPXLd. pWPXLd vector was a gift from Prof.
649 Didier Trono (Addgene plasmid #12258). pWPXLd/LAP-C/blast/long EF/DEST vector was
650 created by inserting DEST/C-terminally LAP tag/blasticidin resistance cassette into the pWPXLd
651 vector. pWPXLd/FLAG-N/blast/DEST vector was created by inserting FLAG/DEST/blasticidin

652 resistance cassette into the pWPXLd vector. All the lenti-viral vectors were propagated in Stbl3
653 competent cells to reduce unwanted recombination of long terminal repeat of the vectors.
654 pCS2-N-terminal 5×MYC/DEST and pCS2-N-terminal 3×HA/DEST (used for in vitro
655 translation) were created by inserting either 5×MYC tag or 3×HA tag and destination cassette
656 into pCS2+ vector, which contains Sp6 and CMV promoter.
657 The Gateway entry vector for Homo sapiens CEP89 was created by BP recombination using a
658 Polymerase Chain Reaction (PCR) product containing attB1 and attB2 site, which was amplified
659 using pCR4-TOPO-CEP89 (MHS6278-213243472, Open Biosystems) as a template. Gateway
660 entry vectors carrying truncation mutants of CEP89 (1-343a.a. and 344-783a.a.) were created by
661 using BP recombination between pDONR221 and PCR-amplified inserts.
662 The Gateway entry vectors for Homo sapiens NCS1 (HsCD00366520) and C3ORF14
663 (HsCD00365881) were obtained from Harvard plasmid. STOP codons were added or removed
664 by using Quick change mutagenesis if necessary. The Gateway entry vectors for NCS1 mutants
665 (myristoylation defective or EF-hand mutants) were created via Quick change mutagenesis using
666 the entry vector for NCS1 described above. The quick-change mutagenesis was performed by
667 PCR with a complementary primary set (forward and reverse) that has a point mutation in the
668 middle of the primers. Following the PCR, the PCR product was treated with 20U of DpnI
669 (R0176L, NEB) for 1 hour at 37°C to eliminate the template, and was then used to transform
670 competent cells.
671 The entry vectors for the CEP350 fragment (2470-2836 a.a.) and FGFR1OP (or FOP) was
672 previously described (T. Kanie et al., 2017).
673 Flp-In system compatible N-terminally LAP-tagged CEP89 was generated by LR recombination
674 between CEP89 entry vector and pG-LAP6/puro.

675 Lentiviral vector containing untagged CEP89 (minimal CMV promoter) was created by LR
676 recombination between CEP89 entry vector that contains a stop codon and
677 pWPXLd/LAPC/blast/minimal CMV/DEST vector.
678 Lentiviral vectors containing untagged NCS1 (long EF promoter or short EF promoter) were
679 created by LR recombination between NCS1 (wild-type and mutants) entry vectors that contain
680 stop codons and pWPXLd/LAPC/blast/long EF/DEST or pWPXLd/LAPC/blast/short EF/DEST
681 vectors.
682 N-terminally HA tagged CEP89, C3ORF14, and FGFR1OP (or FOP) vectors used for in vitro
683 binding assay were created by LR recombination between the respective entry vectors containing
684 a stop codon and the pCS2-N-terminal 3×HA/DEST vector. pCS2-N-terminal 5×MYC tagged
685 C3ORF14, NCS1, and the CEP350 fragment (2470-2836 a.a.) vectors were created by LR
686 recombination between the respective entry vectors that contain stop codons and the pCS2-N-
687 terminal 5×MYC/DEST vector.
688
689 **Cell line, Cell culture, Transfection, and Lentiviral expression**
690 hTERT RPE-1 cells and 293T cells were grown in DMEM/F-12 (12400024, Thermo Fisher
691 Scientific) supplemented with 10% FBS (100-106, Gemini), 1× GlutaMax (35050-079, Thermo
692 Fisher Scientific), 100 U/mL Penicillin-Streptomycin (15140163, Thermo Fisher Scientific) at
693 37°C in 5% CO_2. To induce cilium formation, cells were incubated in DMEM/F-12
694 supplemented with 1×GlutaMax and 100 U/mL Penicillin-Streptomycin (serum-free media).
695 Both cell lines were authenticated via a short-tandem-repeat based test. The authentication was
696 performed by MTCRO-COBRE Cell line authentication core of the University of Oklahoma
697 Health Science Center. Mycoplasma negativity of the original cell lines (hTERT RPE-1 and

698 293T) grown in antibiotics-free media were confirmed by a PCR based test (G238, Applied
699 Biological Materials).
700 RPE-FRT9 expressing N-terminally LAP tagged CEP89 used for tandem affinity purification
701 was generated by transfecting 150 ng of the preceding vectors with 850 ng of pOG44, followed
702 by selection with 10 μg/ml puromycin. Flp-In system compatible RPE cells (RPE-FRT9) were
703 previously described (Sang et al., 2011).
704 All other stable cell lines, including CRISPR knockout cells, were generated using lentivirus.
705 Lentivirus carrying either gene of interest or sgRNAs was produced by co-transfecting 293T
706 cells with 150 ng of pCMV-VSV-G, 350 ng of pCMV-dR8.2 dvpr, and 500 ng of lenti-viral
707 transfer plasmids previously described along with 3 μl of Fugene 6 (E2692, Promega)
708 transfection reagent. Media was replaced 24 hr after transfection to omit transfection reagent,
709 and virus was harvested at 48 hr post-transfection. Virus was then filtered with a 0.45 μm PVDF
710 filter (SLHV013SL, Millipore) and mixed with 4-fold volume of fresh media containing 12.5
711 μg/ml polybrene (TR-1003-G, Millipore). Following infection for 66 hr, cells were selected with
712 either 10 μg/ml puromycin (P9620, SIGMA-Aldrich) or 10 μg/ml blasticidin (30-100-RB,
713 Corning) for at least 10 days before subsequent analysis.
714
715 **CRISPR knockout**
716 RPE cells expressing BFP-Cas9 were generated by infection with lentivirus carrying P293 Cas9-
717 BFP, followed by sorting BFP-positive cells using FACSAria (BD). RPE-BFP-Cas9 cells were
718 then infected with lentivirus carrying sgRNAs in the pMCB306 vector to generate knockout
719 cells. After selection with 10 μg/ml puromycin, cells were subjected to immunoblotting,
720 immunofluorescence, or genomic PCR combined with TIDE analysis (Brinkman, Chen,

721 Amendola, & van Steensel, 2014) to determine knockout efficiency. The exact assay used for
722 each cell line is listed in "Source Data 7-summary of CRISPR knockout cells". Cells were then
723 infected with adenovirus carrying Cre-recombinase (1045N, Vector Biolabs) at a multiplicity of
724 infection of 50 to remove the sgRNA-puromycin resistance-EGFP cassette. 10 days after
725 adenovirus infection, GFP-negative single cells were sorted using FACSAria. The single cell
726 clones were expanded, and their knockout efficiency were determined by immunofluorescence,
727 Western blot, and/or genomic. The same number of validated single clones (typically three to
728 four different clones) were mixed to create pooled single cell knockout clones to minimize the
729 phenotypic variability occurred in single cell clones. The cells lacking both NCS1 and each of
730 the other distal appendage proteins shown in Figure 4 were created by infecting the knockout
731 cells with lenti-virus carrying sgNCS1. The experiments shown in Figure 4 were performed
732 without removing loxP-mU6-sgRNAs-puro resistance-EGFP-loxP cassette.
733 Cells used in the rescue experiments shown in Figure 3B, Figure 3- figure supplement 1A-C,
734 Figure 5A-F, and Figure 5- figure supplement 1A-C were created by infecting the respective
735 knockout cells with lenti-virus carrying untagged CEP89 or NCS1 (wild-type or mutants). To
736 rescue the ciliation defect of CEP89 knockout cells, the expression level of CEP89 was carefully
737 adjusted by using minimal CMV promoter to mimic endogenous CEP89 expression, since
738 overexpression of CEP89 under the control of long EF promoter significantly inhibited cilium
739 formation (data not shown).
740

741 **Tandem affinity purification**

742 5 mL packed cell volume of RPE-FRT9 cells expressing N-terminally LAP-tagged CEP89 were
743 re-suspended with 20 mL of LAP-resuspension buffer (300 mM KCl, 50 mM HEPES-KOH [pH

744 7.4], 1 mM EGTA, 1 mM $MgCl_2$, 10% glycerol, 0.5 mM dithiothreitol (DTT), and protease
745 inhibitors [PI88266, Thermo Scientific]), lysed by gradually adding 600 μL 10% NP-40 to a
746 final concentration of 0.3%, then incubated on ice for 10 min. The lysate was first centrifuged at
747 14,000 rpm (27,000 g) at 4°C for 10 min, and the resulting supernatant was centrifuged at 43,000
748 rpm (100,000 g) for 1 hr at 4°C to further clarify the lysate. High speed supernatant was mixed
749 with 500 μL of GFP-coupled beads (Torres, Miller, & Jackson, 2009) and rotated for 1 hr at 4°C
750 to capture GFP-tagged proteins, and washed five times with 1 mL LAP200N buffer (200 mM
751 KCl, 50 mM HEPES-KOH [pH 7.4], 1 mM EGTA, 1 mM $MgCl_2$, 10% glycerol, 0.5 mM DTT,
752 protease inhibitors, and 0.05% NP40). After re-suspending the beads with 1 mL LAP200N buffer
753 lacking DTT and protease inhibitors, the GFP-tag was cleaved by adding 5 μg of TEV protease
754 and rotating tubes at 4°C overnight. All subsequent steps until the cutting of bands from protein
755 gels were performed in a laminar flow hood. TEV-eluted supernatant was added to 100 μL of S-
756 protein agarose (69704-3, EMD Millipore) to capture S-tagged protein. After washing three
757 times with LAP200N buffer lacking DTT and twice with LAP100 buffer (100 mM KCl, 50 mM
758 HEPES-KOH [pH 7.4], 1 mM EGTA, 1 mM $MgCl_2$, and 10% glycerol), purified protein
759 complexes were eluted with 50 μL of 2×Lithium Dodecyl Sulfate (LDS) buffer (212 mM Tris-
760 HCl, 282 mM Tris-base, 4% LDS, 20% glycerol, 1.02 mM EDTA, 0.13% Brilliant Blue G250,
761 0.05% phenol red buffer) containing 10% DTT and boiled at 95°C for 3 min. Samples were then
762 run on Bolt® Bis-Tris Plus Gels (NW04120BOX, Thermo Fisher Scientific) in Bolt® MES SDS
763 Running Buffer (B000202, Thermo Fisher Scientific). Gels were fixed in 100 mL of fixing
764 solution (50% methanol, 10% acetic acid in Optima™ LC/MS grade water [W6-1, Thermo
765 Fisher Scientific]) at room temperature, and stained with Colloidal Blue Staining Kit (LC6025,
766 Thermo Fisher Scientific). After the buffer was replaced with Optima™ water, the bands were

767 cut into eight pieces, followed by washing twice with 500 μL of 50% acetonitrile in Optima™
768 water. The gel slices were then reduced and alkylated followed by destaining and in-gel
769 digestion using 125 ng Trypsin/LysC (V5072, Promega) as previously described (Shevchenko,
770 Tomas, Havlis, Olsen, & Mann, 2006) with the addition of Protease Max (V2071, Promega) to
771 increase digestion efficiency. Tryptic peptides were extracted from the gel bands and dried in a
772 speed vac. Prior to LC-MS, each sample was reconstituted in 0.1% formic acid, 2% acetonitrile,
773 and water. NanoAcquity (Waters) LC instrument was set at a flow rate of either 300 nL/min or
774 450 nL/min where mobile phase A was 0.2% formic acid in water and mobile phase B was 0.2%
775 formic acid in acetonitrile. The analytical column was in-house pulled and packed using C18
776 Reprosil Pur 2.4 μM (Dr. Maisch) where the I.D. was 100 μM and the column length was 20-25
777 cm. Peptide pools were directly injected onto the analytical column in which linear gradients (4-
778 40% B) were of either 80 or 120 min eluting peptides into the mass spectrometer. Either the
779 Orbitrap Elite or Orbitrap Fusion mass spectrometers were used, where a top 15 or "fastest"
780 MS/MS data acquisition was used, respectively. MS/MS was acquired using CID with a
781 collisional energy of 32-35. In a typical analysis, RAW files were processed using Byonic
782 (Protein Metrics) using 12 ppm mass accuracy limits for precursors and 0.4 Da mass accuracy
783 limits for MS/MS spectra. MS/MS data was compared to an NCBI GenBank FASTA database
784 containing all human proteomic isoforms with the exception of the tandem affinity bait construct
785 sequence and common contaminant proteins. Spectral counts were assumed to have undergone
786 fully specific proteolysis and allowing up to two missed cleavages per peptide. All data was
787 filtered and presented at a 1% false discovery rate (Elias & Gygi, 2007).
788
789 **Silver staining**

790 5μl of samples containing LDS buffer and DTT prepared for tandem affinity purification and
791 mass spectrometry described above were mixed with 0.5 μl of 500 mM iodoacetamide
792 (0210035105, MP Biomedicals). Proteins were separated in a 4-12% Bis-Tris gel (NP0321BOX,
793 Invitrogen), followed by fixation of the gel overnight in 50% methanol at room temperature.
794 The gel was impregnate with solution C (0.8% (w/v) silver nitrate (S6506, SIGMA), 207.2mM
795 ammonium hydroxide (A6899, SIGMA) and 18.9 mM sodium hydroxide) for 15 minutes,
796 followed by rinsing with water twice. The image was then developed in solution D (0.05% citric
797 and 0.0185% formaldehyde in Milli-Q) until intensity of the bands increase to optimal level. The
798 reaction was then terminated by adding stop solution (45% methanol and 10% acetic acid).
799

800 **Immunoblot**

801 For immunoblotting, cells were lysed in NP-40 lysis buffer (50 mM Tris-HCl [pH7.5], 150 mM
802 NaCl, 0.3% NP-40 [11332473001, Roche Applied Science]) containing 10 μg/ml LPC
803 (leupeptin, Pepstatin A, and chymostatin) and 1% phosphatase inhibitor cocktail 2 (P5726,
804 SIGMA). Following clarification of the lysate by centrifugation at 15,000 rpm (21,000 g) for 10
805 min, samples were mixed with 1× LDS buffer (106 mM Tris-HCl, 141 mM Tris-base, 2% LDS,
806 10% glycerol, 0.51mM EDTA, 0.065% Brilliant Blue G250, 0.025% phenol red) containing
807 2.5% 2-mercaptoethanol (M3148, SIGMA) and incubated at 95°C for 5 min. Proteins were
808 separated in an NuPAGE™ Novex™ 4-12% Bis-Tris protein gel (WG1402BOX, Thermo Fisher
809 Scientific) in NuPAGE™ MOPS SDS running buffer (50 mM MOPS, 50 mM Tris Base, 0.1%
810 SDS, 1 mM EDTA, pH 7.7), and transferred onto an Immobilon™-FL PVDF Transfer
811 Membrane (IPFL00010, EMD Millipore) in Towbin Buffer (25 mM Tris, 192 mM glycine, pH
812 8.3). Membranes were incubated in LI-COR Odyssey Blocking Buffer (NC9232238, LI-COR)

813 for 30 min at room temperature, and then probed overnight at 4°C with the appropriate primary
814 antibody diluted in the blocking buffer. Next, the membrane was washed 3 × 5 min in TBST
815 buffer (20 mM Tris, 150 mM NaCl, 0.1% Tween 20, pH 7.5) at room temperature, and incubated
816 with the appropriate IRDye® antibodies (LI-COR) diluted in the blocking buffer for 30 min at
817 room temperature. After washing three times in TBST buffer, the membrane was scanned on an
818 Odyssey CLx Imaging System (LI-COR) and proteins were detected at wavelengths 680 and 800
819 nm. Primary antibodies used for immunoblotting are listed in the "Source Data 4-List of the
820 antiboidies_CEP89-NCS1". Secondary antibodies used for immunoblotting were IRDye®
821 800CW donkey anti-rabbit (926-32213, LI-COR) and IRDye® 680CW donkey anti-mouse (926-
822 68072, LI-COR).
823
824 **Co-immunoprecipitation**
825 Cells were plated in a 10 cm dish and grown to confluent. Cells were then lysed with NP-40 lysis
826 buffer (50 mM Tris-HCl [pH7.5], 150 mM NaCl, and 0.3% NP-40) containing 10 μg/ml LPC
827 (leupeptin, Pepstatin A, and chymostatin) and 1% phosphatase inhibitor cocktail 2 (P5726,
828 SIGMA), followed by clarification of the lysate by centrifugation at 15,000 rpm (21,000 g) for
829 10 min. The protein concentration was measured by Bradford assay as described previously (see
830 procedure B step 8 in (T. Kanie & Jackson, 2018)). For GFP co-immunoprecipitation shown in
831 Figure 1D and Figure 5- figure supplement 1A, the soluble fraction was incubated with Protein A
832 beads cross-linked with rabbit anti-GFP antibody (Torres et al., 2009) (10 μl bed volume per 3
833 mg of lysate) with end-over-end rotation for 1.5 hr at 4°C. For co-immunoprecipitation with
834 endogenous NCS1 shown in Figure 1- figure supplement 1A, the lysate was incubated with
835 mouse monoclonal anti-NCS1 antibody (sc-376206, Santa Cruz) (1 μg of antibody per 4 mg of

836 lysate) for 1 hour with end-over-end rotation. The samples were then mixed with protein A beads
837 (20 μl bed volume) and incubated with end-over-end rotation for 1.5 hr at 4°C. After the
838 incubation with the beads (for both GFP co-IP and NCS1 co-IP), the samples were washed five
839 times with IP wash buffer (50 mM Tris-HCl [pH 7.5], 150 mM NaCl, and 0.1% NP-40). Samples
840 were then eluted with 2 × LDS buffer containing 2.5% 2-mercaptoethanol (M3148, SIGMA).
841
842 **Subcellular fractionation**
843 Cells were plated in a 15 cm dish at the density of 1.25×10^6 cells and grown in DMEM/F-12
844 media containing 10% FBS for 90 hours. Cells were detached from the plate using 0.05%
845 trypsin/EDTA (25300-054, Gibco) and pelleted down by centrifugation at 500 g at 4°C for 5
846 minutes. After washing once with 15 ml of ice cold low osmotic buffer (25mM HEPES-NaOH
847 (pH7.5), 0.5 mM $MgCl_2$), the cell pellet was re-suspended in 10 ml of the ice cold low osmotic
848 buffer and incubated on ice for 10 minutes to let the cells swollen. The swollen cells were
849 pelleted down and were re-suspended in 0.8 ml of the ice cold low osmotic buffer, followed by
850 nitrogen cavitation at 300 psi for 30 minutes on ice. The cavitate was centrifuged at 1000 g at
851 4°C for 10 minutes. The 1000 g supernatant was then centrifuged at 15,000 g at 4°C for 10
852 minutes. The 15,000 g supernatant was then transferred to an ultracentrifugation tube (343778,
853 Beckman) and ultracentrifuged at 100,000 g (R_{max}) in a TLA100.2 fixed angle rotor (Beckman) at
854 4°C for 1 hour. The supernatant samples were prepared by mixing 25 μl of supernatant from
855 each centrifugation speed with 25 μl of 2×LDS buffer containing 5% 2-mercaptoethanol. The
856 pellet samples were prepared by re-suspending the pellet with appropriate amount of 1× LDS
857 buffer containing 2.5% 2-mercaptoethanol.
858

859 ***In vitro* binding assay**

860 *Co-In vitro* translated (co-IVT) proteins were generated with pCS2-N-terminal 5×MYC vectors
861 and pCS2-N-terminal 3×HA vectors described above using TnT® Coupled Reticulocyte Lysate
862 System under the SP6 promoter (L4600, Promega) and by following manufacturer's
863 recommendations with few modifications. Briefly, instead of in vitro translating 1μg of plasmid
864 for each reaction, 0.5μg of HA-tagged protein along with 0.5μg of corresponding MYC-tagged
865 protein was co-translated. Note that we only observed the interaction between CEP89 and NCS1
866 when the two proteins were co-translated. The interaction between all the other proteins were
867 identical between original protocol and co-IVT. For each pull-down reaction, 50 μl of co-IVT
868 protein was added along with 5 μL (bed volume) of washed HA-beads (11815016001, Roche) in
869 300 μL binding buffer (25 mM HEPES-NaOH [pH 7.5], 500 mM NaCl, 1 mM CaCl2, and 0.1%
870 Triton X-100) and mixed for 2 hours at 4°C. The beads were washed five times with the same
871 buffer and eluted with 1×LDS buffer containing 2.5% 2-mercaptoethanol. The eluates were then
872 resolved by SDS-PAGE and analyzed by immunoblotting with anti-HA (901501, BioLegend)
873 and anti-MYC (ab9106, Abcam) antibodies.

874

875 **Transmission electron microscopy**

876 Either control (sgGFP) or NCS1 knockout RPE cells were grown to confluent on 12 mm round
877 coverslips (12-545-81, Fisher Scientific), followed by serum starvation for 3 hr. Cells were then
878 fixed with 4% paraformaldehyde (PFA) (433689M, Alfa Aesar) and 2% glutaraldehyde (G7526,
879 SIGMA) in sodium cacodylate buffer (100 mM sodium cacodylate and 2 mM $CaCl_2$, pH 7.4) for
880 1 hr at room temperature, followed by two washes with sodium cacodylate buffer. Cells were
881 then post fixed in cold/aqueous 1% osmium tetroxide (19100, Electron Microscopy Sciences) in

882 Milli-Q water for 1 hour at 4°C, allowed to warm to room temperature (RT) for 2 hours rotating
883 in a hood, and washed three times with Milli-Q water. The samples were then stained with 1%
884 uranyl acetate in Milli-Q water at room temperature overnight. Next, the samples were
885 dehydrated in graded ethanol (50%, 70%, 95%, and 100%), followed by infiltration in EMbed
886 812. Ultrathin serial sections (80 nm) were created using an UC7 (Leica, Wetzlar, Germany), and
887 were picked up on formvar/Carbon coated 100 mesh Cu grids, stained for 40 seconds in 3.5%
888 Uranyl Acetate in 50% Acetone followed by staining in Sato's Lead Citrate for 2 minutes.
889 Electron micrographs were taken on JEOL JEM1400 (120kV) equipped with an Orius 832
890 digital camera with 9 μm pixel (Gatan). To test the percentage of the ciliary vesicle positive
891 centriole, multiple serial sections (typically 3-4) were analyzed per each mother centriole, as
892 ciliary vesicles are often not attached to all nine blades of the distal appendage (i.e., ciliary
893 vesicles are often not found in all the sections of the same mother centriole).
894
895 **Immunofluorescence**
896 For wide-field microscopy, cells were grown on acid-washed 12 mm #1.5 round coverslips
897 (72230-10, Electron Microscopy Sciences) and fixed either in 4% paraformaldehyde (433689M,
898 Alfa Aesar) in phosphate buffered saline (PBS) for 15 min at room temperature or in 100%
899 methanol (A412-4, Fisher Scientific) for 5 min at -20°C. The primary antibodies used for
900 immunofluorescence are listed in the "Source Data 4-List of the antiboidies_CEP89-NCS1". All
901 staining condition such as fixation condition and dilution of the antibodies can be found in the
902 source data of each figure. After blocking with 5% normal serum that are matched with the
903 species used to raise secondary antibodies (005-000-121 or 017-000-121, Jackson
904 ImmunoResearch) in immunofluorescence (IF) buffer (3% bovine serum albumin (BP9703100,

905 Fisher Scientific), 0.02% sodium azide (BDH7465-2, VWR International), and 0.1% NP-40 in
906 PBS) for 30 min at room temperature, cells were incubated with primary antibody in IF buffer
907 for at least 3 hr at room temperature, followed by rinsing with IF buffer five times. The samples
908 were then incubated with fluorescent-labeled secondary antibody (listed below) in IF buffer for 1
909 hr at room temperature, followed by rinsing with IF buffer five times. After nuclear staining with
910 4',6-diamidino-2-phenylindole (DAPI) (40043, Biotium) in IF buffer at a final concentration of
911 0.5 μg/ml, coverslips were mounted with Fluoromount-G (0100-01, SouthernBiotech) onto glass
912 slides (3050002, Epredia). Images were acquired on an Everest deconvolution workstation
913 (Intelligent Imaging Innovations) equipped with a Zeiss Axio Imager Z1 microscope and a
914 CoolSnap HQ cooled CCD camera (Roper Scientific). A 40x NA1.3 Plan-Apochromat objective
915 lens (420762-9800, Zeiss) was used for ciliation assays, and a 63x NA1.4 Plan-Apochromat
916 objective lens (420780-9900, Zeiss) was used for other analyses.
917 For ciliation assays, cells were plated into a 6-well plate at a density of 2 x 10^5 cells/well and
918 grown for 66 hr. Cells were serum starved for 24 hr unless otherwise indicated and fixed in 4%
919 PFA. In the experiments presented in Figure 3A, the cells were incubated in serum free media for
920 12, 24, 48, 72, or 96 hours before fixation. After the blocking step, cells were stained with anti-
921 ARL13B (17711-1-AP, Proteintech), anti-CEP170 (41-3200, Invitrogen), and anti-acetylated
922 tubulin (Ac-Tub) antibodies (T7451, SIGMA), washed, then stained with anti-rabbit Alexa Fluor
923 488 (711-545-152, Jackson ImmunoResearch), goat anti-mouse IgG1-Alexa Fluor 568 (A-
924 21124, Invitrogen), and goat anti-mouse IgG2b Alexa Fluor 647 (A-21242, Invitrogen). All the
925 images were captured by focusing CEP170 without looking at a channel of the ciliary proteins to
926 avoid selecting specific area based on the percentage of ciliated cells. The structures extending
927 from the centrosome and positive for ARL13B with the length of more than 1 μm was counted as

928 primary cilia. At least 6 images from different fields per sample were captured for typical
929 analysis. Typically, at least 200 cells were analyzed per experiment. Exact number of cells that
930 we analyzed in each sample can be found in the Source Data of corresponding figures. The
931 percentage of ciliated cells were manually counted using the SlideBook software (Intelligent
932 Imaging Innovations).
933 For ciliary vesicle recruitment assays, cells were plated into a 6-well plate at a density of 2 x 10^5
934 cells/well, grown for 66 hr (without serum starvation), and fixed in 4% PFA. After the blocking
935 step, cells were stained with anti-RAB34 (27435-1-AP, Proteintech), anti-Myosin Va (sc-
936 365986, Santa Cruz), and anti-CEP170 (to mark centriole) antibodies (41-3200, Invitrogen),
937 washed, and then stained with goat anti-mouse IgG2a Alexa Fluor 488 (A-21131, Proteintech),
938 goat anti-rabbit Alexa Fluor 568 (A10042, Invitrogen), and goat anti-mouse IgG1 Alexa Fluor
939 647 (A-21240, Invitrogen). All the images were captured by focusing CEP170 without looking at
940 a channel of the ciliary vesicle markers to avoid selecting specific area based on the percentage
941 of ciliary vesicle positive centrioles. At least eight images from different fields per sample were
942 captured for typical analysis. Typically, at least 50 cells were analyzed per experiment. Exact
943 number of cells that we analyzed in each sample can be found in the Source Data of
944 corresponding figures.
945 For CP110 removal assays, cells were plated into a 6-well plate at a density of 2 x 10^5 cells/well
946 and grown for 66 hr. Cells were serum starved for 24 hr in 100% methanol. After the blocking
947 step, cells were stained with anti-CP110 (12780-1-AP, Proteintech), anti-FOP (H00011116-M01,
948 Abnova) (to mark both mother and daughter centrioles), and anti-CEP164 (sc-515403, Santa
949 Cruz) (to mark the mother centriole) antibodies, washed, then stained with anti-rabbit Alexa
950 Fluor 488 (711-545-152, Jackson ImmunoResearch), goat anti-mouse IgG2a-Alexa Fluor 568

951 (A-21134, Invitrogen), and goat anti-mouse IgG2b Alexa Fluor 647 (A-21242, Invitrogen). All
952 the images were captured by focusing FOP without looking at a channel of the other centriolar
953 proteins to avoid selecting specific area based on the percentage of CP110 positive centrioles.
954 CP110 localizing to both mother and daughter centrioles (as judged by colocalization with FOP)
955 were counted as two dots, and CP110 localizing only to daughter centriole (as judged by no
956 colocalization with CEP164) was counted as a one dot. Exact number of cells that we analyzed
957 in each sample can be found in the Source Data of corresponding figures.
958
959 For structured illumination microscopy, cells were grown on 18 mm square coverslips with the
960 thickness of 0.17 mm (474030-9000-000, Zeiss), fixed, and stained as described above. DAPI
961 staining was not included for the structured illumination samples. Coverslips were mounted with
962 SlowFade Gold Antifade Reagent (S36936, Life Technologies). Images were acquired on a
963 DeltaVision OMX V4 system equipped with a 100×/1.40 NA UPLANSAPO100XO objective
964 lens (Olympus), and 488 nm (100 mW), 561 nm (100 mW), and 642 nm (300 mW) Coherent
965 Sapphire solid state lasers and Evolve 512 EMCCD cameras (Photometrics). Image stacks of 2
966 μm z-steps were taken in 0.125 μm increments to ensure Nyquist sampling. Images were then
967 computationally reconstructed and subjected to image registration by using SoftWoRx 6.5.1
968 software.
969 Secondary antibodies used for immunofluorescence were donkey anti-rabbit Alexa Fluor 488
970 (711-545-152, Jackson ImmunoResearch), donkey anti-Chicken IgY Alexa Fluor 488 (703-545-
971 155, Jackson ImmunoResearch), donkey anti-mouse IgG DyLight 488 (715-485-150, Jackson
972 ImmunoResearch), goat anti-mouse IgG2a Alexa Fluor 488 (A-21131, Thermo Fisher
973 Scientific), goat anti-mouse IgG_1 Alexa Fluor 488 (A-21121, Thermo Fisher Scientific), donkey

974 anti-rabbit IgG Alexa Fluor 568 (A10042, Thermo Fisher Scientific), goat anti-mouse IgG2a-
975 Alexa Fluor 568 (A-21134, Thermo Fisher Scientific), goat anti-mouse IgG1-Alexa568 (A-
976 21124, Thermo Fisher Scientific), goat anti-mouse IgG2b Alexa Fluor 647 (A-21242, Thermo
977 Fisher Scientific), goat anti-mouse IgG1 Alexa Fluor 647 (A-21240, Thermo Fisher Scientific),
978 donkey anti-rabbit IgG Alexa Fluor 647 (711-605-152, Jackson ImmunoResearch).
979
980 **Mice**
981 *Ncs1*$^{-/-}$ mice in a C57BL/6J background were originally generated by the lab of Olaf Pongs
982 (Hermainski, 2012) and the strategy for the gene targeting was previously described (Ng et al.,
983 2016). Briefly, the 129 strain derived R1 embryonic stem cells carrying the targeting cassette
984 was injected into C57BL/6J blastocysts. The resulting *Ncs1*$^{-/-}$ mice, which lack exon 4-7 of *Ncs1*,
985 were backcrossed to C57BL/6J over 10 generations. The backcrossed mice were re-derived and
986 maintained at the Toronto Centre for Phenogenomics until they were transferred to Stanford
987 University.
988 All mice were maintained under specific pathogen-free conditions at the Stanford animal care
989 facility. All experiments were approved by Administrative Panel on Laboratory Animal Care at
990 Stanford University (Institutional Animal Care and Use Committee protocol number: 28556).
991 The primers used for genotyping PCR are mNCS1_genotyping-F: 5'-
992 GTCCACCCATACCAATCACT -3', mNCS1_genotyping_WT-R: 5'-
993 ACAGAGAATCCAAAGCCAGC-3', mNCS1_genotyping_KO-R: 5'-
994 TTGTGCTGGAGAAGGGAGAG-3'. The bands observed by PCR amplifications are 398 bp
995 and 514 bp for wild-type and knockout mice respectively.

996 The term “littermate controls” used in this paper means that the mice were born from the same
997 mother on the same day and were housed in the same cage as the test animals throughout the life.
998
999 Assessment of viability of *Ncs1*$^{-/-}$ mice
1000 To test viability of *Ncs1*$^{-/-}$ mice, *Ncs1*$^{+/-}$ female and male mice were mated, and genotype of the
1001 offspring was examined by genomic PCR using the genotyping PCR primers described above at
1002 P21.
1003
1004 Body weight measurement
1005 The body weight of male or female *Ncs1*$^{-/-}$ mice and their littermate controls were measured
1006 weekly between 9 am-12 pm. The statistics was obtained through 2-way ANOVA with Tukey’s
1007 multiple comparisons test. All the raw data can be available in Figure 8B-Source Data.
1008
1009 Measurement of fat weight
1010 20 week old *Ncs1*$^{-/-}$ and their litter mate *Ncs1*$^{+/-}$ mice were anesthetized with isoflurane and
1011 euthanized by cervical dissociation. Inguinal or epididymal fat was then dissected out from the
1012 mice and were measured on a scale.
1013
1014 Preparation, staining, and imaging of the tissue samples.
1015 6- to 8-week-old *Ncs1*$^{-/-}$ or their litter mate control animals were first anesthetized with 3%
1016 isoflurane (Fluriso, Bet-one) at a delivery rate of 1L/min. Complete anesthesia was confirmed by
1017 checking toe pinch reflex, and the animal was kept anesthetized throughout the procedure using a
1018 face mask that is connected to the anesthesia machine (VetEquip). Following exposure of the

1019 heart, an incision was made in the right atrium. Next, 27G½ gage needle (305109, BD)
1020 connected to a 20 ml syringe (302830, BD) was inserted into the left ventricle to transcardially
1021 perfuse the animal with 20 ml of PBS followed by 1.5 ml/g (-35 ml) of 4% (v/v)
1022 paraformaldehyde (PFA) (15710, Electron Microscopy Sciences). Note that the transcardial
1023 perfusion of 4% PFA is critical to preserve the sample to visualize primary cilia in tissues. The
1024 fixed tissues were dissected out and post-fixed in 20 ml of 100% methanol at -20°C for 20 hours.
1025 We found that the post fixation in methanol is critical for Ncs1 visualization in tissues likely
1026 through washing out the PFA from the tissue, since over-fixation of the samples in PFA greatly
1027 diminished the centrosomal signal of Ncs1 in monolayer cultured cells (data not shown). The
1028 post-fixed tissues were then submerged in graded concentration (10-20-30% (w/v)) of sucrose
1029 (S9378, SIGMA Aldrich) in PBS at 4°C until the tissue sunk in each solution to cryoprotect the
1030 samples. The tissues were then embedded into OCT compound (4583, Tissue-Tek). Cryosections
1031 (typically 7-10 μm thickness) were created on a Cryostat (3050S, Leica) and the sliced tissues
1032 were collected on adhesive microscope slides (16005-110, VWR). Samples were immunostained
1033 using the same procedure as the one used for wide-field microscopy experiments. The stained
1034 samples were imaged on the Marianas SDC spinning disk microscope (Intelligent Imaging
1035 Innovations) equipped with Cascade 1K camera (photometrics) and CSU22 confocal scanner
1036 unit (Yokogawa). A 63x NA1.4 Plan-Apochromat objective lens (420781-9910-000, Zeiss) was
1037 used to acquire images. Typically, image stacks of 10 -20 μm z-steps were taken in 0.5 μm
1038 increments.
1039
1040 <u>HE stains</u>

1041 20, 30, or 50 weeks old *Ncs1*$^{-/-}$ mice and their littermate controls were first fixed by transcardial
1042 perfusion of 4% PFA as described above and post-fixed in 4% PFA at 4°C for 72 hours. Tissues
1043 were then processed, embedded in paraffin blocks, sectioned on a microtome, and stained with
1044 Hematoxylin and eosin by standard techniques. Optimal number of tile pictures were obtained
1045 and stitched together via Keyence BZ-X710 fluorescent microscope.
1046
1047 Isolation of hippocampal neurons
1048 Hippocampus was dissected out from E18.5 mice, which were developed from *Ncs1*$^{+/-}$ female
1049 mouse crossed with *Ncs1*$^{+/-}$ male mice. The dissected hippocampus was dissociated by incubating
1050 the tissue in calcium magnesium free (CMF)-HBSS media (14175095, Gibco) supplemented
1051 with 10 mM HEPES (15630080, Gibco) containing 0.05% trypsin (15400-054, Gibco) at 37°C
1052 for 20 minutes. After washing the trypsinized tissue three times with 500 μl of CMF-HBSS
1053 containing 10 mM HEPES, the tissue was triturated with a fire polished Pasteur pipette. The
1054 dissociated cells were then plated on a 12 mm round coverslip (12-545-81, Fisher Scientific)
1055 coated with poly-D-lysine at a density of 60,000 cells per 24-well plate (930186, Thermo
1056 Scientific). The cells were grown in 500 μl of the Neurobasal Medium (21103049, Gibco)
1057 supplemented with 1×B27 (17504044, Gibco), 1×GlutaMax, 100 U/mL Penicillin-Streptomycin,
1058 and 10% horse serum (16050130, Gibco). 24 hours after plating, the media were replaced with
1059 the Neurobasal Medium media supplemented with 1×B27, 1×GlutaMax, and 100 U/mL
1060 Penicillin-Streptomycin. The genotype of the neurons was confirmed by genotyping PCR using
1061 the genotyping PCR primers described above.
1062
1063 Preparation of Mouse Embryonic Fibroblast

1064 Mouse embryonic fibroblasts (MEFs) were prepared from E13.5 mice embryos, which were
1065 developed from *Ncs1*$^{+/-}$ female mice crossed with *Ncs1*$^{+/-}$ male mice. After removing innards
1066 from the embryo, the remaining was minced with a razor blade (55411-050, VWR). The minced
1067 tissues were dissociated using 2 ml 0.05% trypsin/EDTA (25300-054, Gibco) for 20 minutes at
1068 37°C, followed by neutralization of trypsin by adding 4 ml of MEF media (DMEM high glucose
1069 (11995073, Gibco), 10% FBS (100-106, Gemini), 1×GlutaMax (35050-079, Thermo Fisher
1070 Scientific), and 100 U/mL Penicillin-Streptomycin (15140163, Thermo Fisher Scientific))
1071 containing 100 μg DNase I (LS002006, Worthington). Cells were then pelleted down, re-
1072 suspended in 15 ml of MEF media and plated into a T75 flask. The genotype of the MEFs were
1073 confirmed by genotyping PCR using the genotyping PCR primers described above. All
1074 experiments were performed with the cells that were passaged no more than three times.
1075
1076 Immunoblotting of the tissue lysate
1077 A 7-week-old *Ncs1*$^{-/-}$ and a 6-week-old *Ncs1*$^{+/+}$ mouse (not a littermate control) were anesthetized
1078 with isoflurane and euthanized by cervical dissociation. Tissues were quickly dissected out and
1079 minced with a razor blade (55411-050, VWR). The minced tissue is lysed in tissue lysis buffer
1080 (50 mM Tris-HCl [pH7.5], 150 mM NaCl, and 1% NP-40 (11332473001, Roche Applied
1081 Science)) for 15 minutes. Following clarification of the lysate at centrifugation at 15,000 rpm
1082 (21,000 g) for 15 minutes at 4°C, the concentration of the supernatant was measured by Bradford
1083 assay as previously described (see Procedure B step 8 in (T. Kanie & Jackson, 2018)). The lysate
1084 was mixed to prepare a sample containing 4 mg/ml lysate, 1×LDS buffer, and 2.5% 2-
1085 mercaptoethanol. 50 μg (for NCS1 blot) or 12 μg (for other proteins) were loaded onto

1086 NuPAGE™ Novex™ 4-12% Bis-Tris protein gels. Western blot was performed as described
1087 above and the fluorescent signal was detected on an Odyssey CLx Imaging System (LI-COR).
1088

1089 **Experimental replicates**

1090 The term "replicates" used in this paper indicate that the same cell lines were plated at different
1091 dates for each experiment. In most cases, cell lines were thawed from liquid nitrogen at different
1092 dates and immunostaining was performed at different dates among the replicates.
1093

1094 **Quantification of fluorescent intensity and statistical analysis**

1095 *Fluorescent intensity measurement*

1096 The fluorescent intensity was measured with 16-bit TIFF muti-color stack images acquired at
1097 63x magnification (NA1.4) by using Image J software. To measure the fluorescent intensity of
1098 centrosomal proteins, channels containing CEP170 and the protein of interest (POI) were
1099 individually extracted into separate images. A rolling ball background subtraction with a rolling
1100 ball radius of 5 pixels was implemented for both CEP170 and the POI to perform local
1101 background subtraction. The mask for both CEP170 and the POI was created by setting the lower
1102 threshold to the minimum level that covers only centrosome. Each mask was then combined by
1103 converting the two masks to a stack followed by z projection and then dilating the mask until the
1104 two masks are merged. After eroding the dilated masks several times, the fluorescent intensity of
1105 the POI was measured via "analyze particles" command with optimal size and circularity. The
1106 size and circularity are optimized for individual POI to detect most of the centrosome in the
1107 image without capturing non-centrosomal structure. Outliers (likely non-centrosomal structure)
1108 were then excluded from the data using the ROUT method with a false discovery rate of 1%

1109 using GraphPad Prism 9 software. Fluorescent intensity of ciliary proteins was measured
1110 similarly to centrosomal proteins but with several modifications. Mask was created for ciliary
1111 proteins by setting the lower threshold to the minimum level that covers only cilia. The size and
1112 circularity are optimized for individual POI to detect only cilia without capturing non-ciliary
1113 structure. Macros used for the intensity measurement are available from "Source Data- Macro for
1114 measuring fluorescent intensity of centrosomal proteins" and "Source Data-Macro for measuring
1115 fluorescent intensity of ciliary proteins" in an accompanying paper (Tomoharu Kanie et al.,
1116 2023).
1117 To test whether the difference in the signal intensity is statistically different between control and
1118 test samples, the intensity measured through the described method was compared between
1119 control and test samples using nested one-way ANOVA with Dunnett's multiple comparisons
1120 test or nested t-test if there are more than two replicates. In case there are less than three
1121 replicates, the statistical test was not performed in a single experiment, as the signal intensity is
1122 affected slightly by staining procedure and statistical significance is affected largely by the
1123 number of cells examined. For example, we saw statistical significance in the signal intensity
1124 with the same samples that are stained independently if we analyze large number of the cells
1125 (more than 100 cells). Instead, we confirmed the same tendency in the change of fluorescent
1126 intensity in the test samples across two replicates.
1127
1128 *Statistical analysis for ciliation, ciliary vesicle recruitment, and CP110 removal assay*
1129 For ciliation, ciliary vesicle recruitment, and CP110 removal assay, the number of ciliated cells
1130 from the indicated number of replicates were compared between control (sgGFP or sgSafe) and

1131 the test samples using Welch's t test. The exact number of samples and replicated are indicated
1132 in the Source Data of the corresponding figures.
1133
1134 For all the statistics used in this paper, asterisks denote *: $0.01 \leq p < 0.05$, **: $p < 0.01$, ***: $p <$
1135 0.001, n.s.: not significant. All the statical significance was calculated by using GraphPad Prism
1136 9 software.
1137
1138 **Materials Availability Statement**
1139 All the newly created materials used in this paper including plasmids and stable cell lines are
1140 readily available from the corresponding authors (Tomoharu-Kanie@ouhsc.edu or
1141 pjackson@stanford.edu) upon request.
1142
1143 **Figure supplements**
1144 Figure 1-figure supplement 1. *Co-immunoprecipitation of endogenous NCS1 and the localization*
1145 *of CEP89 mutants shown in Figure 1C.*
1146 Figure 1-figure supplement 2. *A negative control for the experiment shown in Figure 1E and F.*
1147 Figure 2-figure supplement 1. *Localization of GFP tagged NCS1.*
1148 Figure 2-figure supplement 2. *Quantification data and immunoblot related to Figure 2.*
1149 Figure 2-figure supplement 3. *Localization of other distal appendage proteins in NCS1*
1150 *knockouts.*
1151 Figure 3-figure supplement 1. *Quantification of ciliary signal intensity of ARL13B in CEP89 and*
1152 *NCS1 knockouts.*
1153 Figure 5-figure supplement 1. *Calcium is required mainly for the stability of NCS1.*

1154 Figure 7-figure supplement 1. *The expression of NCS1 in various tissues*.

1155 Figure 7-figure supplement 2. *NCS1 localizes to the ciliary base in most ciliated tissues but not*

1156 *in photoreceptor cells*.

1157 Figure 7-figure supplement 3. *Localization of ciliary GPCRs is mildly decreased in hippocampal*

1158 *neurons prepared from Ncs1$^{-/-}$ mice*.

1159

1160 **Source Data**

1161 Figure 1A- Source Data. Uncropped image of silver staining of the tandem affinity purification

1162 analysis of CEP89.

1163 Figure 1B-Source Data. Mass spectrometry analysis of tandem affinity purification of CEP89.

1164 Figure 1D-Source Data. The original files of the full raw unedited blots shown in Figure 1D.

1165 Figure 1E-Source Data. The original files of the full raw unedited blots shown in Figure 1D.

1166 Figure 1F-Source Data. The original files of the full raw unedited blots shown in Figure 1E.

1167 Figure 2A-Source Data. Immunofluorescence conditions in the experiment shown in Figure 2A.

1168 Figure 2B-Source Data. Immunofluorescence conditions in the experiment shown in Figure 2B.

1169 Figure 2C-Source Data. Immunofluorescence conditions, raw image quantification data, and

1170 detailed statistics of the experiment shown in Figure 2C.

1171 Figure 2D-I-Source Data. Immunofluorescence conditions in the experiment shown in Figure

1172 2D-I.

1173 Figure 2K-Source Data. Immunofluorescence conditions in the experiment shown in Figure 2K.

1174 Figure 2L-Source Data. Immunofluorescence conditions in the experiment shown in Figure 2L.

1175 Figure 2M-Source Data. Immunofluorescence conditions in the experiment shown in Figure 2M.

1176 Figure 3A-Source Data. Raw quantification data, immunofluorescence conditions and detailed
1177 statistics of the experiment shown in Figure 3A.
1178 Figure 3B-Source Data. Raw quantification data, immunofluorescence conditions and detailed
1179 statistics of the experiment shown in Figure 3B.
1180 Figure 3C-Source Data. Raw quantification data, immunofluorescence conditions and detailed
1181 statistics of the experiment shown in Figure 3C.
1182 Figure 3E-Source Data. Raw quantification data and detailed statistics of the experiment shown
1183 in Figure 3E.
1184 Figure 3F-Source Data. Raw quantification data, immunofluorescence conditions and detailed
1185 statistics of the experiment shown in Figure 3F.
1186 Figure 3F-Source Data. Raw quantification data, immunofluorescence conditions and detailed
1187 statistics of the experiment shown in Figure 3F.
1188 Figure 3G-Source Data. Raw quantification data, immunofluorescence conditions and detailed
1189 statistics of the experiment shown in Figure 3G.
1190 Figure 3H-Source Data. Raw quantification data, immunofluorescence conditions and detailed
1191 statistics of the experiment shown in Figure 3H.
1192 Figure 4A-Source Data. The original files of the full raw unedited blots shown in Figure 4A.
1193 Figure 4B-Source Data. Raw quantification data, immunofluorescence conditions and detailed
1194 statistics of the experiment shown in Figure 4B.
1195 Figure 4C-Source Data. Raw quantification data, immunofluorescence conditions and detailed
1196 statistics of the experiment shown in Figure 4C.
1197 Figure 4D-Source Data. Raw quantification data, immunofluorescence conditions and detailed
1198 statistics of the experiment shown in Figure 4D.

1199 Figure 5A-Source Data. The original files of the full raw unedited blots shown in Figure 5A.

1200 Figure 5B-Source Data. The original files of the full raw unedited blots shown in Figure 5B.

1201 Figure 5C-Source Data. Immunofluorescence conditions in the experiment shown in Figure 5C.

1202 Figure 5D-Source Data. Raw quantification data and immunofluorescence conditions of the

1203 experiment shown in Figure 5D.

1204 Figure 5E-Source Data. Raw quantification data, immunofluorescence conditions and detailed

1205 statistics of the experiment shown in Figure 5E.

1206 Figure 5F-Source Data. Raw quantification data, immunofluorescence conditions and detailed

1207 statistics of the experiment shown in Figure 5F.

1208 Figure 6B-Source Data. Immunofluorescence conditions in the experiment shown in Figure 6B.

1209 Figure 6C-Source Data. Raw quantification data, immunofluorescence conditions and detailed

1210 statistics of the experiment shown in Figure 6C.

1211 Figure 6D-Source Data. Raw quantification data, immunofluorescence conditions and detailed

1212 statistics of the experiment shown in Figure 6D.

1213 Figure 6E-Source Data. Raw quantification data and immunofluorescence conditions of the

1214 experiment shown in Figure 6E.

1215 Figure 6F-Source Data. Raw quantification data and immunofluorescence conditions of the

1216 experiment shown in Figure 6F.

1217 Figure 7A-Source Data. Immunofluorescence conditions in the experiment shown in Figure 7A.

1218 Figure 7B-Source Data. Immunofluorescence conditions in the experiment shown in Figure 7B.

1219 Figure 7C-Source Data. Immunofluorescence conditions in the experiment shown in Figure 7C.

1220 Figure 7D-Source Data. Immunofluorescence conditions in the experiment shown in Figure 7D.

1221 Figure 7E-Source Data. Raw quantification data, immunofluorescence conditions and detailed
1222 statistics of the experiment shown in Figure 7E.
1223 Figure 7F-Source Data. Raw quantification data, immunofluorescence conditions and detailed
1224 statistics of the experiment shown in Figure 7F.
1225 Figure 7G-Source Data. Raw quantification data, immunofluorescence conditions and detailed
1226 statistics of the experiment shown in Figure 7G.
1227 Figure 7H-Source Data. Raw quantification data, immunofluorescence conditions and detailed
1228 statistics of the experiment shown in Figure 7H.
1229 Figure 8A-Source Data. Detailed information of the mice and detailed statistics of the
1230 experiment shown in Figure 8A.
1231 Figure 8B-C-Source Data. Raw data and detailed statistics of the experiment shown in Figure
1232 8B-C.
1233 Figure 8D-Source Data. Raw data and detailed statistics of the experiment shown in Figure 8D.
1234 Figure 8E-G-H-Source Data. Information of the mice used in the experiments shown in Figure
1235 8E, G and H.
1236 Figure 8F-Source Data. Raw data and detailed statistics of the experiment shown in Figure 8F.
1237
1238 Figure 1-figure supplement 1A-Source Data. The original files of the full raw unedited blots
1239 shown in Figure 1-figure supplement 1A.
1240 Figure 1-Figure Supplement 1B-Source Data. Immunofluorescence conditions in the experiment
1241 shown in Figure 1-Figure supplement 1B.
1242 Figure 1-figure supplement 2A-Source Data. The original files of the full raw unedited blots
1243 shown in Figure 1-figure supplement 2A.

1244 Figure 2-Figure Supplement 1-Source Data. Immunofluorescence conditions in the experiment
1245 shown in Figure 2-Figure supplement 1.
1246 Figure 2-Figure Supplement 2A-Source Data. Immunofluorescence conditions and raw
1247 quantification data of the experiment shown in Figure 2-Figure supplement 2A.
1248 Figure 2-Figure Supplement 2B-Source Data. Immunofluorescence conditions and raw
1249 quantification data of the experiment shown in Figure 2-Figure supplement 2B.
1250 Figure 2-Figure Supplement 2C-Source Data. Immunofluorescence conditions and raw
1251 quantification data of the experiment shown in Figure 2-Figure supplement 2C.
1252 Figure 2-figure supplement 2D-Source Data. The original files of the full raw unedited blots
1253 shown in Figure 2-figure supplement 2D.
1254 Figure 2-figure supplement 2E-Source Data. The original files of the full raw unedited blots
1255 shown in Figure 2-figure supplement 2E.
1256 Figure 2-Figure Supplement 3A-Source Data. Immunofluorescence conditions, raw
1257 quantification data and detailed statistics of the experiment shown in Figure 2-Figure supplement
1258 3A.
1259 Figure 2-Figure Supplement 3B-Source Data. Immunofluorescence conditions, raw
1260 quantification data and detailed statistics of the experiment shown in Figure 2-Figure supplement
1261 3B.
1262 Figure 2-Figure Supplement 3C-Source Data. Immunofluorescence conditions and raw
1263 quantification data of the experiment shown in Figure 2-Figure supplement 3C.
1264 Figure 2-Figure Supplement 3D-Source Data. Immunofluorescence conditions and raw
1265 quantification data of the experiment shown in Figure 2-Figure supplement 3D.

1266 Figure 3-Figure Supplement 1-Source Data. Immunofluorescence conditions, raw quantification
1267 data and detailed statistics of the experiment shown in Figure 3-Figure supplement 1A-C.
1268 Figure 5-figure supplement 1A-Source Data. The original files of the full raw unedited blots
1269 shown in Figure 5-figure supplement 1A.
1270 Figure 5-Figure Supplement 1B-Source Data. Immunofluorescence conditions and raw
1271 quantification data of the experiment shown in Figure 5-Figure supplement 1B.
1272 Figure 5-Figure Supplement 1C-Source Data. Immunofluorescence conditions, raw
1273 quantification data and detailed statistics of the experiment shown in Figure 5-Figure supplement
1274 1C.
1275 Figure 7-figure supplement 1A-Source Data. The original files of the full raw unedited blots
1276 shown in Figure 7-figure supplement 1A.
1277 Figure 7-Figure Supplement 2-Source Data. Immunofluorescence conditions in the experiment
1278 shown in Figure 7-Figure supplement 2A-E.
1279 Figure 7-Figure Supplement 3A-Source Data. Immunofluorescence conditions, raw
1280 quantification data and detailed statistics of the experiment shown in Figure 7-Figure supplement
1281 3A.
1282 Figure 7-Figure Supplement 3B-Source Data. Immunofluorescence conditions, raw
1283 quantification data and detailed statistics of the experiment shown in Figure 7-Figure supplement
1284 3B.
1285 Source Data 1-Primers used for genomic PCR and for generating sgRNA vectors.
1286 Source Data 2- The list of mouse embryonic fibroblasts used in this paper.
1287 Source Data 3- The list of Hippocampal Neurons used in this paper.
1288 Source Data 4- The list of antibodies used in this paper.

1289 Source Data 5- The list of cell lines used in this paper.

1290 Source Data 6- uncropped images of the Immunoblot with label.

1291 Source Data 7-summary of CRISPR knockout cells.

1292

1293 **References**

1294 Acs, P., Bauer, P. O., Mayer, B., Bera, T., Macallister, R., Mezey, E., & Pastan, I. (2015). A

1295 novel form of ciliopathy underlies hyperphagia and obesity in Ankrd26 knockout mice. Brain

1296 Struct Funct, 220(3), 1511-1528. doi:10.1007/s00429-014-0741-9

1297 Ames, J. B., Hendricks, K. B., Strahl, T., Huttner, I. G., Hamasaki, N., & Thorner, J. (2000).

1298 Structure and calcium-binding properties of Frq1, a novel calcium sensor in the yeast

1299 Saccharomyces cerevisiae. Biochemistry, 39(40), 12149-12161. doi:10.1021/bi0012890

1300 Ames, J. B., Ishima, R., Tanaka, T., Gordon, J. I., Stryer, L., & Ikura, M. (1997). Molecular

1301 mechanics of calcium-myristoyl switches. Nature, 389(6647), 198-202. doi:10.1038/38310

1302 Anderson, R. G. (1972). The three-dimensional structure of the basal body from the rhesus

1303 monkey oviduct. J Cell Biol, 54(2), 246-265. doi:10.1083/jcb.54.2.246

1304 Aravind, P., Chandra, K., Reddy, P. P., Jeromin, A., Chary, K. V., & Sharma, Y. (2008).

1305 Regulatory and structural EF-hand motifs of neuronal calcium sensor-1: Mg 2+ modulates Ca 2+

1306 binding, Ca 2+ -induced conformational changes, and equilibrium unfolding transitions. J Mol

1307 Biol, 376(4), 1100-1115. doi:10.1016/j.jmb.2007.12.033

1308 Baksheeva, V. E., Nemashkalova, E. L., Firsov, A. M., Zalevsky, A. O., Vladimirov, V. I.,

1309 Tikhomirova, N. K., . . . Zernii, E. Y. (2020). Membrane Binding of Neuronal Calcium Sensor-1:

1310 Highly Specific Interaction with Phosphatidylinositol-3-Phosphate. Biomolecules, 10(2).

1311 doi:10.3390/biom10020164

Barnes, B. G. (1961). Ciliated secretory cells in the pars distalis of the mouse hypophysis. J Ultrastruct Res, 5, 453-467. doi:10.1016/s0022-5320(61)80019-1

Bera, T. K., Liu, X. F., Yamada, M., Gavrilova, O., Mezey, E., Tessarollo, L., . . . Pastan, I. (2008). A model for obesity and gigantism due to disruption of the Ankrd26 gene. Proc Natl Acad Sci U S A, 105(1), 270-275. doi:10.1073/pnas.0710978105

Berbari, N. F., Bishop, G. A., Askwith, C. C., Lewis, J. S., & Mykytyn, K. (2007). Hippocampal neurons possess primary cilia in culture. J Neurosci Res, 85(5), 1095-1100. doi:10.1002/jnr.21209

Berbari, N. F., Malarkey, E. B., Yazdi, S. M., McNair, A. D., Kippe, J. M., Croyle, M. J., . . . Yoder, B. K. (2014). Hippocampal and cortical primary cilia are required for aversive memory in mice. PLoS One, 9(9), e106576. doi:10.1371/journal.pone.0106576

Bernatik, O., Pejskova, P., Vyslouzil, D., Hanakova, K., Zdrahal, Z., & Cajanek, L. (2020). Phosphorylation of multiple proteins involved in ciliogenesis by Tau Tubulin kinase 2. Mol Biol Cell, 31(10), 1032-1046. doi:10.1091/mbc.E19-06-0334

Bishop, G. A., Berbari, N. F., Lewis, J., & Mykytyn, K. (2007). Type III adenylyl cyclase localizes to primary cilia throughout the adult mouse brain. J Comp Neurol, 505(5), 562-571. doi:10.1002/cne.21510

Bornens, M. (2012). The centrosome in cells and organisms. Science, 335(6067), 422-426. doi:10.1126/science.1209037

Bourne, Y., Dannenberg, J., Pollmann, V., Marchot, P., & Pongs, O. (2001). Immunocytochemical localization and crystal structure of human frequenin (neuronal calcium sensor 1). J Biol Chem, 276(15), 11949-11955. doi:10.1074/jbc.M009373200

Bowler, M., Kong, D., Sun, S., Nanjundappa, R., Evans, L., Farmer, V., . . . Loncarek, J. (2019). High-resolution characterization of centriole distal appendage morphology and dynamics by correlative STORM and electron microscopy. Nat Commun, 10(1), 993. doi:10.1038/s41467-018-08216-4

Brechbuhl, J., Klaey, M., & Broillet, M. C. (2008). Grueneberg ganglion cells mediate alarm pheromone detection in mice. Science, 321(5892), 1092-1095. doi:10.1126/science.1160770

Breunig, J. J., Sarkisian, M. R., Arellano, J. I., Morozov, Y. M., Ayoub, A. E., Sojitra, S., . . . Town, T. (2008). Primary cilia regulate hippocampal neurogenesis by mediating sonic hedgehog signaling. Proc Natl Acad Sci U S A, 105(35), 13127-13132. doi:10.1073/pnas.0804558105

Brinkman, E. K., Chen, T., Amendola, M., & van Steensel, B. (2014). Easy quantitative assessment of genome editing by sequence trace decomposition. Nucleic Acids Res, 42(22), e168. doi:10.1093/nar/gku936

Burgoyne, R. D., & Weiss, J. L. (2001). The neuronal calcium sensor family of Ca2+-binding proteins. Biochem J, 353(Pt 1), 1-12. Retrieved from https://www.ncbi.nlm.nih.gov/pubmed/11115393

Cajanek, L., & Nigg, E. A. (2014). Cep164 triggers ciliogenesis by recruiting Tau tubulin kinase 2 to the mother centriole. Proc Natl Acad Sci U S A, 111(28), E2841-2850. doi:10.1073/pnas.1401777111

Cheeseman, I. M., & Desai, A. (2005). A combined approach for the localization and tandem affinity purification of protein complexes from metazoans. Sci STKE, 2005(266), pl1. doi:10.1126/stke.2662005pl1

Chong, W. M., Wang, W. J., Lo, C. H., Chiu, T. Y., Chang, T. J., Liu, Y. P., . . . Liao, J. C. (2020). Super-resolution microscopy reveals coupling between mammalian centriole subdistal appendages and distal appendages. Elife, 9. doi:10.7554/eLife.53580

Craft, J. M., Harris, J. A., Hyman, S., Kner, P., & Lechtreck, K. F. (2015). Tubulin transport by IFT is upregulated during ciliary growth by a cilium-autonomous mechanism. J Cell Biol, 208(2), 223-237. doi:10.1083/jcb.201409036

Dason, J. S., Romero-Pozuelo, J., Atwood, H. L., & Ferrus, A. (2012). Multiple roles for frequenin/NCS-1 in synaptic function and development. Mol Neurobiol, 45(2), 388-402. doi:10.1007/s12035-012-8250-4

Dateyama, I., Sugihara, Y., Chiba, S., Ota, R., Nakagawa, R., Kobayashi, T., & Itoh, H. (2019). RABL2 positively controls localization of GPCRs in mammalian primary cilia. J Cell Sci, 132(2). doi:10.1242/jcs.224428

de Rezende, V. B., Rosa, D. V., Comim, C. M., Magno, L. A., Rodrigues, A. L., Vidigal, P., . . . Romano-Silva, M. A. (2014). NCS-1 deficiency causes anxiety and depressive-like behavior with impaired non-aversive memory in mice. Physiol Behav, 130, 91-98. doi:10.1016/j.physbeh.2014.03.005

Delgehyr, N., Sillibourne, J., & Bornens, M. (2005). Microtubule nucleation and anchoring at the centrosome are independent processes linked by ninein function. J Cell Sci, 118(Pt 8), 1565-1575. doi:10.1242/jcs.02302

Delling, M., DeCaen, P. G., Doerner, J. F., Febvay, S., & Clapham, D. E. (2013). Primary cilia are specialized calcium signalling organelles. Nature, 504(7479), 311-314. doi:10.1038/nature12833

Dickinson, M. E., Flenniken, A. M., Ji, X., Teboul, L., Wong, M. D., White, J. K., . . . Murray, S. A. (2016). High-throughput discovery of novel developmental phenotypes. Nature, 537(7621), 508-514. doi:10.1038/nature19356

Ding, X., Fragoza, R., Singh, P., Zhang, S., Yu, H., & Schimenti, J. C. (2020). Variants in RABL2A causing male infertility and ciliopathy. Hum Mol Genet, 29(20), 3402-3411. doi:10.1093/hmg/ddaa230

Dingemans, K. P. (1969). The relation between cilia and mitoses in the mouse adenohypophysis. J Cell Biol, 43(2), 361-367. doi:10.1083/jcb.43.2.361

Einstein, E. B., Patterson, C. A., Hon, B. J., Regan, K. A., Reddi, J., Melnikoff, D. E., . . . Tallent, M. K. (2010). Somatostatin signaling in neuronal cilia is critical for object recognition memory. J Neurosci, 30(12), 4306-4314. doi:10.1523/JNEUROSCI.5295-09.2010

Elias, J. E., & Gygi, S. P. (2007). Target-decoy search strategy for increased confidence in large-scale protein identifications by mass spectrometry. Nat Methods, 4(3), 207-214. doi:10.1038/nmeth1019

Fath, M. A., Mullins, R. F., Searby, C., Nishimura, D. Y., Wei, J., Rahmouni, K., . . . Sheffield, V. C. (2005). Mkks-null mice have a phenotype resembling Bardet-Biedl syndrome. Hum Mol Genet, 14(9), 1109-1118. doi:10.1093/hmg/ddi123

Forsyth, R. L., & Gunay-Aygun, M. (2020). Bardet-Biedl Syndrome Overview. 2003 Jul 14 [Updated 2020 Jul 23]. In E. D. Adam MP, Mirzaa GM, et al (Ed.), GeneReviews® [Internet]. Seattle (WA).

Forsythe, E., & Beales, P. L. (2013). Bardet-Biedl syndrome. Eur J Hum Genet, 21(1), 8-13. doi:10.1038/ejhg.2012.115

Ganga, A. K., Kennedy, M. C., Oguchi, M. E., Gray, S., Oliver, K. E., Knight, T. A., . . . Breslow, D. K. (2021). Rab34 GTPase mediates ciliary membrane formation in the intracellular ciliogenesis pathway. Curr Biol, 31(13), 2895-2905 e2897. doi:10.1016/j.cub.2021.04.075

Gierke, P., Zhao, C., Brackmann, M., Linke, B., Heinemann, U., & Braunewell, K. H. (2004). Expression analysis of members of the neuronal calcium sensor protein family: combining bioinformatics and Western blot analysis. Biochem Biophys Res Commun, 323(1), 38-43. doi:10.1016/j.bbrc.2004.08.055

Gomez, M., De Castro, E., Guarin, E., Sasakura, H., Kuhara, A., Mori, I., . . . Nef, P. (2001). Ca2+ signaling via the neuronal calcium sensor-1 regulates associative learning and memory in C. elegans. Neuron, 30(1), 241-248. doi:10.1016/s0896-6273(01)00276-8

Graham, J. M. (2015). Fractionation of Subcellular Organelles. Curr Protoc Cell Biol, 69, 3 1 1-3 1 22. doi:10.1002/0471143030.cb0301s69

Graser, S., Stierhof, Y. D., Lavoie, S. B., Gassner, O. S., Lamla, S., Le Clech, M., & Nigg, E. A. (2007). Cep164, a novel centriole appendage protein required for primary cilium formation. J Cell Biol, 179(2), 321-330. doi:10.1083/jcb.200707181

Gupta, G. D., Coyaud, E., Goncalves, J., Mojarad, B. A., Liu, Y., Wu, Q., . . . Pelletier, L. (2015). A Dynamic Protein Interaction Landscape of the Human Centrosome-Cilium Interface. Cell, 163(6), 1484-1499. doi:10.1016/j.cell.2015.10.065

Han, Y. G., Spassky, N., Romaguera-Ros, M., Garcia-Verdugo, J. M., Aguilar, A., Schneider-Maunoury, S., & Alvarez-Buylla, A. (2008). Hedgehog signaling and primary cilia are required for the formation of adult neural stem cells. Nat Neurosci, 11(3), 277-284. doi:10.1038/nn2059

Hermainski, J. G. (2012). Untersuchungen zur Funktion des Neuronalen Calcium Sensors 1 (NCS-1) an genetisch veränderten Mauslinien (Mus musculus, Linnaeus 1758). (Dissertation).

Hibbard, J. V. K., Vazquez, N., Satija, R., & Wallingford, J. B. (2021). Protein turnover dynamics suggest a diffusion-to-capture mechanism for peri-basal body recruitment and retention of intraflagellar transport proteins. Mol Biol Cell, 32(12), 1171-1180. doi:10.1091/mbc.E20-11-0717

Huttlin, E. L., Bruckner, R. J., Navarrete-Perea, J., Cannon, J. R., Baltier, K., Gebreab, F., . . . Gygi, S. P. (2021). Dual proteome-scale networks reveal cell-specific remodeling of the human interactome. Cell, 184(11), 3022-3040 e3028. doi:10.1016/j.cell.2021.04.011

Kanie, T., Abbott, K. L., Mooney, N. A., Plowey, E. D., Demeter, J., & Jackson, P. K. (2017). The CEP19-RABL2 GTPase Complex Binds IFT-B to Initiate Intraflagellar Transport at the Ciliary Base. Dev Cell, 42(1), 22-36 e12. doi:10.1016/j.devcel.2017.05.016

Kanie, T., & Jackson, P. K. (2018). Guanine Nucleotide Exchange Assay Using Fluorescent MANT-GDP. Bio Protoc, 8(7). doi:10.21769/BioProtoc.2795

Kanie, T., Love, J. F., Fisher, S. D., Gustavsson, A.-K., & Jackson, P. K. (2023). A hierarchical pathway for assembly of the distal appendages that organize primary cilia. bioRxiv, 2023.2001.2006.522944. doi:10.1101/2023.01.06.522944

Kurtulmus, B., Yuan, C., Schuy, J., Neuner, A., Hata, S., Kalamakis, G., . . . Pereira, G. (2018). LRRC45 contributes to early steps of axoneme extension. J Cell Sci, 131(18). doi:10.1242/jcs.223594

Lemire, S., Jeromin, A., & Boisselier, E. (2016). Membrane binding of Neuronal Calcium Sensor-1 (NCS1). Colloids Surf B Biointerfaces, 139, 138-147. doi:10.1016/j.colsurfb.2015.11.065

Lim, S., Strahl, T., Thorner, J., & Ames, J. B. (2011). Structure of a Ca2+-myristoyl switch protein that controls activation of a phosphatidylinositol 4-kinase in fission yeast. J Biol Chem, 286(14), 12565-12577. doi:10.1074/jbc.M110.208868

Lo, C. H., Lin, I. H., Yang, T. T., Huang, Y. C., Tanos, B. E., Chou, P. C., . . . Wang, W. J. (2019). Phosphorylation of CEP83 by TTBK2 is necessary for cilia initiation. J Cell Biol, 218(10), 3489-3505. doi:10.1083/jcb.201811142

Loktev, A. V., & Jackson, P. K. (2013). Neuropeptide Y family receptors traffic via the Bardet-Biedl syndrome pathway to signal in neuronal primary cilia. Cell Rep, 5(5), 1316-1329. doi:10.1016/j.celrep.2013.11.011

Loktev, A. V., Zhang, Q., Beck, J. S., Searby, C. C., Scheetz, T. E., Bazan, J. F., . . . Nachury, M. V. (2008). A BBSome subunit links ciliogenesis, microtubule stability, and acetylation. Dev Cell, 15(6), 854-865. doi:10.1016/j.devcel.2008.11.001

Lu, Q., Insinna, C., Ott, C., Stauffer, J., Pintado, P. A., Rahajeng, J., . . . Westlake, C. J. (2015). Early steps in primary cilium assembly require EHD1/EHD3-dependent ciliary vesicle formation. Nat Cell Biol, 17(3), 228-240. doi:10.1038/ncb3109

Mazo, G., Soplop, N., Wang, W. J., Uryu, K., & Tsou, M. F. (2016). Spatial Control of Primary Ciliogenesis by Subdistal Appendages Alters Sensation-Associated Properties of Cilia. Dev Cell, 39(4), 424-437. doi:10.1016/j.devcel.2016.10.006

Mirzadeh, Z., Merkle, F. T., Soriano-Navarro, M., Garcia-Verdugo, J. M., & Alvarez-Buylla, A. (2008). Neural stem cells confer unique pinwheel architecture to the ventricular surface in neurogenic regions of the adult brain. Cell Stem Cell, 3(3), 265-278. doi:10.1016/j.stem.2008.07.004

Molla-Herman, A., Ghossoub, R., Blisnick, T., Meunier, A., Serres, C., Silbermann, F., . . . Benmerah, A. (2010). The ciliary pocket: an endocytic membrane domain at the base of primary and motile cilia. J Cell Sci, 123(Pt 10), 1785-1795. doi:10.1242/jcs.059519

Mun, H. S., Saab, B. J., Ng, E., McGirr, A., Lipina, T. V., Gondo, Y., . . . Roder, J. C. (2015). Self-directed exploration provides a Ncs1-dependent learning bonus. Sci Rep, 5, 17697. doi:10.1038/srep17697

Mykytyn, K., Mullins, R. F., Andrews, M., Chiang, A. P., Swiderski, R. E., Yang, B., . . . Sheffield, V. C. (2004). Bardet-Biedl syndrome type 4 (BBS4)-null mice implicate Bbs4 in flagella formation but not global cilia assembly. Proc Natl Acad Sci U S A, 101(23), 8664-8669. doi:10.1073/pnas.0402354101

Nakamura, T. Y., Jeromin, A., Mikoshiba, K., & Wakabayashi, S. (2011). Neuronal calcium sensor-1 promotes immature heart function and hypertrophy by enhancing Ca2+ signals. Circ Res, 109(5), 512-523. doi:10.1161/CIRCRESAHA.111.248864

Nakamura, T. Y., Nakao, S., Nakajo, Y., Takahashi, J. C., Wakabayashi, S., & Yanamoto, H. (2017). Possible Signaling Pathways Mediating Neuronal Calcium Sensor-1-Dependent Spatial Learning and Memory in Mice. PLoS One, 12(1), e0170829. doi:10.1371/journal.pone.0170829

Ng, E., Georgiou, J., Avila, A., Trought, K., Mun, H. S., Hodgson, M., . . . Wong, A. H. C. (2020). Mice lacking neuronal calcium sensor-1 show social and cognitive deficits. Behav Brain Res, 381, 112420. doi:10.1016/j.bbr.2019.112420

Ng, E., Varaschin, R. K., Su, P., Browne, C. J., Hermainski, J., Le Foll, B., . . . Wong, A. H. (2016). Neuronal calcium sensor-1 deletion in the mouse decreases motivation and dopamine release in the nucleus accumbens. Behav Brain Res, 301, 213-225. doi:10.1016/j.bbr.2015.12.037

Nguyen, L. D., Nolte, L. G., Tan, W. J. T., Giuvelis, D., Santos-Sacchi, J., Bilsky, E., & Ehrlich, B. E. (2021). Comprehensive somatosensory and neurological phenotyping of NCS1 knockout mice. Sci Rep, 11(1), 2372. doi:10.1038/s41598-021-81650-5

Nishimura, D. Y., Fath, M., Mullins, R. F., Searby, C., Andrews, M., Davis, R., . . . Sheffield, V. C. (2004). Bbs2-null mice have neurosensory deficits, a defect in social dominance, and retinopathy associated with mislocalization of rhodopsin. Proc Natl Acad Sci U S A, 101(47), 16588-16593. doi:10.1073/pnas.0405496101

O'Callaghan, D. W., Ivings, L., Weiss, J. L., Ashby, M. C., Tepikin, A. V., & Burgoyne, R. D. (2002). Differential use of myristoyl groups on neuronal calcium sensor proteins as a determinant of spatio-temporal aspects of Ca2+ signal transduction. J Biol Chem, 277(16), 14227-14237. doi:10.1074/jbc.M111750200

O'Callaghan, D. W., Tepikin, A. V., & Burgoyne, R. D. (2003). Dynamics and calcium sensitivity of the Ca2+/myristoyl switch protein hippocalcin in living cells. J Cell Biol, 163(4), 715-721. doi:10.1083/jcb.200306042

Oguchi, M. E., Okuyama, K., Homma, Y., & Fukuda, M. (2020). A comprehensive analysis of Rab GTPases reveals a role for Rab34 in serum starvation-induced primary ciliogenesis. J Biol Chem, 295(36), 12674-12685. doi:10.1074/jbc.RA119.012233

Olafsson, P., Soares, H. D., Herzog, K. H., Wang, T., Morgan, J. I., & Lu, B. (1997). The Ca2+ binding protein, frequenin is a nervous system-specific protein in mouse preferentially localized in neurites. Brain Res Mol Brain Res, 44(1), 73-82. doi:10.1016/s0169-328x(96)00188-x

Paintrand, M., Moudjou, M., Delacroix, H., & Bornens, M. (1992). Centrosome organization and centriole architecture: their sensitivity to divalent cations. J Struct Biol, 108(2), 107-128. doi:10.1016/1047-8477(92)90011-x

Peitzsch, R. M., & McLaughlin, S. (1993). Binding of acylated peptides and fatty acids to phospholipid vesicles: pertinence to myristoylated proteins. Biochemistry, 32(39), 10436-10443. doi:10.1021/bi00090a020

Pongs, O., Lindemeier, J., Zhu, X. R., Theil, T., Engelkamp, D., Krah-Jentgens, I., . . . et al. (1993). Frequenin--a novel calcium-binding protein that modulates synaptic efficacy in the Drosophila nervous system. Neuron, 11(1), 15-28. doi:10.1016/0896-6273(93)90267-u

Ratai, O., Hermainski, J., Ravichandran, K., & Pongs, O. (2019). NCS-1 Deficiency Is Associated With Obesity and Diabetes Type 2 in Mice. Front Mol Neurosci, 12, 78. doi:10.3389/fnmol.2019.00078

Reiter, J. F., & Leroux, M. R. (2017). Genes and molecular pathways underpinning ciliopathies. Nat Rev Mol Cell Biol, 18(9), 533-547. doi:10.1038/nrm.2017.60

Rhee, S., Kirschen, G. W., Gu, Y., & Ge, S. (2016). Depletion of primary cilia from mature dentate granule cells impairs hippocampus-dependent contextual memory. Sci Rep, 6, 34370. doi:10.1038/srep34370

Rigaut, G., Shevchenko, A., Rutz, B., Wilm, M., Mann, M., & Seraphin, B. (1999). A generic protein purification method for protein complex characterization and proteome exploration. Nat Biotechnol, 17(10), 1030-1032. doi:10.1038/13732

Saab, B. J., Georgiou, J., Nath, A., Lee, F. J., Wang, M., Michalon, A., . . . Roder, J. C. (2009). NCS-1 in the dentate gyrus promotes exploration, synaptic plasticity, and rapid acquisition of spatial memory. Neuron, 63(5), 643-656. doi:10.1016/j.neuron.2009.08.014

Sang, L., Miller, J. J., Corbit, K. C., Giles, R. H., Brauer, M. J., Otto, E. A., . . . Jackson, P. K. (2011). Mapping the NPHP-JBTS-MKS protein network reveals ciliopathy disease genes and pathways. Cell, 145(4), 513-528. doi:10.1016/j.cell.2011.04.019

Schmidt, K. N., Kuhns, S., Neuner, A., Hub, B., Zentgraf, H., & Pereira, G. (2012). Cep164 mediates vesicular docking to the mother centriole during early steps of ciliogenesis. J Cell Biol, 199(7), 1083-1101. doi:10.1083/jcb.201202126

Shalata, A., Ramirez, M. C., Desnick, R. J., Priedigkeit, N., Buettner, C., Lindtner, C., . . . Martignetti, J. A. (2013). Morbid obesity resulting from inactivation of the ciliary protein CEP19 in humans and mice. Am J Hum Genet, 93(6), 1061-1071. doi:10.1016/j.ajhg.2013.10.025

Shevchenko, A., Tomas, H., Havlis, J., Olsen, J. V., & Mann, M. (2006). In-gel digestion for mass spectrometric characterization of proteins and proteomes. Nat Protoc, 1(6), 2856-2860. doi:10.1038/nprot.2006.468

Sillibourne, J. E., Hurbain, I., Grand-Perret, T., Goud, B., Tran, P., & Bornens, M. (2013). Primary ciliogenesis requires the distal appendage component Cep123. Biol Open, 2(6), 535-545. doi:10.1242/bio.20134457

Sillibourne, J. E., Specht, C. G., Izeddin, I., Hurbain, I., Tran, P., Triller, A., . . . Bornens, M. (2011). Assessing the localization of centrosomal proteins by PALM/STORM nanoscopy. Cytoskeleton (Hoboken), 68(11), 619-627. doi:10.1002/cm.20536

Simon, M. M., Greenaway, S., White, J. K., Fuchs, H., Gailus-Durner, V., Wells, S., . . . Brown, S. D. (2013). A comparative phenotypic and genomic analysis of C57BL/6J and C57BL/6N mouse strains. Genome Biol, 14(7), R82. doi:10.1186/gb-2013-14-7-r82

Sorokin, S. (1962). Centrioles and the formation of rudimentary cilia by fibroblasts and smooth muscle cells. J Cell Biol, 15, 363-377. doi:10.1083/jcb.15.2.363

Sorokin, S. P. (1968). Reconstructions of centriole formation and ciliogenesis in mammalian lungs. J Cell Sci, 3(2), 207-230. doi:10.1242/jcs.3.2.207

1556 Spektor, A., Tsang, W. Y., Khoo, D., & Dynlacht, B. D. (2007). Cep97 and CP110 suppress a
1557 cilia assembly program. Cell, 130(4), 678-690. doi:10.1016/j.cell.2007.06.027
1558 Stuck, M. W., Chong, W. M., Liao, J. C., & Pazour, G. J. (2021). Rab34 is necessary for early
1559 stages of intracellular ciliogenesis. Curr Biol, 31(13), 2887-2894 e2884.
1560 doi:10.1016/j.cub.2021.04.018
1561 Tanos, B. E., Yang, H. J., Soni, R., Wang, W. J., Macaluso, F. P., Asara, J. M., & Tsou, M. F.
1562 (2013). Centriole distal appendages promote membrane docking, leading to cilia initiation.
1563 Genes Dev, 27(2), 163-168. doi:10.1101/gad.207043.112
1564 Torres, J. Z., Miller, J. J., & Jackson, P. K. (2009). High-throughput generation of tagged stable
1565 cell lines for proteomic analysis. Proteomics, 9(10), 2888-2891. doi:10.1002/pmic.200800873
1566 Vorobjev, I. A., & Chentsov Yu, S. (1982). Centrioles in the cell cycle. I. Epithelial cells. J Cell
1567 Biol, 93(3), 938-949. doi:10.1083/jcb.93.3.938
1568 Wang, Z., Phan, T., & Storm, D. R. (2011). The type 3 adenylyl cyclase is required for novel
1569 object learning and extinction of contextual memory: role of cAMP signaling in primary cilia. J
1570 Neurosci, 31(15), 5557-5561. doi:10.1523/JNEUROSCI.6561-10.2011
1571 Wright, K. J., Baye, L. M., Olivier-Mason, A., Mukhopadhyay, S., Sang, L., Kwong, M., . . .
1572 Jackson, P. K. (2011). An ARL3-UNC119-RP2 GTPase cycle targets myristoylated NPHP3 to
1573 the primary cilium. Genes Dev, 25(22), 2347-2360. doi:10.1101/gad.173443.111
1574 Wright, M. H., Heal, W. P., Mann, D. J., & Tate, E. W. (2010). Protein myristoylation in health
1575 and disease. J Chem Biol, 3(1), 19-35. doi:10.1007/s12154-009-0032-8
1576 Wu, C. T., Chen, H. Y., & Tang, T. K. (2018). Myosin-Va is required for preciliary vesicle
1577 transportation to the mother centriole during ciliogenesis. Nat Cell Biol, 20(2), 175-185.
1578 doi:10.1038/s41556-017-0018-7

Wu, Y., & Shroff, H. (2018). Faster, sharper, and deeper: structured illumination microscopy for biological imaging. Nat Methods, 15(12), 1011-1019. doi:10.1038/s41592-018-0211-z

Zhang, Y., Hao, J., Tarrago, M. G., Warner, G. M., Giorgadze, N., Wei, Q., . . . Hu, J. (2021). FBF1 deficiency promotes beiging and healthy expansion of white adipose tissue. Cell Rep, 36(5), 109481. doi:10.1016/j.celrep.2021.109481

Main Figures

1585

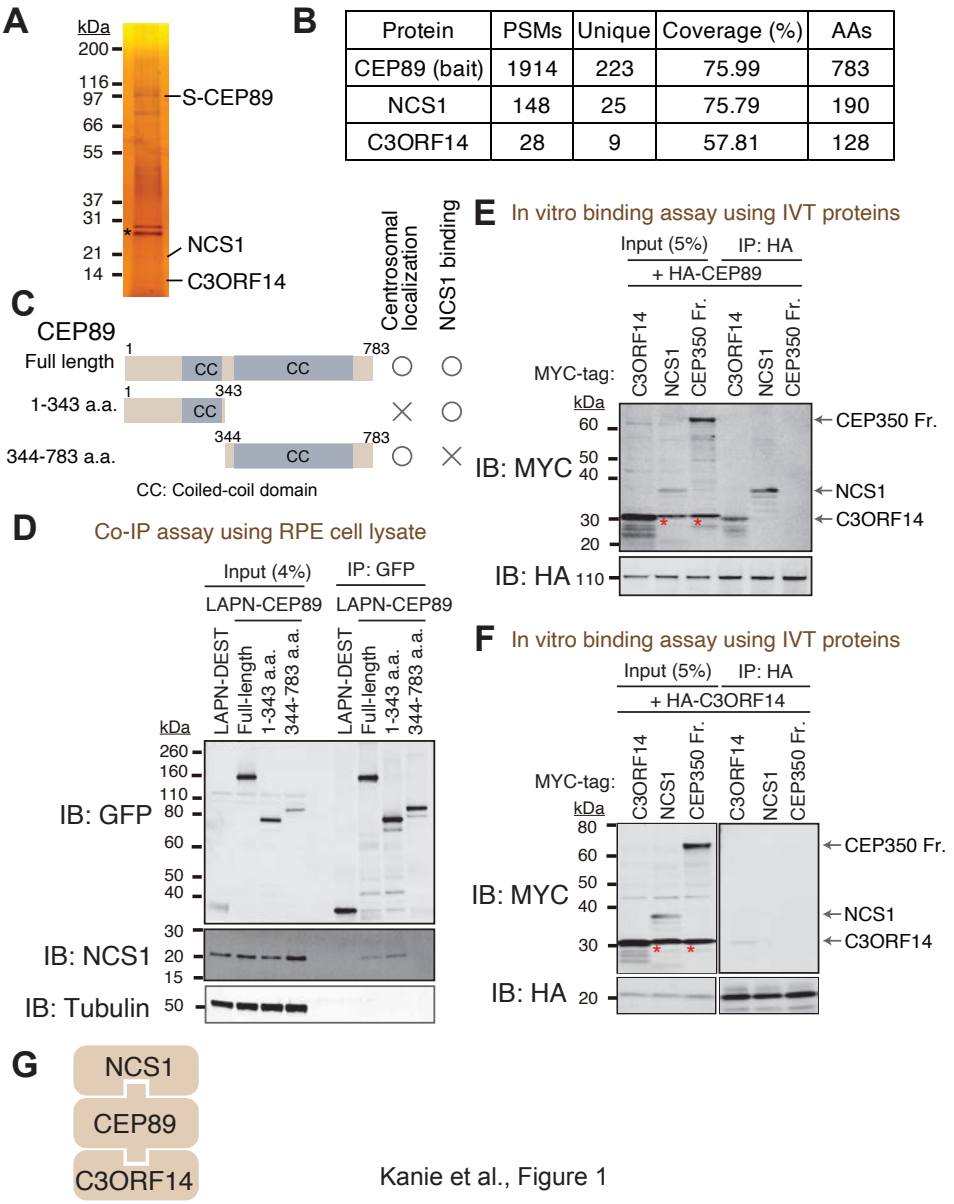

Protein	PSMs	Unique	Coverage (%)	AAs
CEP89 (bait)	1914	223	75.99	783
NCS1	148	25	75.79	190
C3ORF14	28	9	57.81	128

Kanie et al., Figure 1

Figure 1 ***Identification of Neuronal Calcium Sensor-1 as a stoichiometric interactor of CEP89.***

A. Silver staining of the eluate following tandem affinity purification of N-terminally LAP (EGFP-TEV cleavage site-S tag-PreScission cleavage site)-tagged CEP89 expressed in confluent RPE cells. The cell lysates were purified with GFP antibodies and S-protein beads, resolved by Sodium Dodecyl Sulfate–Polyacrylamide Gel Electrophoresis (SDS-PAGE) and visualized by silver staining. The bands corresponding to S tagged CEP89 (S-CEP89), NCS1, and C3ORF14 are indicated. Molecular weights (kDa) estimated from a protein marker are indicated. Asterisk denotes a band corresponding to TEV protease used for tandem affinity purification.

B. Tabulation of peptide-spectrum matches (PSMs), unique peptide counts, coverage, and the length of the amino acids from the mass spectrometry analysis of the eluate shown in (A).

C. A cartoon depicting the region of CEP89 important for centrosomal localization or binding to NCS1. Localization data can be found in Figure 1-figure supplement 1A.

D. Immunoblot (IB) analysis of the eluates from a co-immunoprecipitation assay of the full length or the indicated fragments of N-terminally LAP-tagged CEP89 expressed in confluent RPE cells. The cell lysates were purified with GFP antibodies, resolved by SDS-PAGE and immunoblotted with the indicated antibodies. Molecular weights (kDa) estimated from a protein marker are indicated.

E-F. Immunoblot (IB) analysis of the eluates from *in vitro* binding assay of the *in vitro* translated (IVT) N-terminally HA-tagged CEP89 (E) or C3ORF14 (F) and the indicated N-terminally MYC tagged proteins. The *in vitro* translated proteins were mixed and captured by HA-agarose beads, resolved by SDS-PAGE and immunoblotted with the indicated antibodies. The CEP350 fragment (2470-2836 a.a.), which binds to FOP efficiently (Figure 1-figure supplement 2A)(Kanie et al. 2017) serves as a negative control. Red asterisks indicate non-specific bands, which overlap with the MYC-tagged C3ORF14. Molecular weights (kDa) estimated from a protein marker are indicated.

G. The order of binding for CEP89-NCS1-C3ORF14 interaction.

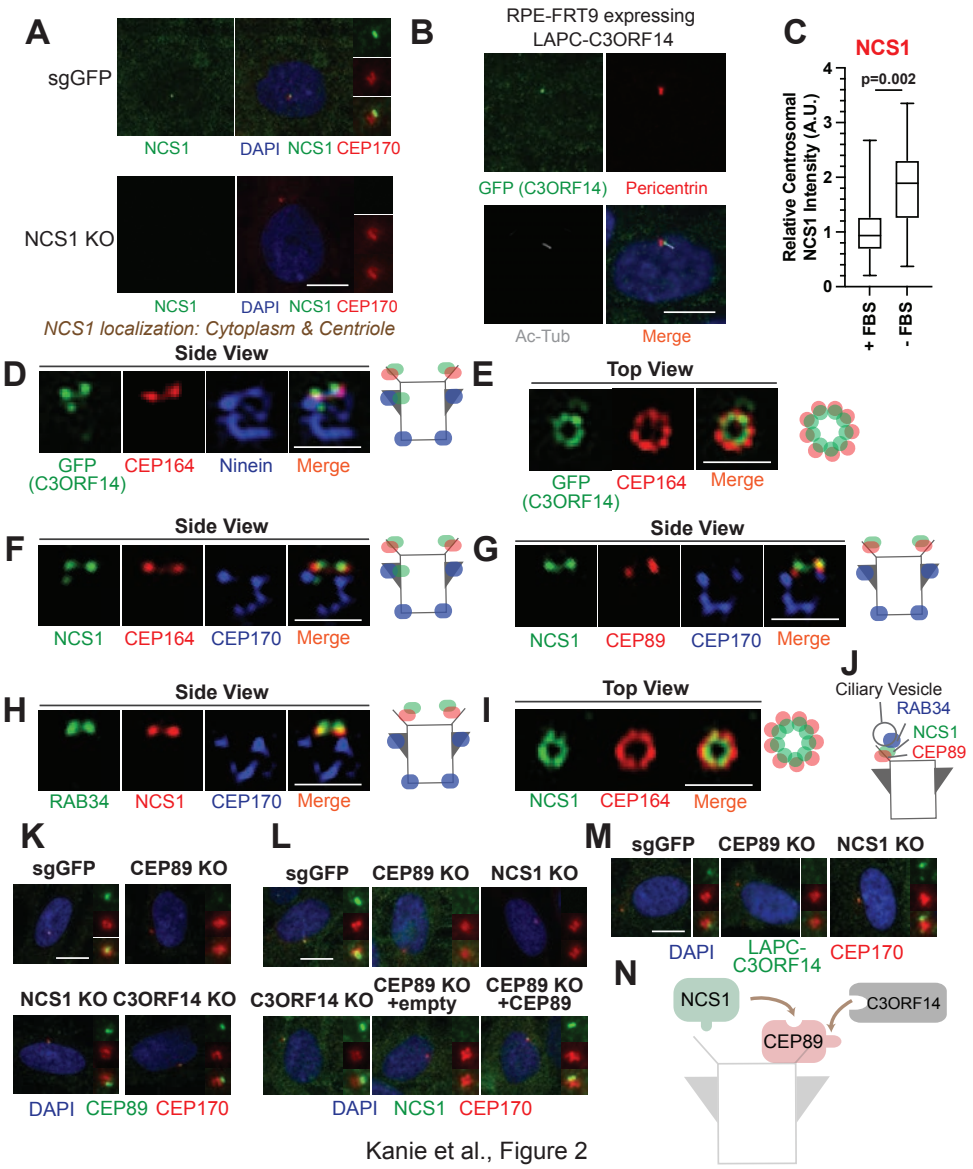

Figure 2 ***NCS1 is recruited to the distal appendage by CEP89.***

A. Immunofluorescence images taken via wide-field microscopy. Control (sgGFP) or NCS1 knockout RPE cells were serum starved for 24 hours, fixed, and stained with indicated antibodies. Insets at the right panels are the enlarged images of the mother centriole. Ac-Tub indicates acetylated α-tubulin. Scale bar: 10 μm.

B. Immunofluorescence images taken via wide-field microscopy. RPE cells expressing C-terminally LAP (LAPC) tagged C3ORF14 were serum starved for 24 hours, fixed, and stained with indicated antibodies. Scale bar: 10 μm.

C. Box plots showing centrosomal signal intensity of NCS1. RPE cells were grown in fetal bovine serum (FBS)-containing media for 24 hours, and then grown in either fetal bovine serum (FBS)-containing media (+ FBS) or serum free media (-FBS) for an additional 24 hours. Cells were fixed and stained with NCS1 antibody. Centrosomal signal intensity of NCS1 was measured from fluorescence images using the method described in Materials and Methods. A.U., arbitrary units. Data are combined from three replicates. Statistical significance was calculated from a nested T-test. The raw data, experimental conditions, and detailed statistics are available in Figure 2C-Source data

D-I. Immunofluorescence images taken via 3D-structured illumination microscopy. Side view (D, F, G, and H) or Top view (E and I) is shown. RPE cells were either grown to confluent (H) or serum starved for 24 hours (D-G and I), fixed and stained with indicated antibodies. Each individual image is from a representative z-slice. Scale bar: 1 μm. CEP170: a marker of subdistal appendage and proximal end of the mother centriole. A cartoon at the right of each figure shows estimated positions of each protein at the mother centriole.

J. A cartoon depicting the localization of NCS1 relative to RAB34 and CEP89. NCS1 is sandwiched between RAB34 and CEP89.

K-M. Immunofluorescence images taken via wide-filed microscopy. Control (sgGFP) or indicated knockout RPE cells were serum starved for 24 hours, fixed, and stained with indicated antibodies. Scale bar: 10 μm. Insets at the right panels are the enlarged images of the mother centriole. Quantification data are available in Figure 2-figure supplement 2A-C.

N. A cartoon depicting the order of recruitment of the CEP89-NCS1-C3ORF14 complex.

1587

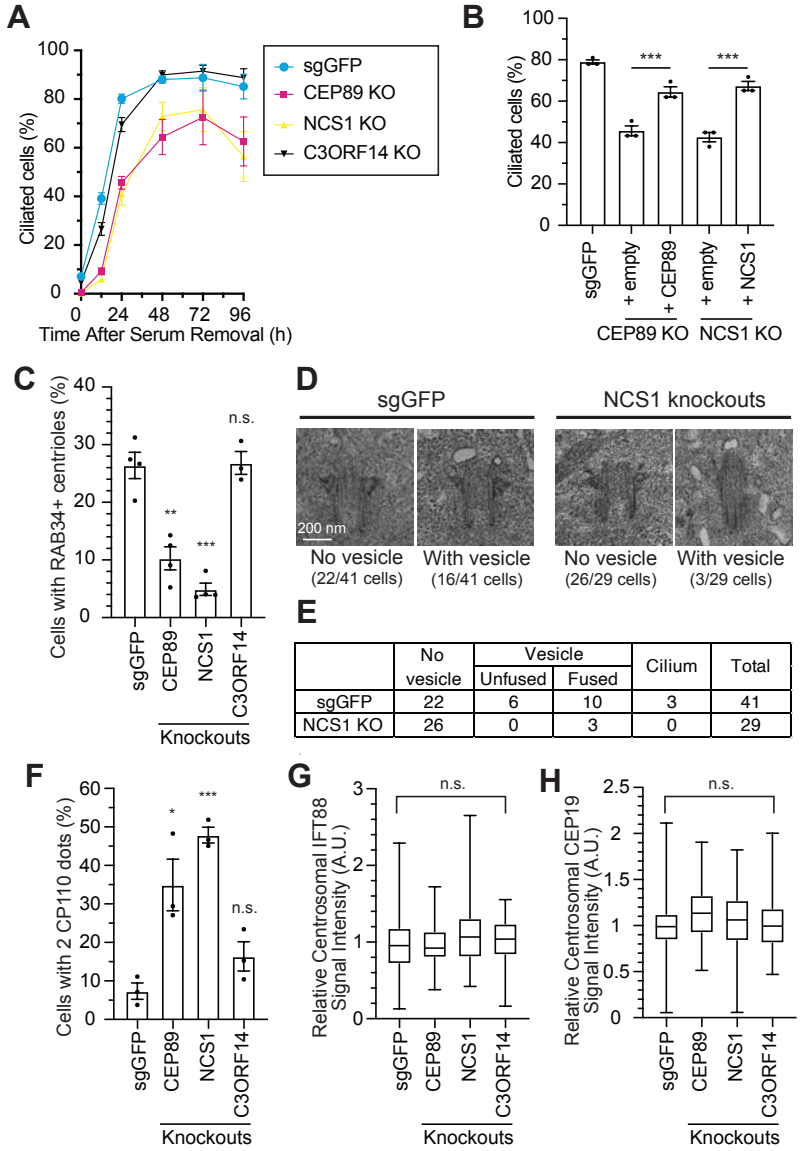

	No vesicle	Vesicle		Cilium	Total
		Unfused	Fused		
sgGFP	22	6	10	3	41
NCS1 KO	26	0	3	0	29

Kanie et al., Figure 3

Figure 3 ***NCS1 is important for ciliary vesicle recruitment, but not for IFT88/CEP19 recruitment.***

A. Time course of cilium formation assay in control (sgGFP) and indicated knockout RPE cells. The indicated cells were serum starved for 12, 24,48,72,96 hours, fixed, stained with α-ARL13B (to mark cilium) and α-CEP170 (to mark centriole), and imaged via wide-field microscopy. Data averaged from four independent experiments. Error bars represent ± SEM. Statistics obtained through comparing between each knockout and control by Welch's t-test. The raw data, experimental conditions, detailed statistics are available in Figure 3A-Source data.

B. Cilium formation assay in control (sgGFP) and indicated knockout RPE cells serum starved for 24 hours. Data averaged from three independent experiments, and each black dot indicates the value from the individual experiment. Error bars represent ± SEM. Statistics obtained by Welch's t-test. The raw data, experimental conditions, and detailed statistics are available in Figure 3B-Source data.

C. Ciliary vesicle recruitment assay in control (sgGFP) or indicated knockout RPE cells grown to confluence (without serum starvation). The data are averaged from 4 independent experiments, and each black dot indicates the value from each individual experiment. Error bars represent ± SEM. Statistics obtained through comparing between each knockout and control by Welch's t-test. The raw data, experimental conditions, and detailed statistics are available in Figure 3C-Source data.

D. Transmission electron microscopy analysis of the mother centriole in control (sgGFP) or NCS1 knockout RPE cells serum starved for 3 hours. The representative images of the mother centrioles without (left) or with (right) ciliary vesicle at the distal appendage are shown. Scale: 200 nm.

E. Quantification of the data from the experiments shown in Figure 3D. The raw data and detailed statistics are available in Figure 3E-Source data. This experiment was synchronized with the experiment shown in the Figure 4C of (Tomoharu Kanie et al., 2023), hence the values for sgGFP are exactly the same as the ones shown in (Tomoharu Kanie et al., 2023).

F. CP110 removal assay in control (sgGFP) and indicated knockout RPE cells serum starved for 24 hours. Data are averaged from three independent experiments, and each black dot indicates the value from the individual experiment. Error bars represent ± SEM. Statistics obtained through comparing between each knockout and control by Welch's t-test. The raw data, experimental conditions, and detailed statistics are available in Figure 3F-Source data.

G-H. Quantification of the centrosomal signal intensity of IFT88 (G) or CEP19 (H) in control (sgGFP) and indicated knockout RPE cells serum starved for 24 hours. The data are combined from three independent experiments. Statistical significance was calculated from nested T test. The raw data, experimental conditions, detailed statistics are available in Figure 3G-H-Source Data.

A.U., arbitrary units; n.s., not significant; *$p < 0.05$, **$p < 0.01$, ***$p < 0.001$

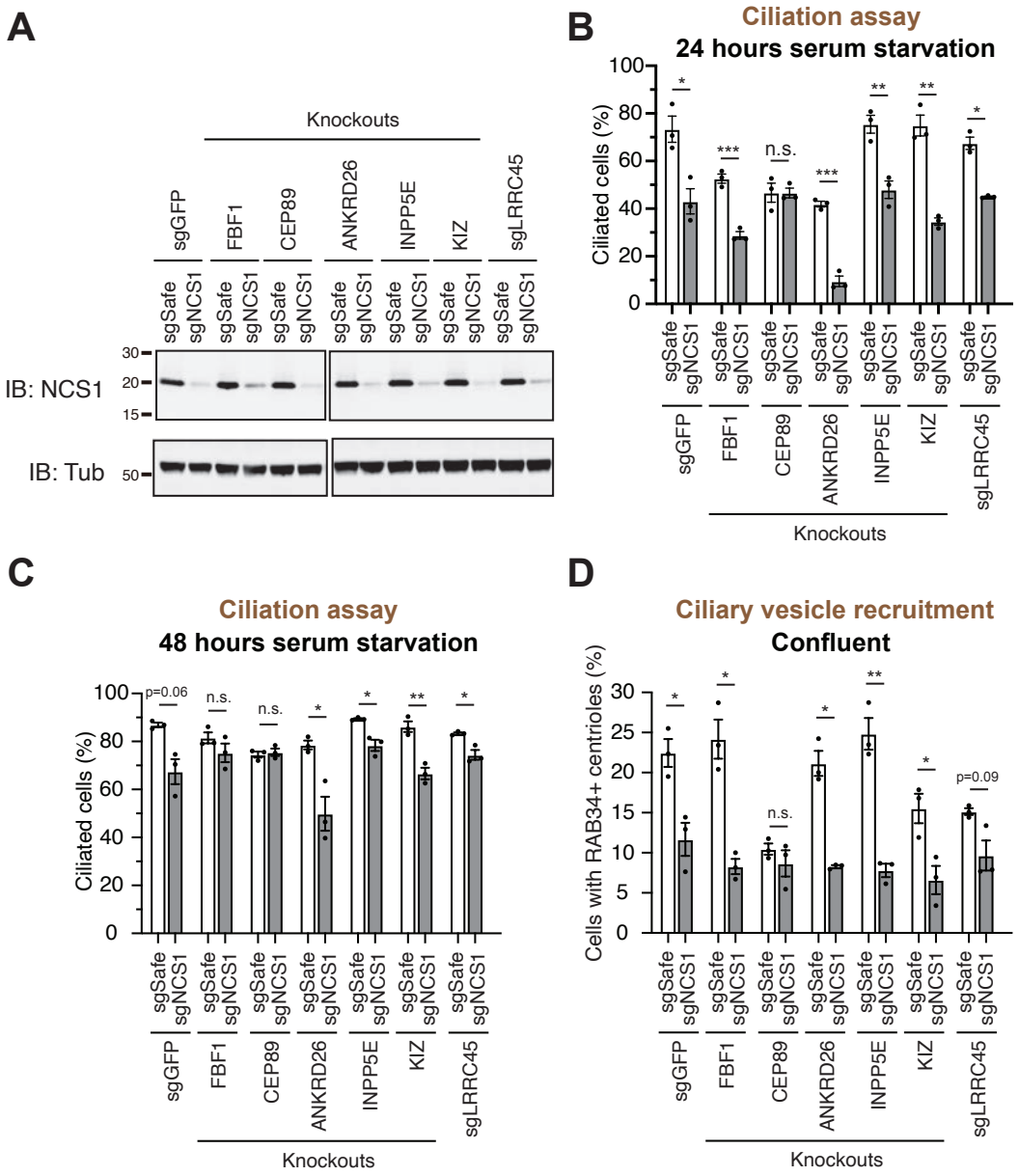

Kanie et al., Figure 4

Figure 4 A ***ciliary vesicle recruitment defect in NCS1 knockout cells is compensated by yet unknown distal appendage proteins.***

A. Immunoblot (IB) analysis of expression of NCS1 (IB: NCS1) and α-tubulin (IB: Tub) in control (sgGFP) or indicated knockout RPE cells stably expressing either sgSafe (non-targeting) or sgNCS1. The cells were grown to confluence (without serum starvation), lysed and analyzed by immunoblot. Molecular weights (kDa) estimated from a protein marker are indicated.

B-C. Cilium formation assay in control (sgGFP) and indicated knockout RPE cells stably expressing either sgSafe (non-targeting) or sgNCS1. The cells were serum starved for 24 (B) or 48 (C) hours. Data averaged from three independent experiments, and each black dot indicates the value from the individual experiment. Error bars represent ± SEM. Statistics obtained by Welch's t-test. The raw data, experimental conditions, and detailed statistics are available in Figure 4B-C-Source Data.

D. Ciliary vesicle recruitment assay in control (sgGFP) or indicated knockout RPE cells stably expressing either sgSafe (control) or sgNCS1. Cells were grown to confluence (without serum starvation). Data are averaged from three independent experiments. Error bars represent ± SEM. Statistics obtained by Welch's t-test. The raw data, experimental conditions, and detailed statistics are available in Figure 4D-Source data.

n.s., not significant; *p < 0.05, **p < 0.01, ***p < 0.001

1588

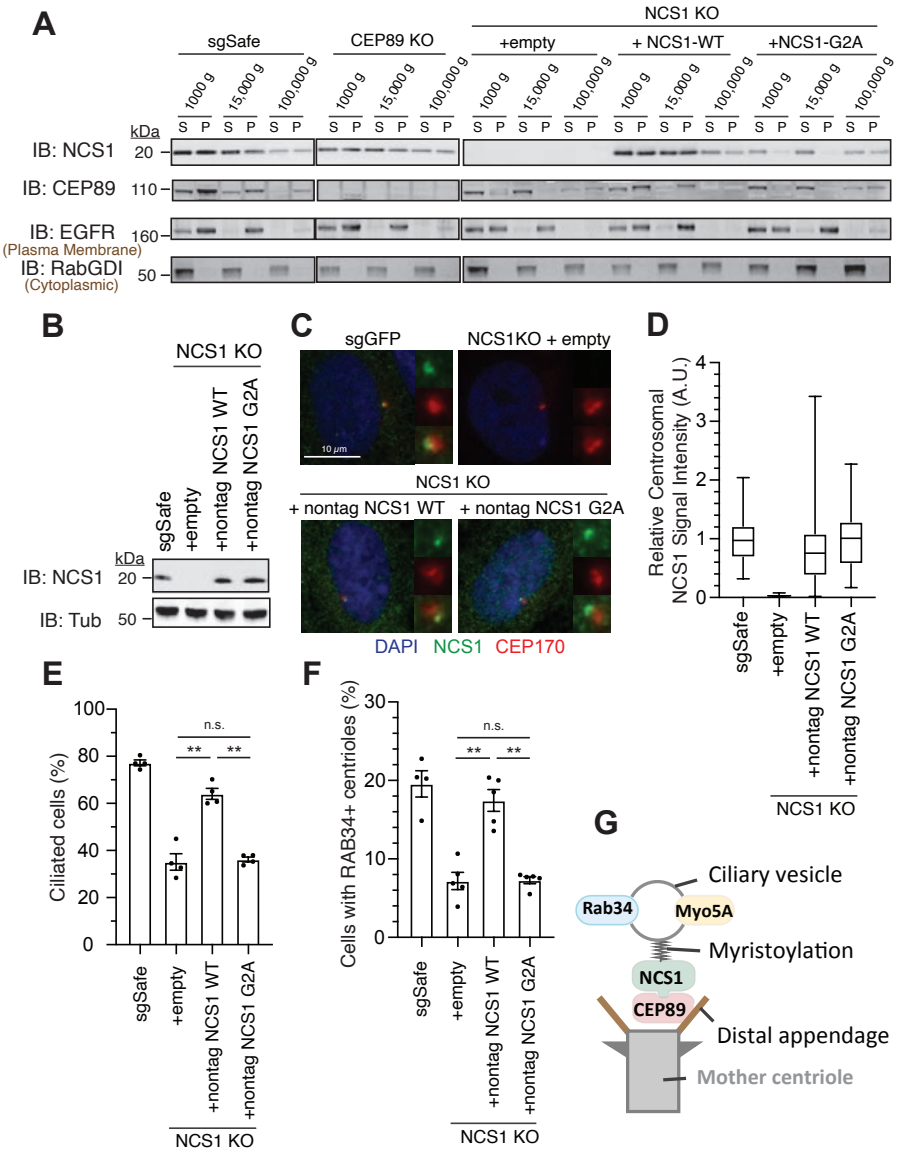

Kanie et al., Figure 5

Figure 5 ***NCS1 captures the ciliary vesicle via its myristoylation motif.***

A. Immunoblot (IB) analysis of expression of NCS1, CEP89, EGFR, and RabGDI. The control (sgSafe) and indicated knockout cells were grown to confluence, lysed by nitrogen cavitation, and fractionated by differential centrifugation at 1,000, 15,000, and 100,000 x g. S: supernatant; P: pellet. Molecular weights (kDa) estimated from a protein marker are indicated. EGFR and RabGDI serves as representative markers for plasma membrane or cytoplasmic proteins, respectively.

B. Immunoblot (IB) analysis of expression of NCS1 and α-tubulin in control (sgSafe) or or indicated RPE cells. Molecular weights (kDa) estimated from a protein marker are indicated.

C. Immunofluorescence images taken via wide-filed microscopy in the cells described in (B) serum starved for 24 hours. Insets at the right panels are the enlarged images of the mother centriole. Scale bar: 10 μm.

D. Box plots showing centrosomal signal intensity of NCS1 in cells described in (B) that were serum starved for 24 hours. A.U., arbitrary units. The data from a representative experiment are shown. The raw data and experimental conditions are available in Figure 5D-Source data.

E. Cilium formation assay in the cells described in (B) serum starved for 24 hours. Data averaged from four independent experiments, and each black dot indicates the value from the individual experiment. Error bars represent ± SEM. Statistics obtained by Welch's t-test. The raw data, experimental conditions, and detailed statistics are available in Figure 5E-Source data.

F. Ciliary vesicle recruitment assay in the cells described in (B) grown to confluence (without serum starvation). Data averaged from 5 independent experiments. Error bars represent ± SEM. Statistics obtained through comparing between each knockout and control by Welch's t-test. The raw data, experimental conditions, and detailed statistics are available in Figure 5F-Source data.

G. A cartoon depicting the model generated by our results. NCS1 is recruited to the distal appendage by CEP89 and captures ciliary vesicle via its myristoylation motif. n.s., not significant; *p < 0.05, **p < 0.01, ***p < 0.001

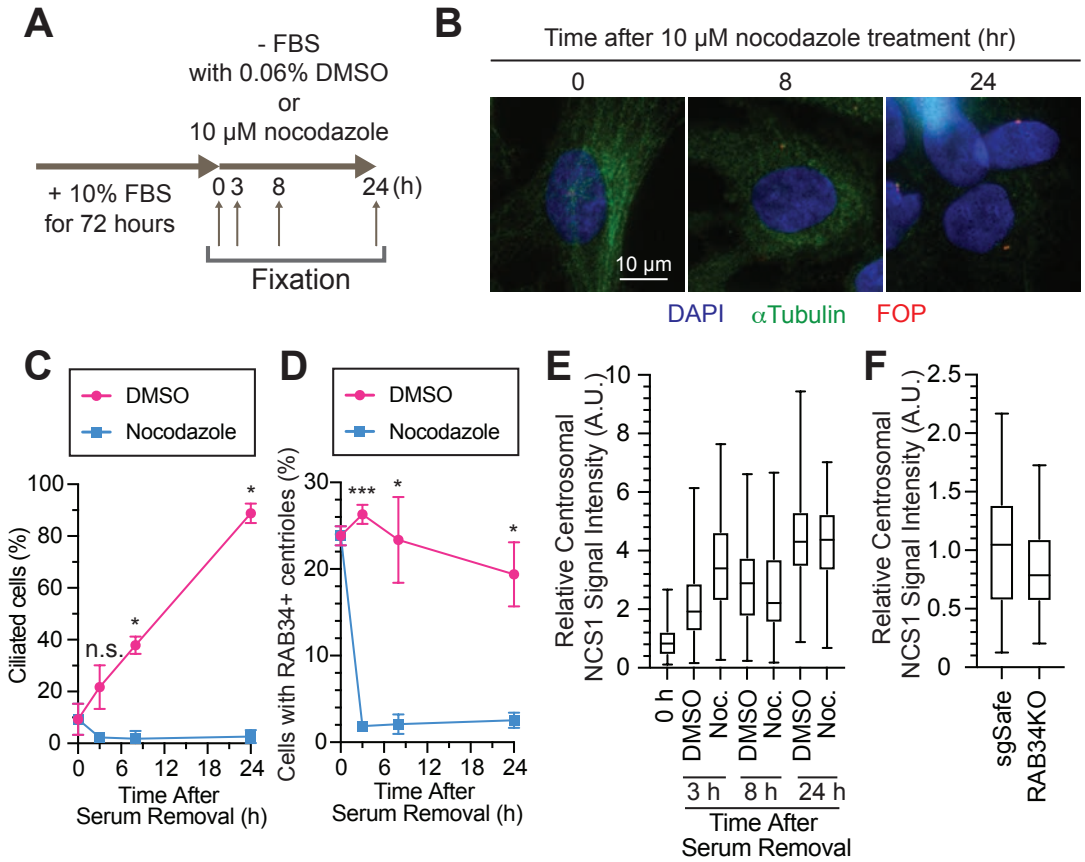

Kanie et al., Figure 6

Figure 6 ***Ciliary vesicle, but not NCS1 and CEP89, is recruited to the centriole via microtubule.***

A. A cartoon showing the method used to test the requirement of microtubules in ciliary vesicle recruitment and NCS1 localization. RPE cells were cultured in media containing 10% FBS for 72 hours, then serum starved (-FBS) for indicated times in the presence of nocodazole or dimethyl sulfoxide (DMSO).

B. Immunofluorescence images taken via wide-filed microscopy. RPE cells were cultured as shown in (A), fixed, and stained with antibodies against α-Tubulin and FGFR1OP (FOP). Scale bar: 10 μm.

C. The time course of cilium formation in cells treated with either DMSO (magenta) or nocodazole (blue). The cells were fixed at indicated time points, stained with α-ARL13B (to mark cilium) and α-CEP170 (to mark centriole), and imaged via wide-field microscopy. Data averaged from three independent experiments. Error bars represent ± SEM. Statistics obtained through comparing between DMSO and nocodazole treated cells at each time point by Welch's t-test. The raw data, experimental conditions, and detailed statistics are available in Figure 6C-Source data.

D. The time course of ciliary vesicle recruitment in cells treated with either DMSO (magenta) or nocodazole (blue). The cells were fixed at indicated time points, stained with α-RAB34 (to mark ciliary vesicle) and α-CEP170 (to mark centriole), and imaged via wide-field microscopy. Data are averaged from three independent experiments. Error bars represent ± SEM. Statistics obtained through comparing between DMSO and nocodazole treated cells at each time point by Welch's t-test. The raw data, experimental conditions, and detailed statistics are available in Figure 6D-Source data.

E. Box plots showing centrosomal signal intensity of NCS1 in RPE cells prepared using the method described in (A). The data from the representative experiment are shown. The raw data and experimental conditions are available in Figure 6E-Source data.

F. Quantification of the centrosomal signal intensity of NCS1 in control or RAB34 knockout RPE cells serum starved for 24 hours. The data from the representative experiment are shown. The raw data and experimental conditions are available in Figure 6F-Source data.

A.U., arbitrary units; n.s., not significant; *$p < 0.05$, **$p < 0.01$, ***$p < 0.001$

1590

1591

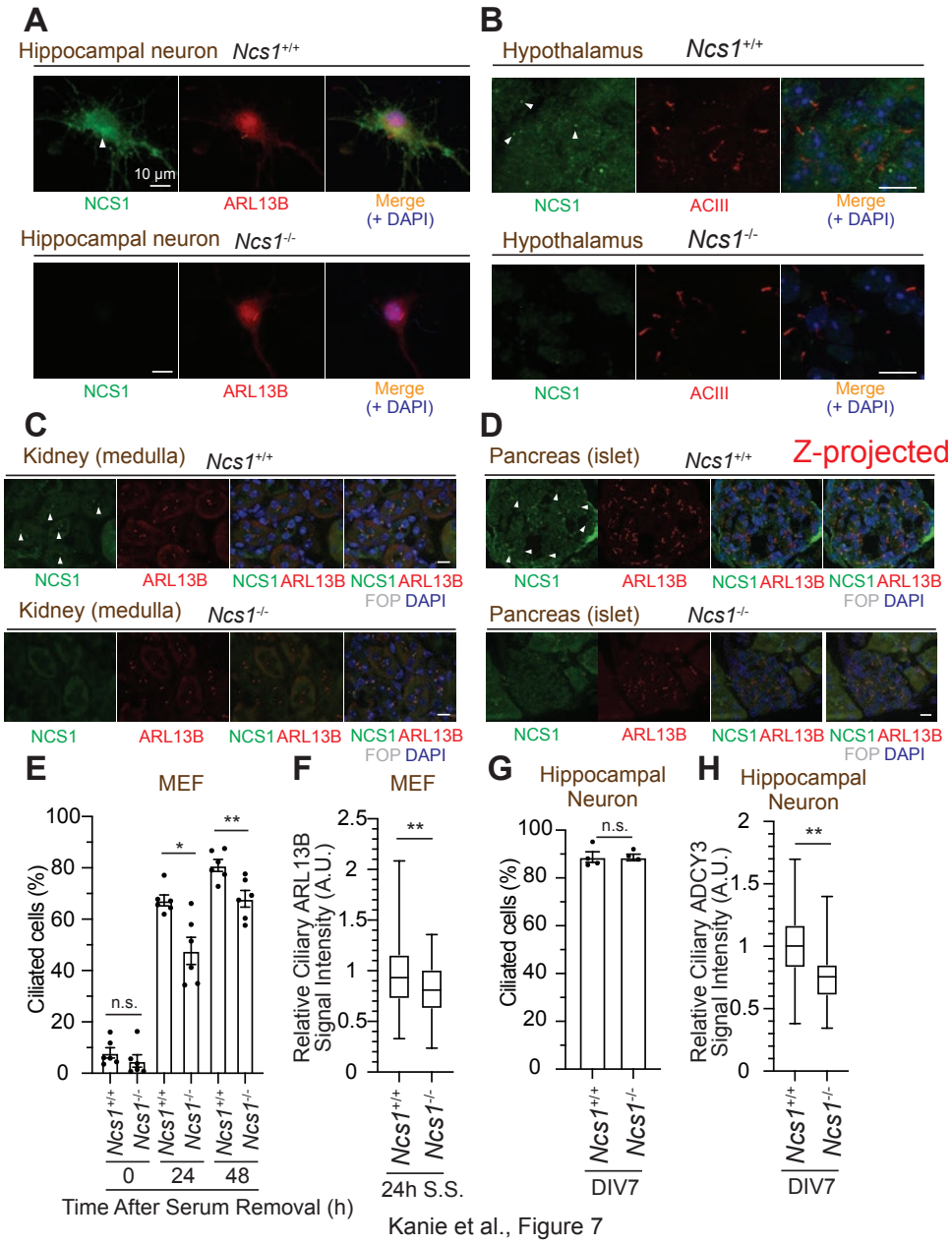

Figure 7 ***NCS1 localizes to the ciliary base in ciliated tissues and gets involved in cilium formation and ciliary membrane protein trafficking.***

A. Immunofluorescence images of cultured hippocampal neurons taken by wide-field microscopy. The isolated hippocampal neurons from E18.5 mice were fixed and stained for the indicated markers. Arrow indicates Ncs1 localization at the ciliary base. The individual image is from a representative z-slice. Scale bar: 10 μm.

B-D. Immunofluorescence images of indicated mouse tissues taken via spinning disk confocal microscopy. Tissue sections prepared from 8 week old *Ncs1*$^{+/+}$ or *Ncs1*$^{-/-}$ mice with the method described in Materials and Methods were stained for indicated markers. The images shown in (D) were created by maximum intensity z-projection. The other images were from representative z-slices. Arrowheads indicate NCS1 localization. Scale bar: 10 μm.

E. Cilium formation assay in *Ncs1*$^{+/+}$ or *Ncs1*$^{-/-}$ mouse embryonic fibroblasts (MEFs) serum starved for indicated time. Data averaged from six different MEFs per genotype. Each black dot indicates the value from the individual experiment. Error bars represent ± SEM. Statistics obtained through comparing between the two genotypes at each time point by Welch's t-test. The raw data, experimental conditions, and detailed statistics are available in Figure 7E-Source data.

F. Box plots showing ciliary signal intensity of ARL13B in *Ncs1*$^{+/+}$ or *Ncs1*$^{-/-}$ MEFs. The cells were serum starved for 24 hours, fixed, stained with α-ARL13B (to mark cilium) and α-CEP170 (to mark centriole), and imaged via wide-field microscopy. Data averaged from six different MEFs per genotype. Statistical significance was calculated from nested T test. The raw data, experimental conditions, and detailed statistics are available in Figure 7F-Source data.

G. Cilium formation assay in isolated hippocampal neurons prepared from *Ncs1*$^{+/+}$ or *Ncs1*$^{-/-}$ E18.5 mouse embryos at 7 days in vitro (DIV). Data are averaged from four different hippocampal neurons per genotype. Each black dot indicates the value from the individual experiment. Error bars represent ± SEM. Statistics obtained through comparing between the two genotypes at each time point by Welch's t-test. The raw data, experimental conditions, detailed statistics are available in Figure 7G-Source data.

H. Box plots showing ciliary signal intensity of ADCY3 in isolated hippocampal neurons prepared from *Ncs1*$^{+/+}$ or *Ncs1*$^{-/-}$ E18.5 mouse embryos at DIV7. The cells were fixed and stained with α-ADCY3 antibody, and imaged via wide-field microscopy. Data are averaged from five different neurons per genotype. Statistical significance was calculated from nested T test. The raw data, experimental conditions, and detailed statistics are available in Figure 7H-Source data.

A.U., arbitrary units; n.s., not significant; *p < 0.05, **p < 0.01, ***p < 0.001

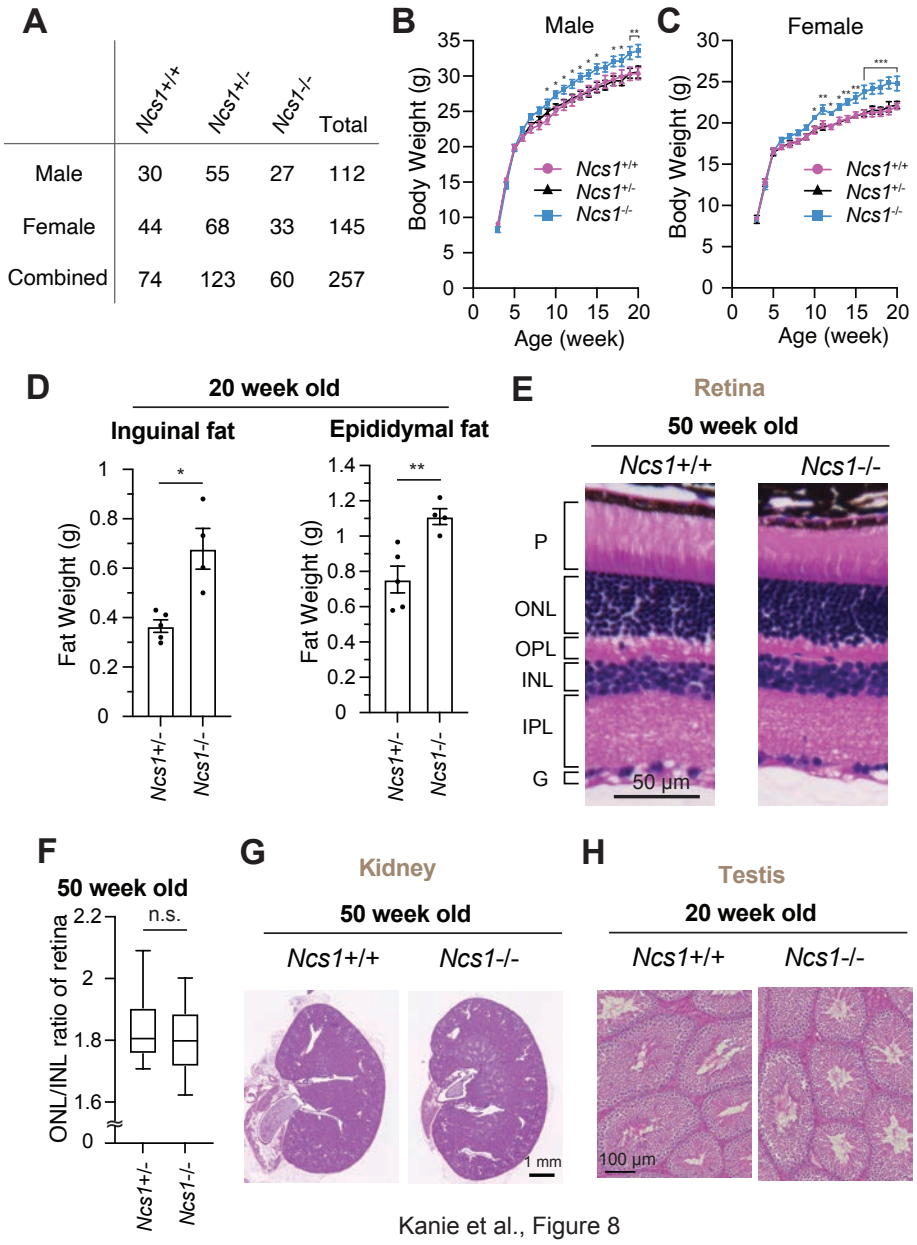

Figure 8 *Ncs1* knockout mice display obesity but no other ciliopathy-related phenotypes.

A. A table showing viability of *Ncs1*$^{+/+}$, *Ncs1*$^{+/-}$, or *Ncs1*$^{-/-}$ mice, generated by crossing *Ncs1*$^{+/-}$ male and female, at P21. Detailed information of the mice and statistics are available in Figure 8A-Source Data.

B-C. Body weight analysis of *Ncs1*$^{+/+}$, *Ncs1*$^{+/-}$, or *Ncs1*$^{-/-}$ male (B) and female (C) mice. Raw data and detailed statistics are available from Figure 8B-C-Source Data.

D. Measurements of the weights of inguinal fat (left) or epididymal fat (right) from 20-week-old *Ncs1*$^{+/+}$ or *Ncs1*$^{-/-}$ male mice. Raw data and detailed statistics are available in Figure D-Source Data.

E. Hematoxylin and Eosin (H&E) staining of the retina prepared from 50-week-old *Ncs1*$^{+/+}$ or *Ncs1*$^{-/-}$ female mice. Scale bar: 50 μm. G, ganglion cell layer; IPL, inner plexiform layer; INL, inner nuclear layer; OPL, outer plexiform layer; ONL, outer nuclear layer; P, photoreceptor cell layer. Representative images from five *Ncs1*$^{+/+}$ or *Ncs1*$^{-/-}$ mice are shown. Detailed information of the mice is available in Figure 8E-G-H-Source Data.

F. Quantification of ONL/INL ration of the retina prepared from 50-week-old *Ncs1*$^{+/+}$ or *Ncs1*$^{-/-}$ mice. 8 areas per mouse and 5 mice from each genotype were analyzed. Statistical significance was calculated from nested T test. The raw data, detailed information of the mice, and detailed statistics are available in Figure 8F-Source Data.

G-H. H&E staining of the kidney (G) or Testis (H) prepared from 50-week-old *Ncs1*$^{+/+}$ or *Ncs1*$^{-/-}$ female mice (G) or 20-week-old *Ncs1*$^{+/+}$ or *Ncs1*$^{-/-}$ male mice. Scale bar: 1mm (G) and 100 μm (H). Representative images from five (G) or three (H) *Ncs1*$^{+/+}$ or *Ncs1*$^{-/-}$ mice are shown. Detailed information of the mice is available in Figure 8E-G-H-Source Data.

n.s., not significant; *$p < 0.05$, **$p < 0.01$, ***$p < 0.001$

Figure supplements

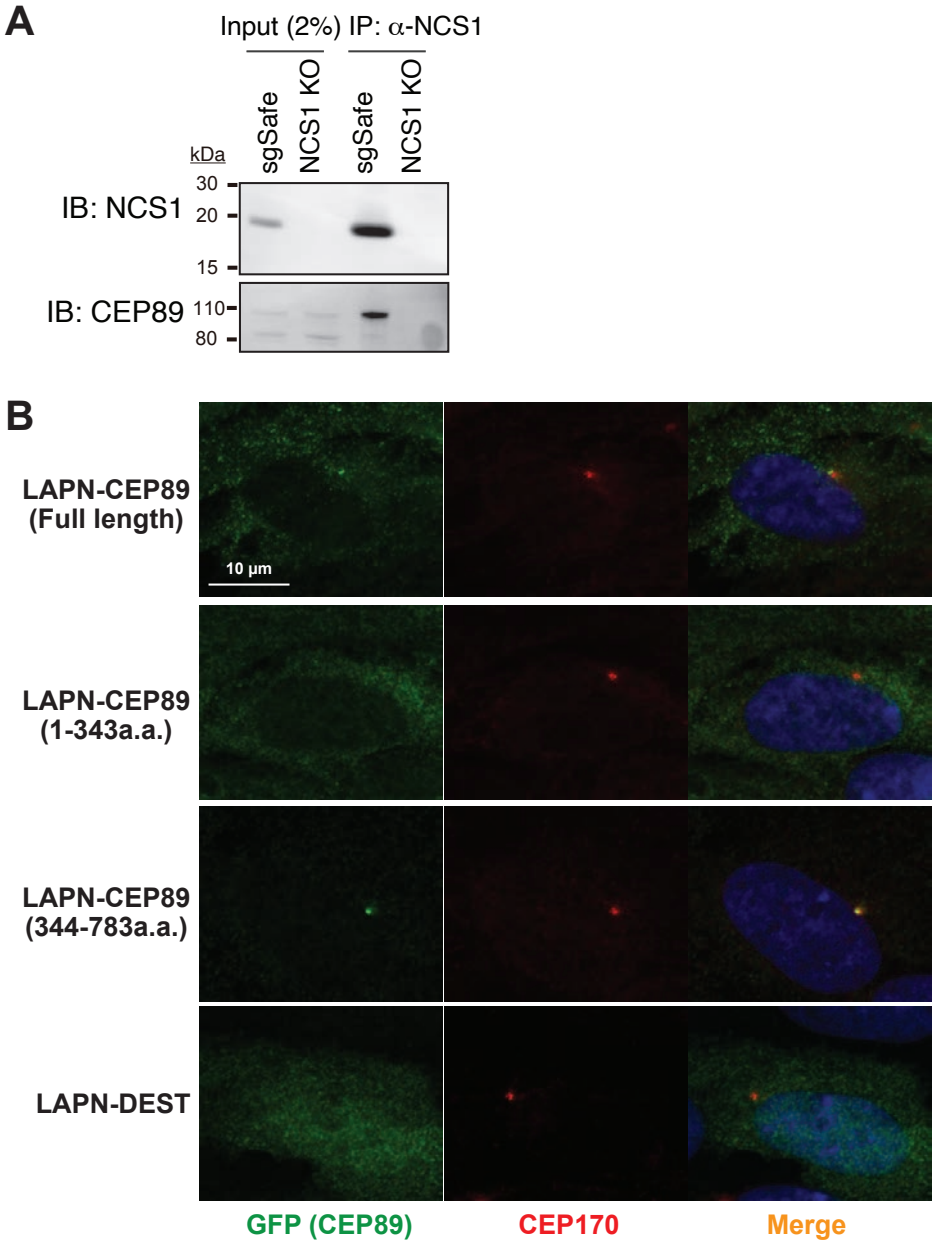

Kanie et al., Figure 1-figure supplement 1

Figure 1-figure supplement 1 ***Individual channels of the images shown in Figure 1A.***

A. Immunoblot (IB) analysis of the eluates from co-immunoprecipitation assay of endogenous NCS1 in the control (sgSafe) or NCS1 knockout cells. The eluates were immunoblotted with antibodies against NCS1 or CEP89. Molecular weights (kDa) estimated from a protein marker are indicated.
B. Immunofluorescence images taken via wide-field microscopy. RPE cells expressing the indicated N-terminally LAP (EGFP and S) tagged fragments of CEP89 or LAPN (control) were serum starved for 24 hours, fixed, and stained with antibodies against GFP and CEP170. Scale bar: 10 μm.

1593

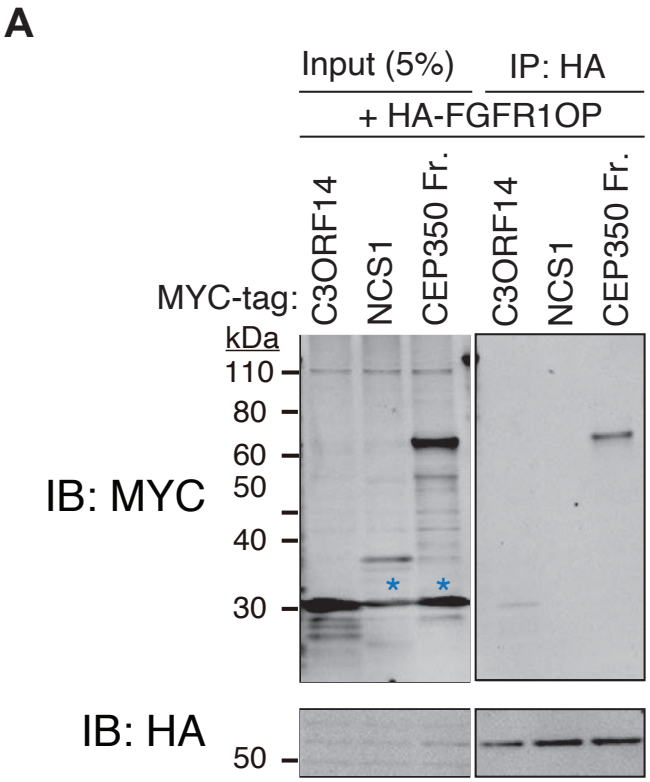

Kanie et al., Figure 1-figure supplement 2

Figure 1-figure supplement 2 ***A negative control for the experiment shown in Figure 1E and F.***

A. Immunoblot (IB) analysis of the eluates from *in vitro* binding assay of the *in vitro* translated N-terminally HA-tagged FGFR1OP and the indicated N-terminally MYC tagged proteins. The *in vitro* translated proteins were mixed and captured by HA-agarose beads, resolved by SDS-PAGE and immunoblotted with the indicated antibodies. The CEP350 fragment (2470-2836 a.a.), which binds to FGFR1OP efficiently (Kanie et al. 2017) serves as a positive control. Blue asterisks indicate non-specific bands, which overlap with the MYC-tagged C3ORF14. Molecular weights (kDa) estimated from a protein marker are indicated.

1594

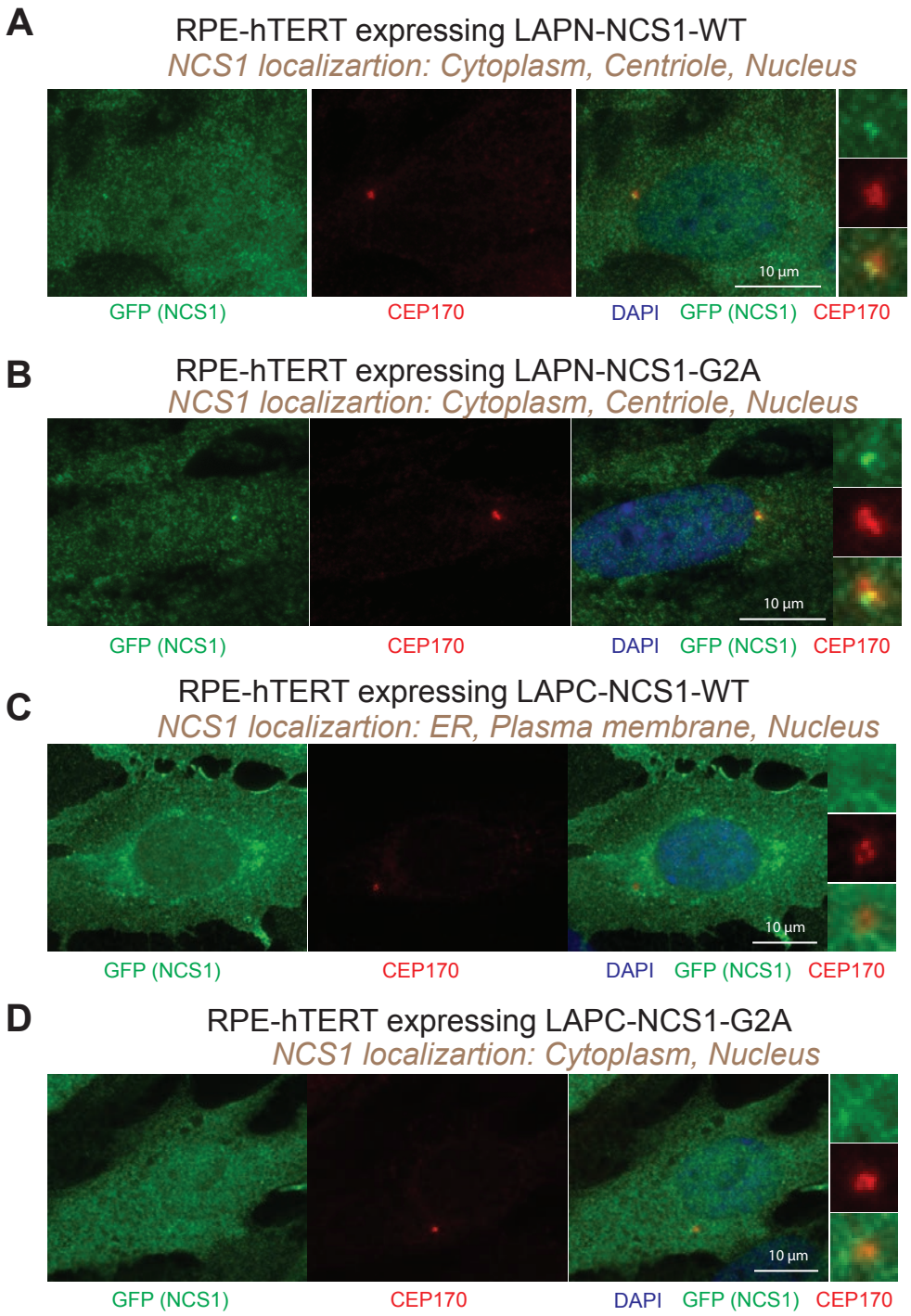

Kanie et al., Figure 2-figure supplement 1

Figure 2-figure supplement 1 ***Localization of GFP tagged NCS1.***

A-D. Immunofluorescence images taken via wide-field microscopy. RPE cells expressing N-terminally LAP tagged wilde-type NCS1 (A), N-terminally LAP tagged myristoylation defective mutant (G2A) of NCS1 (B), C-terminally LAP tagged wild-type NCS1 (C), or C-terminally LAP tagged myristoylation defective mutant (G2A) of NCS1 (D) were serum starved for 24 hours, fixed, and stained with indicated antibodies. Scale bar: 10 μm. Insets at the right panels are the enlarged images of the mother centriole. The experimental conditions are available in Figure 2-Figure Supplement 1-Source Data.

1595

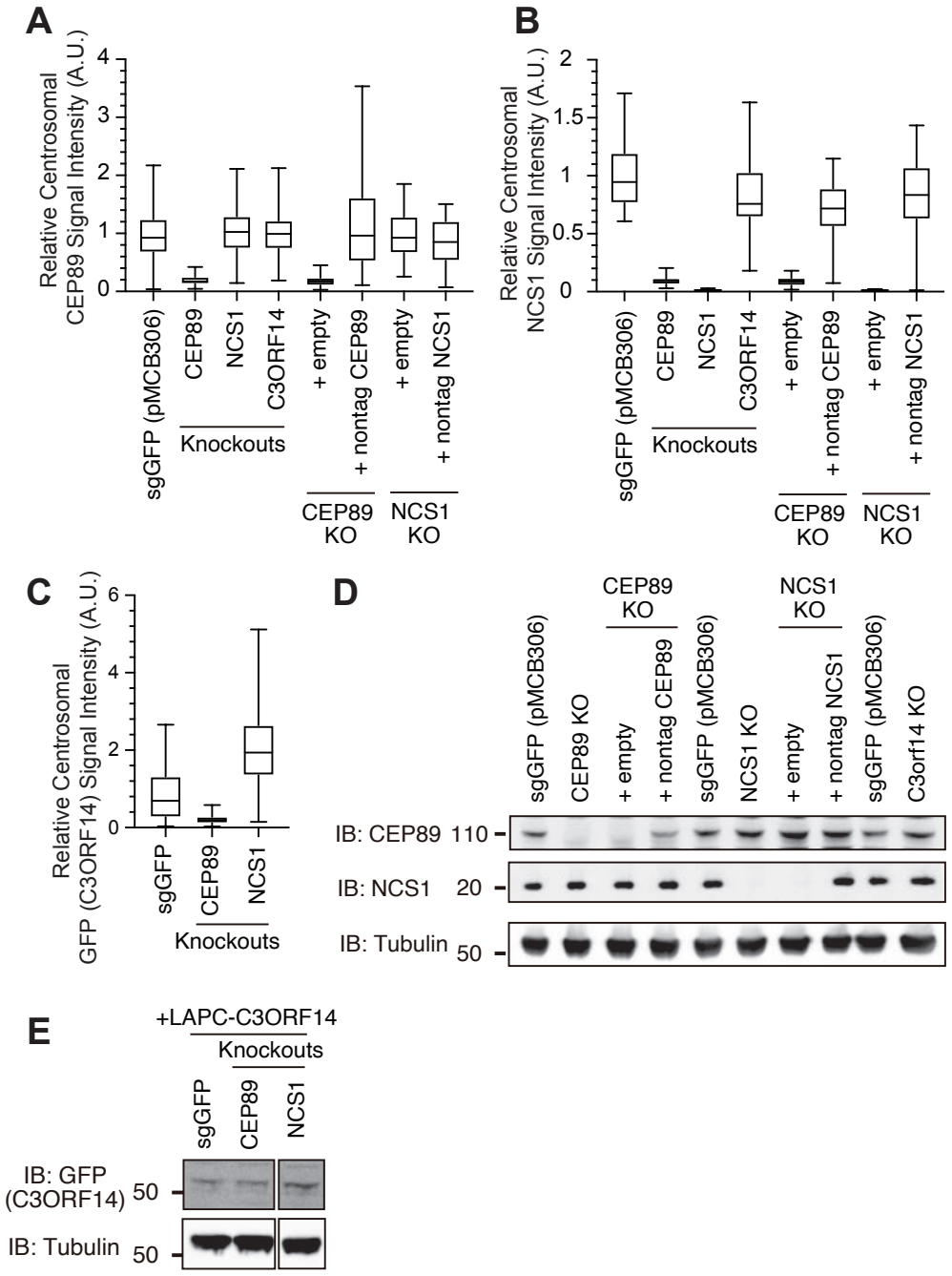

Kanie et al., Figure 2-figure supplement 2

Figure 2-figure supplement 2 ***Quantification data and Westen blot related to Figure 2.***

A-C. Box plots showing centrosomal signal intensity of CEP89 (A), NCS1 (B), or GFP-C3ORF14 (C) from the immunofluorescence experiments shown in Fig.2K-M. Data from a representative experiment are shown. A.U., arbitrary units. The raw data and experimental conditions are available in Figure 2-Figure Supplement 2A-C-Source Data.

D-E. Immunoblot (IB) analysis of expression of CEP89, NCS1, and LAPC-C3ORF14 in indicated RPE cells. The cells were serum starved for 24 hours, lysed and analyzed by immunoblot. Molecular weights (kDa) estimated from a protein marker are indicated.

A.U., arbitrary units; n.s., not significant

1596

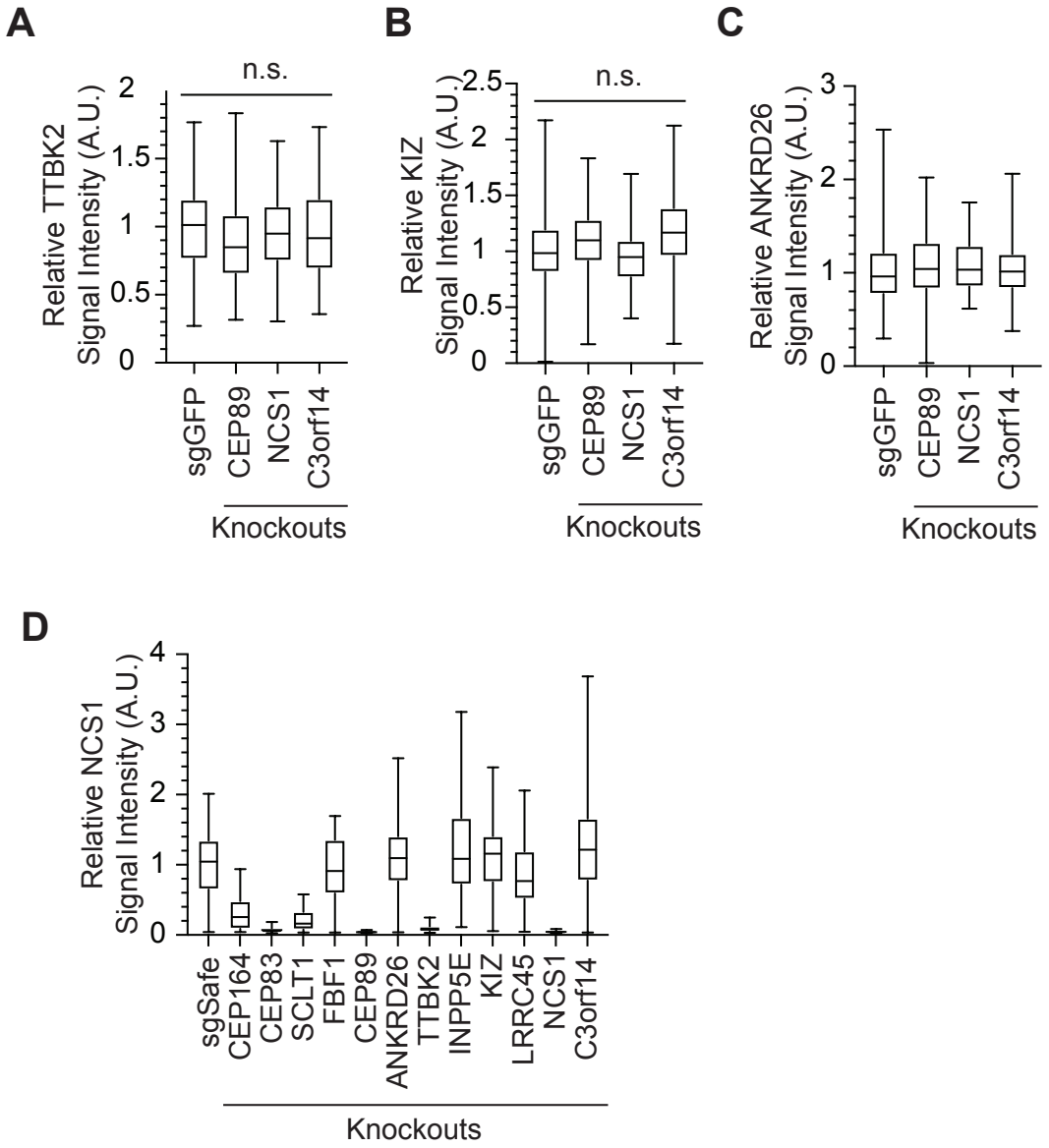

Kanie et al., Figure 2-figure supplement 3

Figure 2-figure supplement 3 ***Localization of distal appendage protein in NCS1 knockouts.***

A-B. Box plots showing centrosomal signal intensity of TTBK2 (A) and KIZ (B) in control (sgGFP), CEP89, NCS1, or C3ORF14 knockout RPE cells. The data combined from three independent experiments. Statistical significance was calculated from nested T test. The raw data, experimental conditions, detailed statistics are available in Figure 2-figure supplement 3A-B-Source data.

C-D. Quantification of centrosomal signal intensity of ANKRD26 (C) and NCS1 (D) in indicated RPE cells. The data from the representative experiment are shown. The raw data and experimental condition are available in the source data of Figure 2-figure supplement 3C-D-Source data.

1597

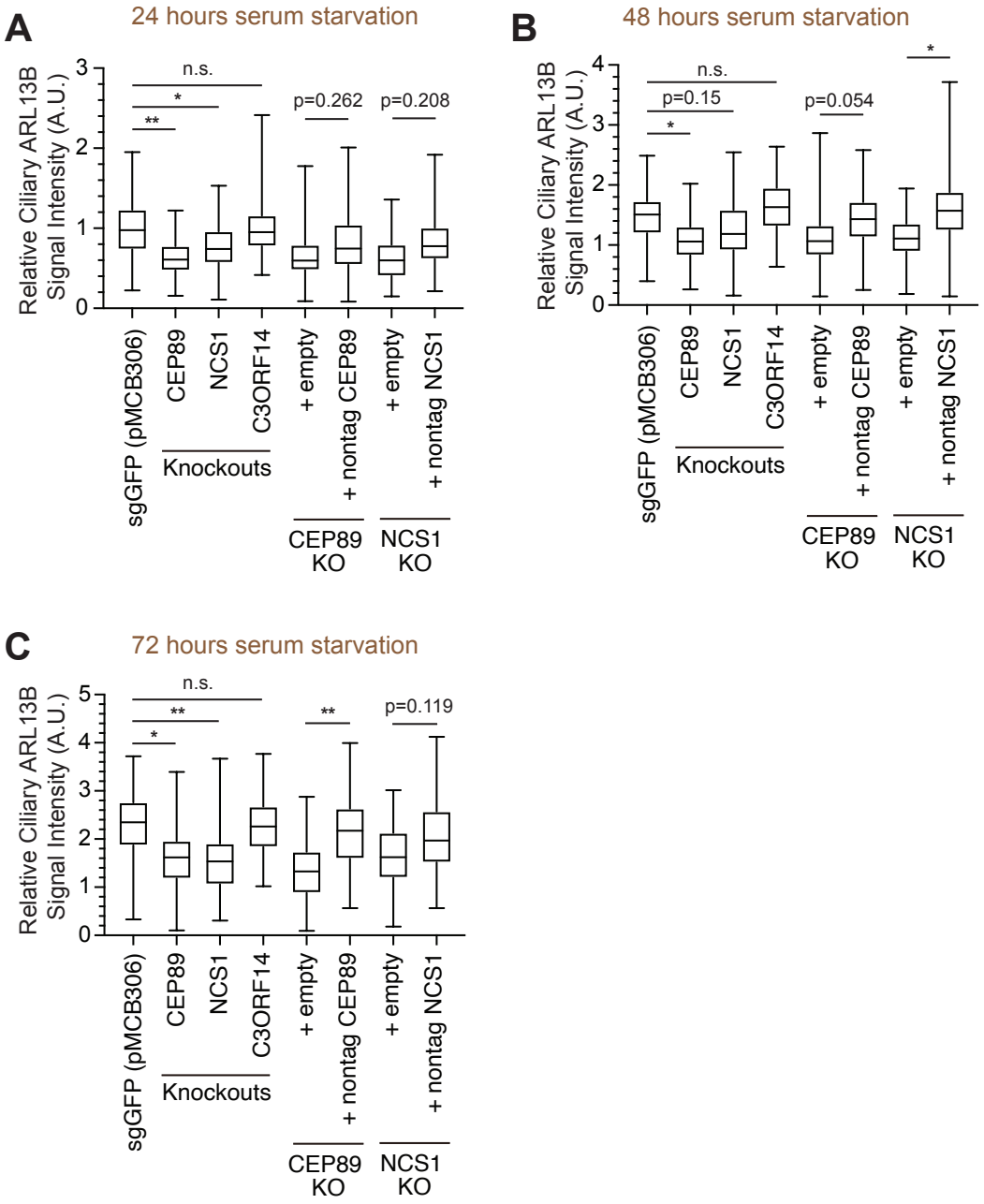

Kanie et al., Figure 3-figure supplement 1

Figure 3-figure supplement 1 ***Quantification of ciliary signal intensity of ARL13B in CEP89 and NCS1 knockouts.***

A-C. Quantification of ciliary signal intensity of ARL13B in indicated cells. The cells were serum starved for 24 (A), 48 (B), and 72 (C) hours, fixed, stained with α-ARL13B (cilium marker) and α-CEP170 (centriole marker), and imaged via wide-field microscopy. Data are averaged from three independent experiments. Error bars represent ± SEM. Statistics obtained by One-way ANOVA with Šídák's multiple comparison test. The raw data, experimental conditions, detailed statistics are available in Figure3-figure supplement 1-Source data.
A.U., arbitrary units.

1598

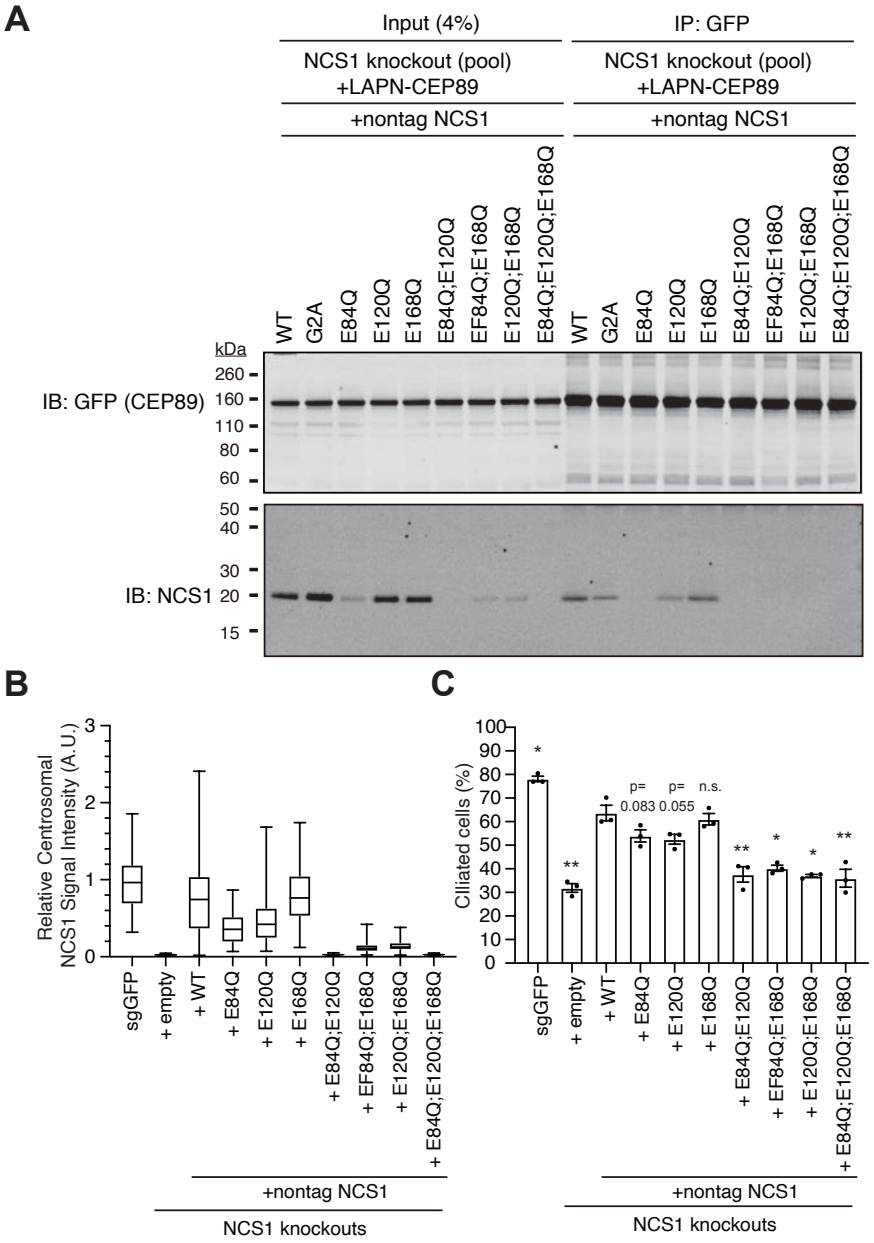

Kanie et al., Figure 5-figure supplement 1

Figure 5-figure supplement 1 ***Calcium is required mainly for the stability of NCS1.***

A. Immunoblot (IB) analysis of the eluates from co-immunoprecipitation assay of NCS1 knockout RPE cells stably expressing wild-type or indicated point mutants of untagged NCS1 and N-terminally LAP (EGFP and S) tagged CEP89. The cell lysates were co-immunoprecipitated with GFP antibodies, resolved by SDS-PAGE and immunoblotted with indicated antibodies. Molecular weights (kDa) estimated from a protein marker are indicated.

B. Box plots showing centrosomal signal intensity of NCS1. Control (sgGFP) or NCS1 knockout RPE cells stably expressing wild-type or indicated point mutants of NCS1were serum starved for 24 hours. Cells were fixed and stained with NCS1 antibody. Centrosomal signal intensity of NCS1 was measured from fluorescent images with the method described in Materials and Methods. A.U., arbitrary units. Data from a representative experiment are shown. The raw data and experimental conditions are available in Figure 5-figure supplement 1B-Source data.

C. Cilium formation assay in cells described in (B) serum starved for 24 hours. Data are averaged from three independent experiments, and each black dot indicates the value from the individual experiment. Error bars represent ± SEM. Statistics obtained through comparing between each mutant and wild-type NCS1 by Welch's t-test. The raw data, experimental conditions, and detailed statistics are available in Figure 5-figure supplement 1C-Source data.

n.s., not significant; *p < 0.05, **p < 0.01, ***p < 0.001

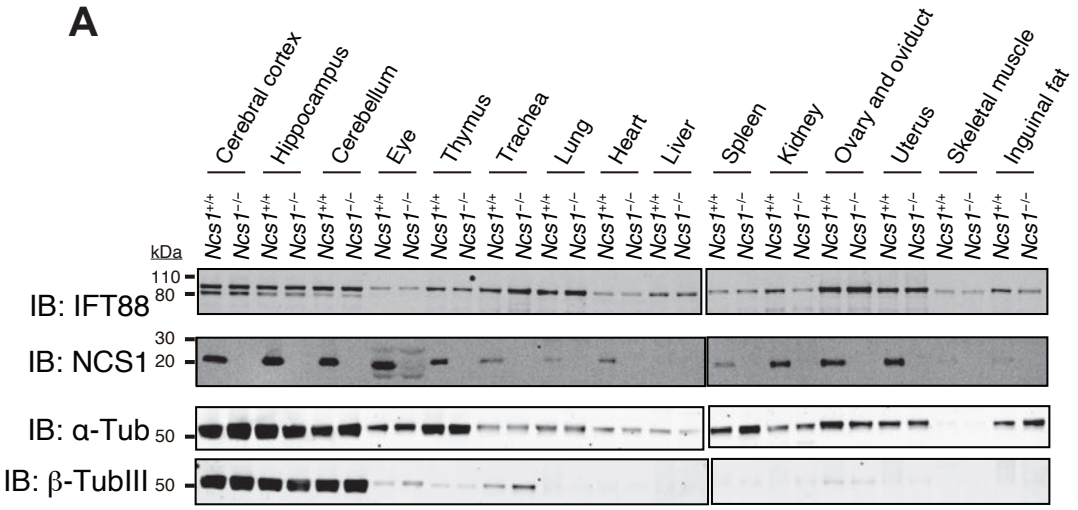

Kanie et al., Figure 7-figure supplement 1

Figure 7-figure supplement 1 ***The expression of NCS1 in various tissues.***

A. Immunoblot (IB) analysis of the indicated tissue lysate from *Ncs1*$^{+/+}$ (7-week-old) or *Ncs1*$^{-/-}$ (6-week-old) mice. 50 μg (for NCS1 detection) or 12 μg (for detection of other proteins) of each tissue lysate was loaded and analyzed by immunoblot with the indicated antibodies. Molecular weights (kDa) estimated from a protein marker are indicated.

1600

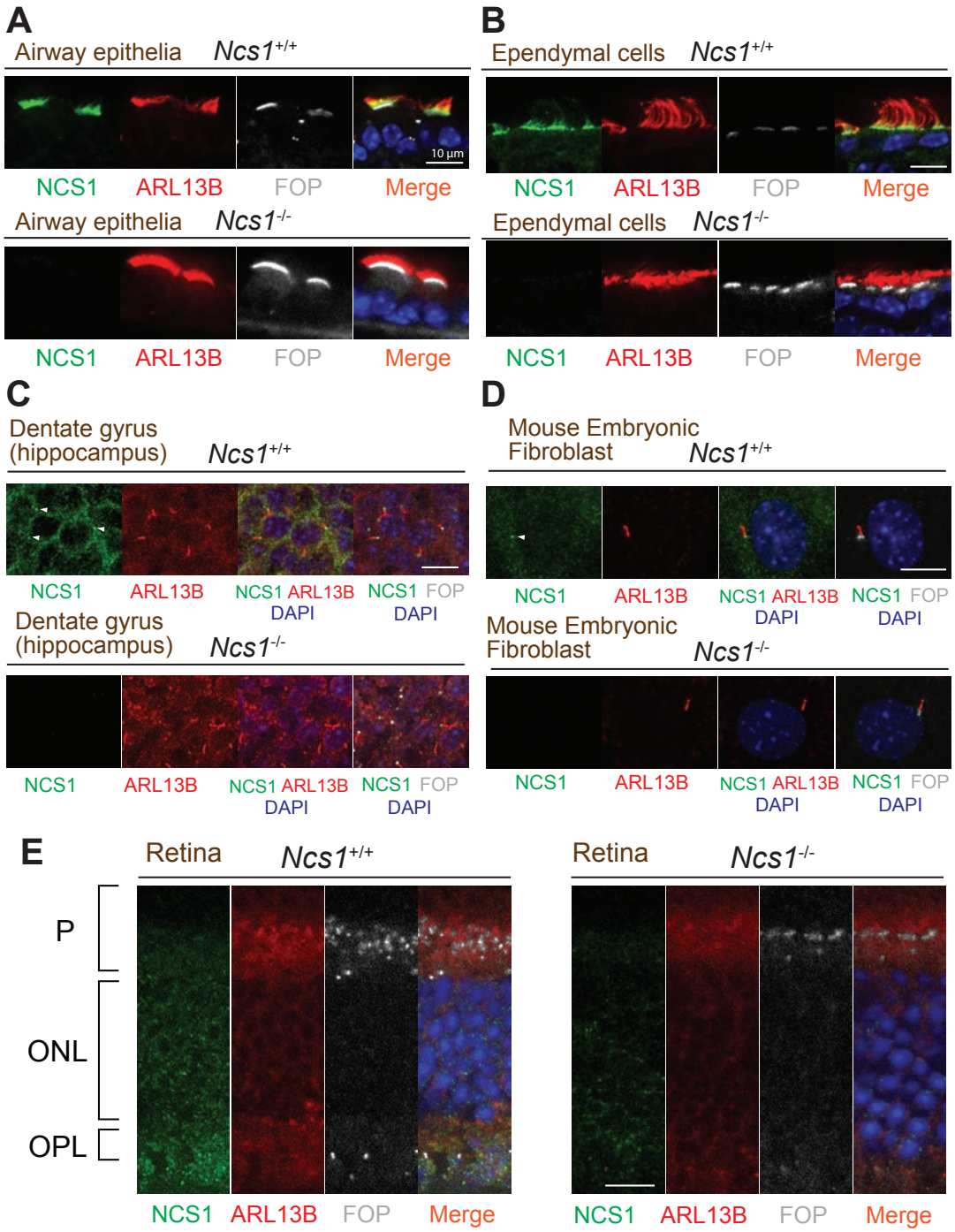

Kanie et al., Figure 7-figure supplement 2

Figure 7-figure supplement 2 ***NCS1 localizes to the ciliary base in most ciliated tissues but not in photoreceptor cells.***

A-E. Immunofluorescence images of indicated mouse tissues taken via spinning disk confocal microscopy. Tissue sections prepared from 8-week-old *Ncs1*$^{+/+}$ or *Ncs1*$^{-/-}$ mice with the method described in materials and methods were stained for indicated markers. Arrowheads indicate NCS1 localization. The individual image is from a representative z-slice. Scale bar: 10 μm. P, photoreceptor cell layer; ONL, outer nuclear layer; OPL, outer plexiform layer.

1601

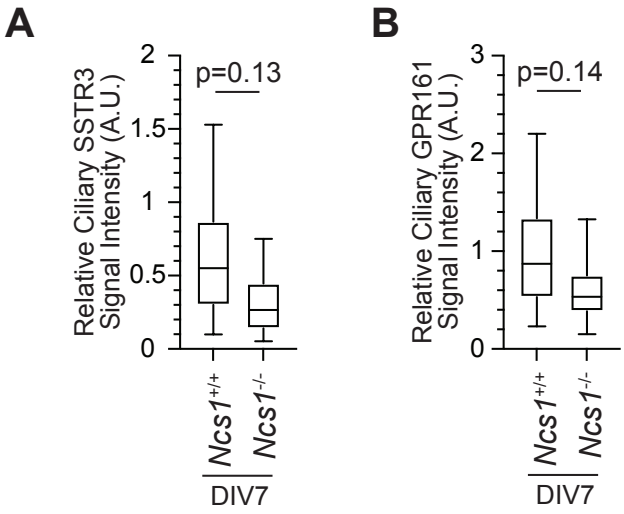

Kanie et al., Fig.7- figure supplement 3

Figure 7-figure supplement 3 ***Localization of ciliary GPCRs is mildly decreased in hippocampal neurons prepared from Ncs1$^{-/-}$ mice.***

A-B. Box plots showing ciliary signal intensity of SSTR3 (A) or GPR161 (B) in isolated hippocampal neurons prepared from E18.5 *Ncs1*$^{+/+}$ or *Ncs1*$^{-/-}$ mouse embryos. The cells were cultured in vitro for 7 days (DIV7), fixed, and stained with either SSTR3 or GPR161 together with α-ARL13B (to mark cilium) and α-FGFR1OP (to mark centriole), and imaged via wide-field microscopy. Data are averaged from five different neurons per genotype for SSTR3 and 3 *Ncs1*$^{+/+}$ and 4 *Ncs1*$^{-/-}$ neurons for GPR161. Statistical significance was calculated from nested T test. The raw data, experimental conditions, detailed statistics are available in Figure 7-figure supplement 3A-B-Source data.

1602